Gravity and Magnetic Investigations of the Greater Magadi Area in Kenya

John Gitonga Githiri

DOCTOR OF PHILOSOPHY

(Physics)

JOMO KENYATTA UNIVERSITY OF AGRICULTURE AND TECHNOLOGY

2009

Gravity and Magnetic Investigations of the Greater Magadi Area in Kenya

John Gitonga Githiri

A Thesis Submitted In Partial Fulfillment for the Degree of Doctor of Philosophy in Physics in the Jomo Kenyatta University of Agriculture and Technology

2009

DECLARATION

This thesis is my original work and has not been presented for a degree in any other university.

Signature: ---------- Date: ----------

John Gitonga Githiri

This thesis has been submitted for examination with our approval as university supervisors.

1. Signature: ---------- Date: ----------

Prof. J.P Patel

UON, Kenya.

2. Signature: ---------- Date: ----------

Prof. J.O. Barongo

UON, Kenya.

3. Signature: ---------- Date: ----------

Prof. P.K Karanja

JKUAT, Kenya.

DEDICATION:

This work is dedicated to my dear wife and children, dear parents, brothers and sisters. They were a source of encouragement and inspiration to me. All the glory is to almighty God.

ACKNOWLEDGEMENTS

I would wish to extend my sincere thanks to my academic supervisors: **Professor J.P Patel** first for encouraging me to develop a proposal and continue my previous research at Magadi , secondly for his continuous guidance throughout my research and always having been available when I needed to consult, **Professor Justus Barongo** through whose vast experience in magnetics I greatly benefited during our many discussions also a source of encouragement and very supportive at all times I consulted him, **Professor P.K Karanja** for his keen interest in my work. He has been quite understanding and encouraged me throughout my work.

I would also appreciate Geomatics Department of JKUAT for allowing me to use their GPS system and topographic maps. Special gratitude to Mr Muriuki for having spent time assisting in digitization of the maps. I also wish to thank other institutions as National Oil corporation of Kenya for provision of software and Kenyatta University for lending me their Proton Precession and Flux gate magnetometers. I am also grateful to the administration of Magadi Soda Company for their hospitality in accommodating my research team at their premises. I am also much indebted to Dr Kinyua (chairman, Physics JKUAT) and all members of Physics Department JKUAT for the moral support and encouragement. I especially appreciate Mr Munyithya for the company during my field work and useful discussions we have had together.

My entire PhD study was funded by JKUAT through the RPE Department. I gratefully acknowledge their generosity in being a beneficiary of their research funding scheme.

TABLE OF CONTENTS

LIST OF TABLES

LIST OF FIGURES

LIST OF APPENDICES

ABBREVIATIONS

Ma	Million years
2-D	Two dimensional
3-D	Three dimensional
KRISP	Kenya Rift International Seismic Project
LMT	Long period Magneto-telluric
g.u	gravity units (1 g.u = 10^{-6} ms^{-2})
mg	milli-grams
ms	milli-second
nT	nano Teslas
mgals	milli-gals
B_Z	Vertical magnetic field component
B_H	Horizontal magnetic field component
B_T	Total magnetic field vector
B_Z	Vertical magnetic field component
B_e	Ambient geomagnetic field
D	Magnetic declination
I	Magnetic inclination
I’	Reduced magnetic inclination
χ	Magnetic susceptibility
M_i	Induced magnetization
M_r	Remanent magnetization
H	Magnetizing force
G	Universal gravitational constant, 6.67 x 10^{-11} NM^2Kg^{-2}

ρ	Crustal density
σ	Bouguer slab density
f	Frequency
γ_p	Gyromagnetic ratio
π	Constant, 3.14
GPS	Global Positioning System
IGSN	International Gravity Standardization Network
NOCK	National Oil Corporation of Kenya
GRS	Geodetic Reference System
φ	Geographic latitude
β	Dip of dike
f	Flattening
ω	Angular frequency
h	Height (altitude)
α	Azimuth of profile relative to magnetic north
e	First numerical eccentricity = 0.081819191
Δg_h	Free-air anomaly
Δg_{bc}	Bouguer correction
g_{sb}	Bouguer slab correction
g_{fa}	Free air correction
g_{ter}	Terrain correction
g_e	Normal gravity at equator, = 978032.67715 mgal
RTP	Reduction to the pole
N	Structural index

B	Regional field value
T	Potential field

ABSTRACT

Magadi area is located in the southern part of the Kenyan rift, an active continental rift that is part of the East African Rift system. Thermal manifestations in the form of hot springs in the northern and southern shores of Lake Magadi and high heat flows suggest geothermal potential in the area. Local seismic activity monitored previously around Lake Magadi revealed an earthquake cluster caused by swarm activity in the rift centre at shallow depths, which was probably triggered by magma movements. Magma detected at shallow depths may be used as a heat source for a geothermal resource while seismic activity due to its presence may be considered a geo-hazard to nearby cities.

Ground magnetic and gravity investigations were carried out as a follow-up to locate any body at depth with sufficient magnetic susceptibility and density contrast respectively that may represent magmatic intrusions. The necessary corrections were applied to both raw gravity and magnetic data and Bouguer and magnetic contour maps prepared respectively. Euler deconvolution technique was used to image depth to the causative bodies. From the magnetic field data, an attempt was made to estimate depth to the curie isotherm using spectral analysis. The isotherm is a marker to the depth below which the rocks cease to be magnetic when their temperature exceeds Curie point temperature. The Curie point depths obtained range from 5.2-8.3 km along the selected profiles suggesting a high geothermal gradient. The estimated vertical temperature gradients along the profiles range between 69.92 ˚C/Km and 111.53 ˚C/Km. 2-D gravity and magnetic models of the subsurface structure were also generated by forward modelling. A body of density of 3.20 gcm^{-3} and susceptibility

contrasts 0.0428 SI was modelled on the northern region near little Magadi at a depth of approximately 0.4 km. The location of the body coincides with the area where earthquake swarm occurs. Such a body of high density and susceptibility contrasts may consist of hot mantle derived material that may have intruded the crust. The slowly cooling magmatic intrusions heats underground water producing hot springs that issue from faults. Earthquakes recorded may be due to stress concentration due to crustal heterogeneity due to magmatic intrusives. The result of this study hence indicates presence of shallow heat sources that could harness geothermal energy exploration. The intrusives detected may be causing stress on the rocks and hence chances of an earthquake are high.

As a measure to avert destruction in event of such earthquakes, earthquake resistant structures are recommended in major towns in the vicinity of Magadi area. A detailed reconnaissance gravity and magnetic survey is recommended in the north eastern and southern area of Lake Magadi to image the bodies at a higher resolution. This could not have been achieved due to large station spacing resulting from large area coverage and inaccessibility of some regions that were security restricted zones. Other studies to determine temperature and other parameters of importance in assessing a geothermal resource are recommended in this area.

CHAPTER ONE

INTRODUCTION

1.0 BACKGROUND OF STUDY AREA.

Magadi area which is the study area is located in Kajiado district, approximately 100 km from Nairobi. The study area is bounded by latitudes 1˚ 40’ S and 2˚ 10’ S, and longitudes 36˚ 00’ E and 36˚ 30’ E as illustrated in Figure 1.1. It is in the southern part of the Gregory Rift, an active continental rift that is part of the East African Rift System. The Gregory Rift is of continental rift type (Gregory, 1921); it extends from the Magadi –Natron basin in the south to Baringo and Suguta grabens in the north and is a complex graben bisecting the Kenya domal uplift.

Lake Magadi is located in a broad flat depression that occurs at the lowest point in the southern Kenya Rift Valley. The Magadi area is largely covered by Quaternary sediments that overlie extensive Pleistocene trachyte lavas. The trachyte lava overlies Pliocene olivine basalts and nephelinites, which, in turn rest on the Archean basement. A dense network of grid faults affects the area. These faults, especially the north-south trending fault scarps, control the occurrence of geothermal manifestations (Riaroh and Okoth, 1994)

Geothermal fields are present in Magadi characterized by fissure eruptions, which are trachytic in composition. Hot springs are distributed along the shores of Lake Magadi issuing from the base of fault scarps.

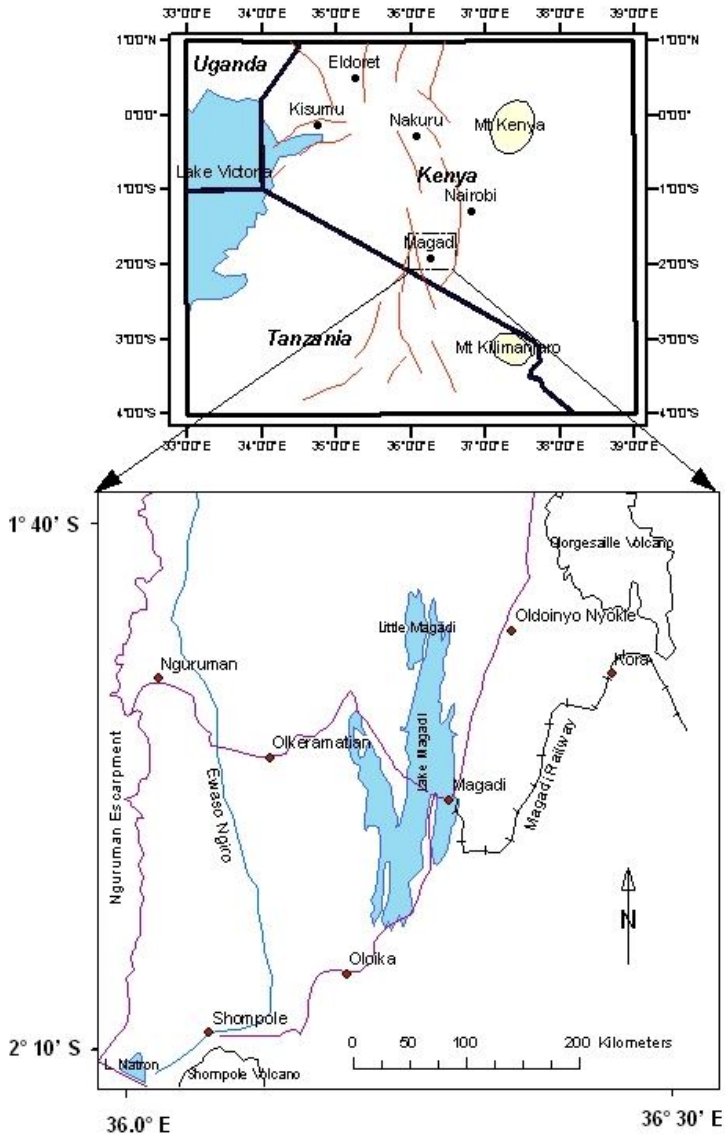

Fig. 1.1 Location map of the study area.

1.1 PROBLEM STATEMENT

This study is to be carried out with a view to understanding the subsurface structure of the greater Magadi area by investigating possibility of presence of bodies responsible for high seismicity that may be possible heat sources. Previous geophysical works done in the area reveal high seismicity implying high activity in the subsurface. During one of the first micro-earthquake surveys in Kenya, Molnar and Aggarwal (1971) found the Magadi Rift to be seismically the most active section of the Kenya Rift. Later, as part of the Kenya Rift International Seismic Project (KRISP 94), a temporary seismic network around Lake Magadi recorded more than 200 events in a period of two weeks. A seismotectonic and crustal structure study by Ibs-Von Seht *et al.* (2001) revealed an earthquake cluster north of Lake Magadi, beside little Magadi as illustrated in figure 1.2. The cluster represented 75 percent of observed events in the area, other events being distributed over the rift floor. Earthquake swarms were observed in the area, which are commonly related to movement of magma. The focal depths determined were considered shallow and it was suggested that the swarm activity was an expression of the present day seismic activity in the grid fault system. The study observed absence of seismic activity below 9km just beneath the cluster region strongly suggesting a lower crustal magmatic intrusion that applies upward pressure on the upper crust. All activity in the cluster region was found to be characterized by migration of hypocenters in time from south to north. It was suggested to have been caused by movement of earthquake trigger mechanism that is propagation of magmatic intrusion in the northern direction. In the axial direction, a locally up-warped brittle-ductile transition occurs at a depth of 15km in the south and 10km in the north. From

the study by Ibs-Von Seht *et al.* (2001), it was unclear whether this linear body of low shear strength represents a magmatic intrusion that could have triggered the swarm activity. There was need to make a follow-up to investigate the body causing high seismic activity in the area. If the body modelled has high density contrast and high susceptibility contrast, it may represent a magmatic body. Magmatic bodies at depth may have cooled with time, and therefore it is necessary to determine Curie- point depth. At this depth, rocks cease to be magnetic as they are at a temperature above Curie temperature. The magnetic method as an exploration tool depends on measuring accurately anomalies of local geomagnetic field, which occurs above the Curie point depth produced by variation in intensity of magnetization in rock formations. For magnetite, by far the major magnetic material, the Curie temperature is +575°C. In areas of high geothermal gradient, such a temperature may be reached at relatively shallow depth, which means that below this depth, rocks are not magnetic. Variation in intensity of magnetization can exist only at a temperature cooler than Curie point, which limits sources of magnetic anomalies to a maximum depth of 30 to 40 km. In mapping of hot magmatic intrusions for geothermal exploration, this method is particularly useful in that the hot rocks cease to be magnetic at Curie point depth, which can be modelled as the bottom of a magnetic body.

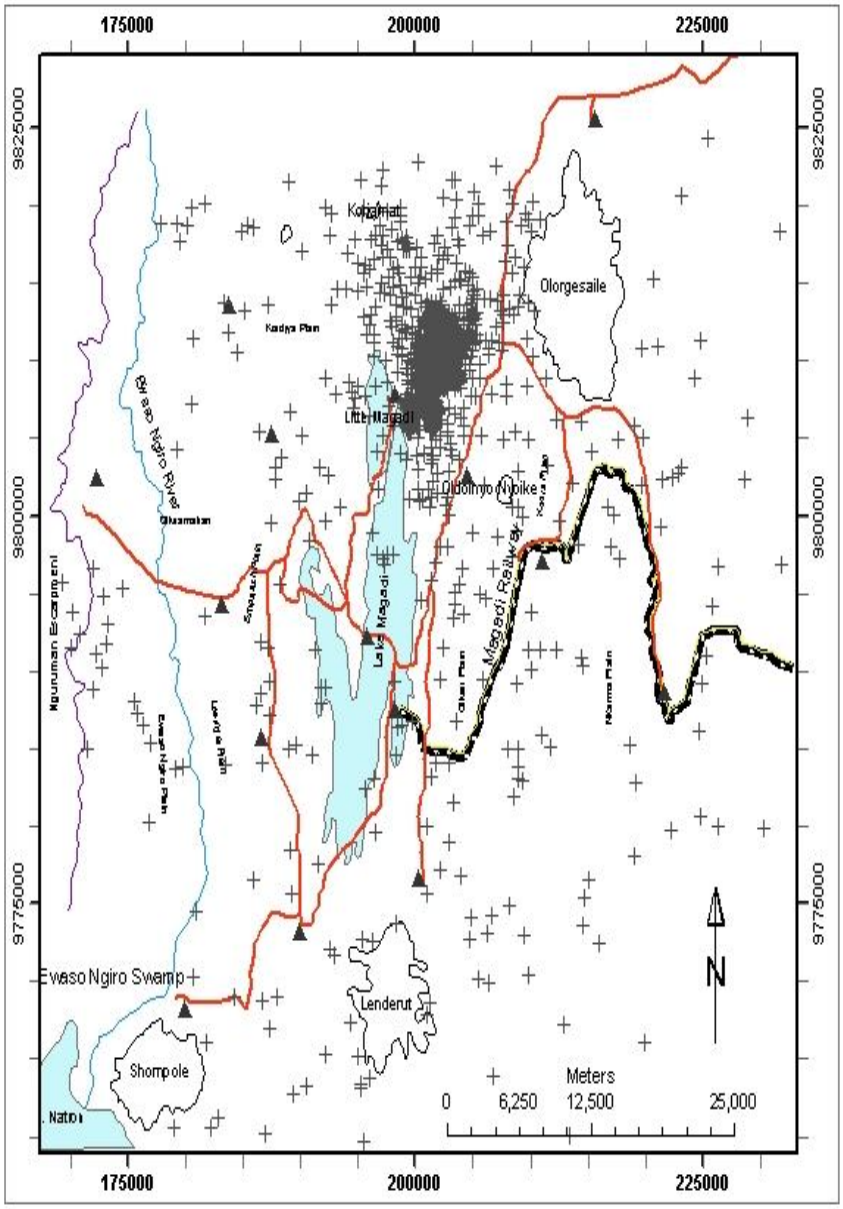

Figure 1.2: Distribution of earthquake epicentres in Magadi (after Ibs-Von Seht *etal*, 2001).

1.2 OBJECTIVES OF STUDY

The objectives of the proposed study are: -

- To undertake detailed ground magnetic and gravity surveys with a view to locating bodies at depth with sufficient magnetic susceptibility and density contrast, respectively, that may represent magmatic intrusions related to the tectonics of the area, hot springs and earthquake swarms.
- To construct 2-D gravity and magnetic models of any detected bodies that may be responsible for the existing seismicity and geothermal manifestations.
- To determine depth to the Curie isotherm beneath Magadi using magnetic data. Shallow isotherm depth may imply presence of a heat source at shallow depth and hence geothermal potential.

1.3 RATIONALE

Potential field data may be used in detection and delineation of geologic structures and crustal heterogeneities commonly associated with earthquake processes. This study is to be done with a view to model any bodies that may be causing high seismic activity in Magadi area using gravity and magnetic prospecting methods and investigate whether the bodies detected are possible heat sources. This may be important for the following reasons: -

(i) Detection of intrusives that may be hot bodies would be important in expanding the use of geothermal energy in Kenya. Steam produced by circulating water coming in contact with shallow hot rock bodies in the earth's crust can be utilized in the generation of electricity in geothermal plants and also for industrial heating in the soda factory.

(ii) Advancement of knowledge of the subsurface in Magadi area located 100 km southwest of Nairobi city can help in assessment and mitigation of earthquake risk. In earthquake prone areas, any decision for urban and regional planning rests on knowledge of the characteristics of future earthquakes. The estimation of seismic risk cannot be made solely on the basis of seismological data, which cover a period too short to reveal trends in earthquake activity. Other geophysical information correlated with seismological data may be used to establish criteria for delineation of earthquake origin zones.

1.5 GEOLOGY

The Magadi area is classified into three formations by Baker (1958, 1963) namely Precambrian metamorphic rocks, Plio-Pleistocene volcanics, the Holocene to Recent lake and fluvial sediments. The basement rocks outcrop in the region west of the Nguruman escarpment. These rocks consist mainly of regular banded schists, gneisses and muscovite-rich quartzites. The basement rocks are overlain by the Kirikiti platform, which is down faulted to the rift floor at the Nguruman escarpment. Baker (1958) found that the olivine basalt layers of the Kirikiti platform are interbedded with conglomerates; gravels and sands deposited between different eruption episodes.The area has three central volcanoes olorgesailie, Oldoinyo Nyokie and Shompole (Fig 1.3), Olorgesailie being the highest. Its lava composition consists of olivine basalts, alkali trachyte and nephelinite. Further south, Lenderut volcano dated 2.5 Ma has basalt and andesite lavas, while Shompole dated 2.0 Ma consists of carbonatite and nephelinite

rocks. The most extensive volcanic activity in the area occurred between 1.4 and 0.7 Ma (Crossley, 1979).

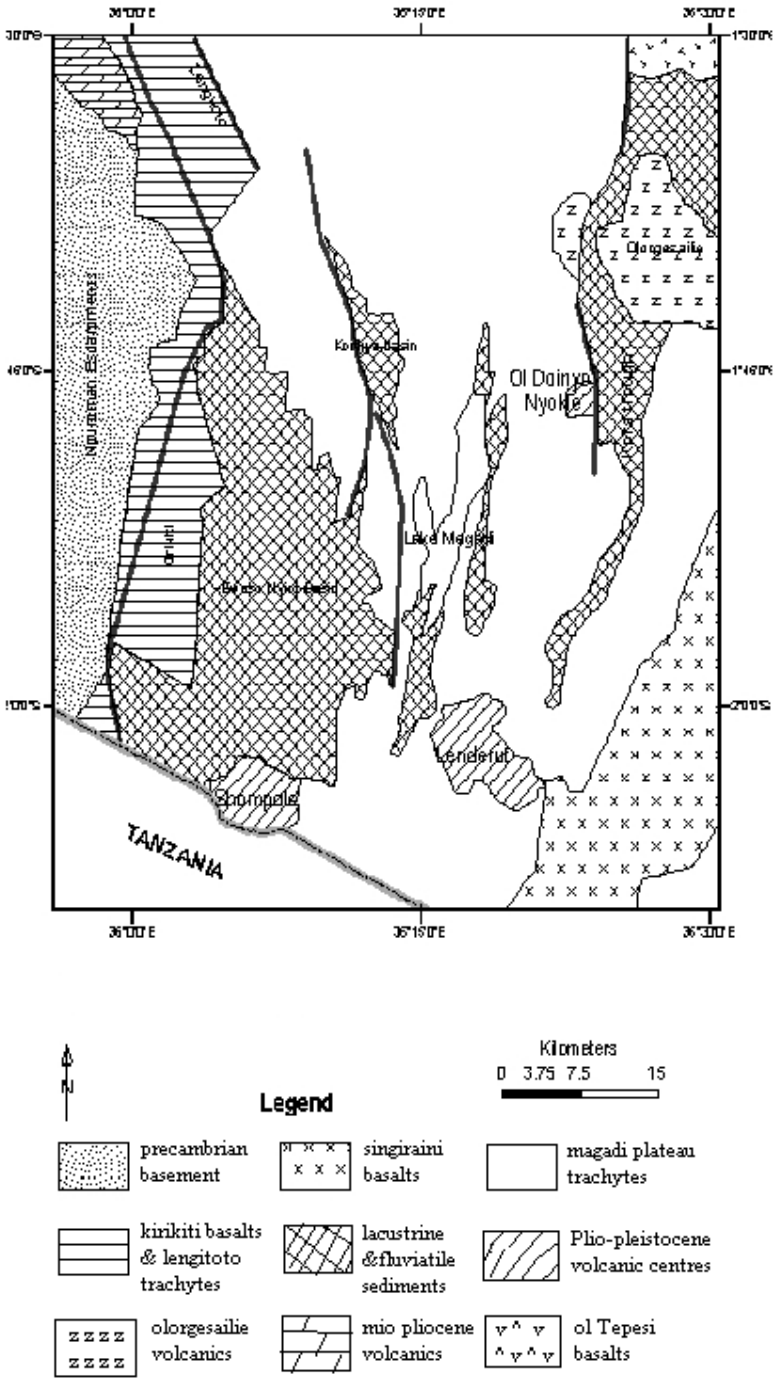

Figure 1.3. Geological map of Magadi (simplified from Baker, 1958, 1963)

During this activity the Magadi plateau trachytes series were formed. These consist of alkali lava sheets extending many kilometres that overlie most of the volcanics in the area. Formations of the Magadi plateau trachytes were closely followed by development of ash and lava vents and small obsidian lava volcano Oldoinyo Nyokie. This marked the end of volcanism in the southern Kenya Rift. The last geological formation in Magadi relates to lacustrine and fluviatile sediments. Lakebed lay in the bottom of fault troughs and depressions mostly covered by alluvial silts, clays and boulder beds. These are exposed in the region around Lake Magadi especially on the eastern trough of the lake. The fluviatile sediments are located in the Ewaso Ngiro basin. Other superficial deposits are the alluvium and soil filled Kordjya basin and Kora trough.

1.6. STRUCTURAL AND TECTONIC SETTING

Magadi area is situated in the southern part of the Kenyan Rift. According to Crossley (1979), volcanism in this segment of the rift began at 15 Ma and ceased by 0.8 Ma. The structural evolution took place from 7 Ma with the Nguruman fault activity with the area developing into an asymmetric graben between 4 Ma and 3 Ma. In the period from Pleistocene to Recent, faulting dissecting the rift floor increased in Magadi area when compared to other segments of the Kenyan Rift (Baker, 1986). Smith and Mosley (1993) subdivided the Kenya rift into three segments which are separated by major NW-SE trending ductile shear zones in the underlying Precambrian basement.

Integrated interpretation of geophysical data by Simiyu, (1996) as a geological cross-sectional model displays Magadi area as an asymmetric rift graben bordered in the western side by high angle faults of Nguruman escarpment. The basin fill which has a depth of 3.5 km against the Nguruman scarp to the west and 2.0 km to the east is divided into two parts by a horst structure located just beneath Lake Magadi. The southern segment which covers Lake Magadi area and extends to northern Tanzania developed on a craton type lithosphere. This was obscured by imbricated thrust slices and gravitationally collapsed nappes of the Tanzanian Craton and the Mozambique belt (Smith, 1994; Simiyu, 1996). Therefore this pre-existing framework might have influenced the structural geometry of this part of the rift by reactivation of NW-SE to NNW-SSE ductile and brittle Aswa-Nandi-Loita (ANL) shear zone which bounds Lake Magadi at its northern limit.

Structural analysis using spot image, aerial photos and fieldwork in Magadi area by Atmaoui, (1999) revealed important structural orientations features in the southern segment of the Kenyan rift corresponding to normal faults as displayed in figure 1.4. The size and space distribution of these faults is asymmetric within the western and eastern parts of the rift floor that are separated by the axial zone. The western part, which extends from Nguruman to Magadi depression, is affected by longer faults, which are widely spaced with vertical throws reaching 500 metres. The rift axis in the eastern part in comparison has relatively shorter faults, which become closely spaced on approaching the rift axis and have throws not exceeding 147 metres. North- south rift propagation is suggested by the decrease in fault length towards south.

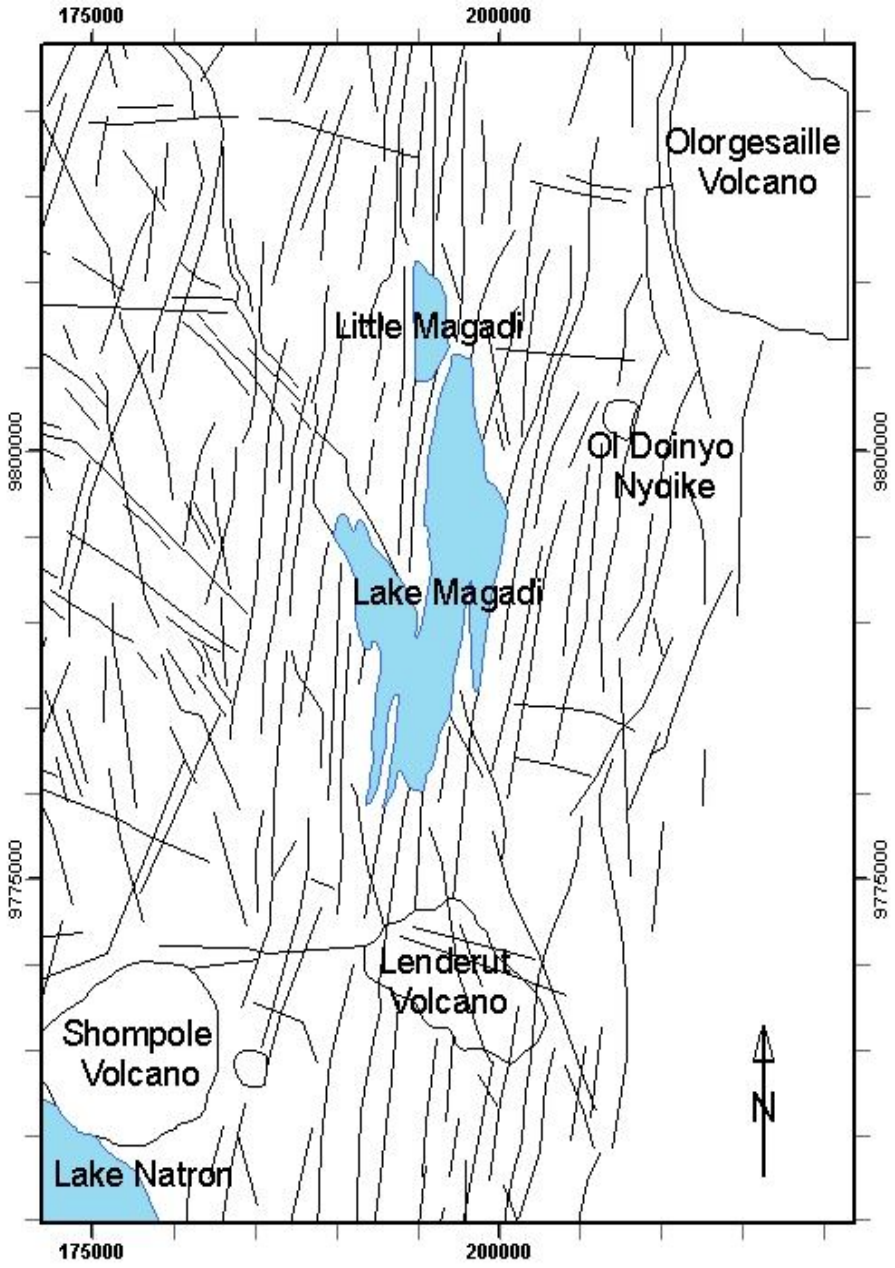
175000
200000
Olorgesaille
Volcano
Little Magadi
Ol Doinyo
Nyoike
Lake Magadi
9800000
9775000
Lenderut
Volcano
Shompole
Volcano
Lake Natron
N

Figure 1.4 Interpreted SPOT lineament map of Magadi (after Atmaoui, 1999).

1.7. PREVIOUS GEOPHYSICAL STUDIES

In the southern part of the Kenya dome, the Rift begins to lose graben-like appearance. The development of the Rift in the southern area is thought to be different from that in the north (Smith and Mosley, 1993; Smith, 1994). Below the southern part of the Kenya Rift, Mechie *et al* (1996) estimated, from Kenya Rift International Seismic Project (KRISP 90) data, that the onset of melting is at a depth of 50 ± 10 km, on the basis of anomalously low velocities interpreted to be caused by partial melt. Also for the southern Kenya Rift, seismic P-wave velocity information shows that the crust-mantle boundary outside the rift occurs at about 42 km depth (Bonjer et al., 1970; Maguire and Long, 1976). Beneath the Rift the crust-mantle boundary occurs at about 35 km depth (KRISP working group, 1987; Henry *et al*., 1990). Thus the crust-mantle boundary uplift is 5-7 km. In addition, low p-wave velocities (7.5 – 7.7 km/s) below the Rift has been detected where as outside the Rift, P-wave velocities appear to be normal (8.0 – 8.1 km/s) (Bonjer *et al*, 1970; Maguire and Long, 1976). This deduces the presence of partial melt in the low velocity zone of the mantle beneath the Rift. From long period magneto-telluric survey (LMT), (Simpson *et al*, 1997), in the southern part of the Kenya Rift, the Nguruman fault was clearly detected in additional enhanced conductivities, increasing to the north below the Rift graben itself. An anomaly below the Chyulu hills, where the structure is suggested to be 3-D, is inferred. A zone of partial melt seems the most likely explanation for this anomaly, which may correspond with the zone of lower seismic velocity modelled below the Chyulu south shot point. Williamson (1975) showed that the Kenya Rift axial high heat flow anomalies can in

part be modelled with young dyke intrusions into the axis of the Rift. The existence of such intrusions was predicted from gravity data (Baker and Wohlenberg, 1971). Intrusives in Magadi have been modelled as shallow prismatic dykes (Githiri *et al.*, 2004) and (Githiri *et al.* 2005). Healey (1975) explained that the source of heat in such a system is to be related to the concentration of intrusive dykes arising from an intra-crustal magma reservoir. A long wavelength of high gravity anomaly over the East African plateau was explained as due to the thinning of the lithospheric plate during the separation of East and West African tectonic plates (Girdler *et al.*, 1969). McCall (1967) detected gravity anomalies in the region between 0.15^0 N and 1.25^0 S. The anomaly has amplitude of 200 to 500 g.u and a width of 40 to 80 km. The anomaly suggests the presence of a body with positive density contrast likely to represent an intrusive zone of basaltic or gabbroic materials, which feeds the Rift volcanoes. The presence of the intrusive materials from the upper mantle suggests that crustal thinning has taken place. An extension of the survey was conducted by Searle (1970). Within the Rift Valley to the south, an area covering Menengai, Longonot and Suswa volcanoes, an axial high anomaly was detected but variable in width and amplitude which was explained to represent dense mantle derived intrusion 20 km wide extending from a depth of 20 km and a width of 2-3 km of the Rift floor. This represented extreme thinning of the lithospheric plate.

Gravity survey of Kenya conducted by Khan and Swain (1977) investigates the nature of the axial gravity high. The results were found to be associated with prominent volcanoes similar to those in the southern part of the Rift and showed that the Rift axis is associated with an intermittent narrow positive anomaly that runs from Lake Turkana

to Lake Magadi in the south. The major Rift boundary faults in Nguruman escarpment dates back to the earliest stage of Rift evolution (Baker 1958; Smith 1994). The grid faulting consists of a dense net of small scale, young, NNE trending faults that extend over the Rift floor obscured by young volcanic piles and sediments (Baker *et al.,* 1972). In Magadi and Hannington aeromagnetic survey (Wohlenberg and Bhatt, 1972), intrusive bodies were detected beneath extensive lava flows covering the Rift floor. In the Magadi aeromagnetic survey, strong magnetic anomalies were observed on the eastern border near Olorgesailie and on the north near Suswa volcanoes. A comprehensive analysis of Lake Magadi aeromagnetic survey data was done by Wolff (1992) from which several magnetic anomalies were detected near Nguruman and Olorgesailie. Most of the anomalies were interpreted to represent shallow magnetic bodies extending to depths ranging between 3.5 – 15 km.

Local seismic activity has been monitored in the southern part of the Kenya Rift around Lake Magadi. The background seismic activity of Magadi area is at least 10 events per day, (Ibs-Von Seht *et al.*, 2001). It occurs at depths greater than 10 km and can be assigned to the Rift boundary faults and faults buried under the volcanic Rift infill. An earthquake cluster caused by swarm activity occurred in the Rift centre at shallow depth and was associated with the grid fault system. The hypocenter depth distribution shows large depths of up to 27 km in the south and much shallower depths of 1 km in the northern part of the area. Other than the background activity, swarm activities with rates of more than 300 events per day were recorded. The epicentres are clustered and trace a linear structure lying SSW-NNE over a length of 10 km north of Lake Magadi. The stress field of the southern Kenya Rift is directed WNW –ESE. The fault plane

solutions indicate a predominantly normal fault. Most fault planes are aligned parallel to the graben axis. The clearest expression of present day seismic activity in connection to rifting is the observed earthquake swarm, which was probably triggered by magma movements.

CHAPTER TWO

MAGNETIC AND GRAVITY METHODS

2.1 THEORY OF MAGNETIC METHOD

2.1.1 Elements of the earth′s magnetic field

The direction and magnitude of the geomagnetic field at any part of the earth′s surface are represented by a vector parallel to the direction of the field, pointing in the direction of force on a positive pole, and having a length proportional to the strength of the field at that point. Among the magnetic elements, the direction of the field is the element least sensitive to changes in the dimensions and magnetic properties of the subsurface body. The various magnetic elements are B_Z, B_H, B_T, D and I, which describes the earth′s magnetic field. These elements are represented in the parallelepiped in Figure 2.1. The angle between the magnetic and geographic meridians is the magnetic declination D while that between the total geomagnetic field vector and the horizontal plane is the magnetic inclination I. These geomagnetic elements vary all over the earth′s surface. The line where inclination I is zero is the magnetic equator and points where the inclination is +90° and -90° are the north and south magnetic poles, respectively.

The total field vector B_T has a vertical component B_Z and a horizontal component B_H in the direction of the magnetic north. The vertical component B_Z is positive north of the magnetic equator and negative south of it (Parasnis, 1986). The dip of B_T is the inclination I of the field. B_T varies in strength from about 25,000 nT in equatorial regions to about 70,000 nT at the magnetic poles.

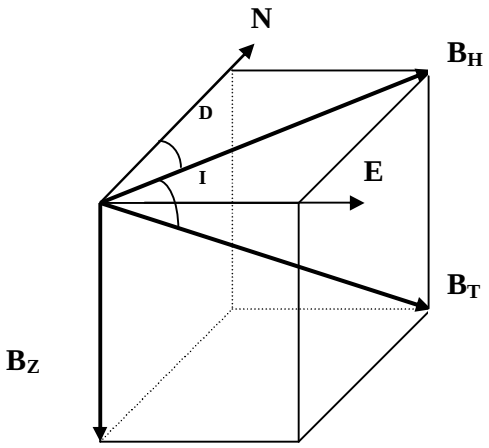

B_T = Total intensity vector

B_Z = Vertical component of the geomagnetic field

B_H =Horizontal component of the geomagnetic field

D= Angle of declination

I= Angle of inclination

E= Geographic East

N= Geographic North

Figure 2.1 Geomagnetic Elements.

The total magnetic field, its horizontal and vertical components are related by equation 2.1.

$$B_T^{\,2} = B_H^{\,2} + B_Z^{\,2}, \qquad \text{---------- (2.1)}$$

where B_H is the intensity of the horizontal component. The magnetic inclination is the vertical angle between the total magnetic intensity vector and the horizontal plane as expressed by equation 2.2.

$$I = Arc\tan\left[\frac{B_Z}{B_H}\right] \qquad \text{---------- (2.2)}$$

But from equation 2.1, $B_H = \left[B_T{}^2 - B_Z{}^2\right]^{\frac{1}{2}}$, and substituting this expression in equation 2.2, then it can be expressed as equation 2.3.

$$I = Arc\tan\left[\frac{B_Z}{\left(B_T{}^2 - B_Z{}^2\right)^{\frac{1}{2}}}\right] \qquad \text{---------- (2.3)}$$

The magnetic inclination can be determined by substitution of measured values of B_T and B_Z in equation 2.3.

2.1.2. Geomagnetic field

The geomagnetic field of the earth, is the magnetic field which can be measured at any part on the earth′s surface. The magnetic field on the earth at a given place and time may be considered to consist of three parts. These are the main field, which is slowly changing, a diurnal part that changes with time, which is approximately repeated in daily cycles, and the anomaly part caused by inhomogeneities of the earth′s crust.

The main field is the undisturbed component of the earth′s field, which to the first approximation can be mathematically represented as a dipole field. The origin of the main field and its secular variation is the earth′s core according to accepted theories by Elasser (1956) and Bullard (1949). It seems probable that the main field is caused by

electric currents in the earth′s liquid core below about 2,900 km. By slow convective movements, electric currents are produced in the core; these maintain the magnetic field, as in a self-exciting dynamo. Large scale eddies in the convective motion produce the regional features of the main field, and their changes produce the secular magnetic variation. According to this theory, the geomagnetic field will remain of mainly dipole character nearly down to the surface of the core, with the lines of magnetic force lying nearly in planes through the geomagnetic axis. The magnetic intensity will increase inversely as the cube of the distance from the centre. There is a reaction between the magnetic field and the electric currents in the core, that tends to produce a westward drift of the core and hence of the secular magnetic variations relative to the outer solid part of the earth. This is reflected in a slow progressive, temporal change in all the geomagnetic elements (David, 1981).

Diurnal variations are small but more rapid oscillations in the earth′s field with a periodicity of about a day and amplitude averaging 25 nT (Dobrin, 1988). The fast variations of the magnetic field that takes place within the course of the day are connected with phenomena occurring on the sun. These variations are influenced by conditions in the atmosphere. Normally, steady ring currents are present in the ionosphere. In addition, the outer layers of the sun ‘corona’ erupt occasionally emitting corpuscular rays consisting of protons and electrons. When the corpuscles impinge upon the ionosphere, the ring currents are greatly disturbed and this affects the magnetic field of the earth (Fukushima and Kaminde, 1973).

The magnetic anomaly consists of that part of the magnetic field which is caused by irregularities in the distribution of magnetized material in the outer-crust of the earth. The magnetized rock produces a magnetic field around itself. If the rock is close enough to the earth′s surface, its magnetic field will combine with the earth′s field. The field from the rock constitutes the anomalous field and because fields are vectors, the combined field may be greater or smaller than the geomagnetic field acting alone. If the field from the magnetized body lies more or less in the same direction as the earth's magnetic field at the site, the two fields will reinforce each other, and the total field will be greater than the earth's field alone and the resulting anomaly is a positive anomaly. If the two fields are opposite in direction, they will cancel each other and the total field will be smaller than the earth's field alone, the resulting anomaly being negative. A magnetic anomaly is detected when the measured magnetic field at the earth′s surface differs from the undisturbed geomagnetic field. This implies the presence of a magnetized material below the subsurface. All magnetic anomalies caused by rocks are superimposed in the main field of the earth.

2.1.3. Rock magnetism

When a rock is in a magnetic field, it may acquire a magnetization in the direction of the field, which is lost when the rock is removed from the field. This is called induced magnetization and is due to alignment of the dipoles in the rock in the direction of the field. The induced intensity of magnetization M_i of a material is directly proportional to the magnetizing force H of the induced field. In small fields with magnitude compared to the earth's magnetic field the relationship between induced magnetisation and applied magnetic field is linear as represented in equation 2.4.

$$M_i = \chi H \quad \text{---------- (2.4)}$$

where χ is the magnetic susceptibility of the material, which is a dimensionless constant. Most minerals constituent in rocks have low magnetic susceptibilities. The magnetism in rocks is therefore as a result of proportions of magnetic minerals they may contain. The most common magnetic mineral is magnetite and hence its proportion determines magnetic behaviour of rocks. Basic igneous rocks have relatively high magnetic susceptibility as compared to acidic igneous rocks due to their high magnetite content while it is even far lower in metamorphic rocks. Sedimentary rocks are usually non- magnetic. Magnetic anomaly over sedimentary rocks may be due to an underlying magnetic basement or due to intrusions on the sediments. The magnetite content, which determines the susceptibility of rocks, is variable and there can be overlap between different rock types. It may therefore not be possible to identify uniquely a rock type from its magnetic susceptibility.

A rock sample may contain thousands of ferromagnetic mineral grains. In strong fields, the magnetization reaches a saturation value at which individual magnetic moments are aligned with the applied field. When the magnetizing field is removed, the sample may retain part of the induced magnetism. This permanent magnetization is called remanent magnetisation, denoted by M_r. Remanent magnetisation in a rock is not only a function of chemical makeup but also geologic and thermal history (Blakely, 1995). The total magnetisation of a rock denoted by M is the vector sum of its induced and remanent magnetisation, expressed as:

$$M = M_i + M_r \quad \text{---------- (2.5)}$$

Igneous rocks solidify at temperatures above 1000°C. At this temperature, the grains are solid and fixed in a rigid matrix. The grains of a ferromagnetic mineral are above their Curie temperature, which is 578°C for magnetite and 675°C for hematite. The individual atomic moments point different directions and magnetization is hence paramagnetic. On cooling through Curie point temperature, the magnetic state of the magnetite grains change from paramagnetic to ferromagnetic. On further cooling, magnetizations in the magnetite grains become blocked along directions of magnetization close to the field direction. The resultant thermo-remanent magnetization is parallel to the field direction. According to Kearey and Brooks, (1984) magnetic anomalies are commonly caused by dykes, lava flows, basic intrusions, metamorphic basements and magnetic ore-bodies. Magnetic anomalies range in amplitude from few tens of nanoTeslas over deep metamorphic basement to several hundred nano-Teslas over basic intrusions and may reach several thousands nano-Teslas over magnetic ore-bodies.

2.2 THEORY OF GRAVITY METHOD

From the Newton's law of universal gravitation, the force F between two point masses M_1 and M_2 separated by a distance r is expressed as

$$F = \frac{GM_1M_2}{r^2}, \quad \text{---------- (2.6)}$$

where G is the universal gravitational constant equal to 6.67×10^{-11} Nm^2kg^{-2}. The force acting on a mass M_2 in the gravitational field of another mass M_1 is also given by

$$F = M_2 a, \quad \text{---------- (2.7)}$$

and, therefore, the expression for acceleration is

$$a = \frac{GM_1}{r^2}. \qquad \text{---------- (2.8)}$$

The gravitational acceleration of an extended body can be obtained by dividing it into point masses and vector addition of their corresponding accelerations. The density ρ is generally a function of the position. Since $dm_i = \rho_i dv_i$ acceleration, a_i, of the point mass is expressed as

$$a_i = \frac{Gdm_i}{r_i^2} = \frac{G\rho_i dv_i}{r_i^2}, \qquad \text{---------- (2.9)}$$

where dm_i, ρ_i, dv_i are mass of the point mass, its density and volume, respectively.

In general, the gravity anomaly of any shape can be determined by summing the attractions of all the mass elements, which make up the body. Figure 2.2 shows a prismatic element of an extended body of density ρ, located at x', y', z', with sides of length δx', δy', δz'. The mass δm of this element is given by,

$$\delta m = \rho \delta x' \delta y' \delta z'. \qquad \text{---------- (2.10)}$$

The attraction δg at a point outside the body of coordinates (x, y, z) a distance r from the element as derived from equation 2.9 is

$$\delta g = G\rho \frac{(z' - z)}{r^3} \delta x' \delta y' \delta z'. \qquad \text{---------- (2.11)}$$

The anomaly of the whole body (Δg) is found by summing all such elements that make up the body

$$\Delta g = \sum\sum\sum G\rho \frac{(z' - z)}{r^3} \delta x' \delta y' \delta z'. \qquad \text{---------- (2.12)}$$

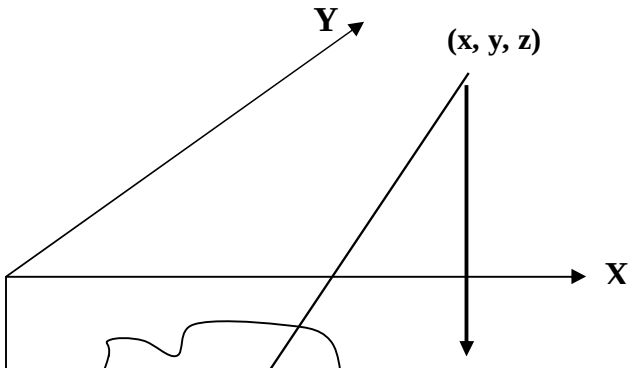

Figure 2.2. Gravitational attraction of a mass element.

If δx', δy'and δz' are allowed to approach zero, that is the size of the volume elements becomes infinitesimal, the summation is replaced by the integration over the volume of the body and the anomaly is expressed as

$$\Delta g = \iiint G\rho \frac{\left(z' - z\right)}{r^3} \delta x' \delta y' \delta z' , \qquad \text{---------- (2.13)}$$

where $r = \left[\left(x' - x\right)^2 + \left(y' - y\right)^2 + \left(z' - z\right)^2\right]^{\frac{1}{2}}$.

Attraction of bodies of regular geometry can be determined by integrating equation 2.13 analytically while anomalies of irregularly shaped bodies are calculated by numerical integration of equation 2.12.

The gravity prospecting method involves measuring variations in the earth's gravitational field caused by changes in density of the earth. This method can be used to outline major structural features. A gravity survey provides the distribution of

gravity field on a reference surface. The gravity curve, presents the regional as well as the residual anomalies, which are the base for the interpretation of buried bodies. After all the usual corrections, the Bouguer anomaly represents the attraction due to density differences within the earth. Gravity anomalies can be positive, when density of the anomalous bodies is higher than the surrounding medium or negative when density is lower.

CHAPTER THREE

FIELD WORK AND DATA PROCESSING

3.1 INTRODUCTION

The first step in field work involved setting up of stations from which both the gravity and magnetic fields would be measured. Establishment of stations in a regular grid network would have been most ideal. This was not possible especially in the north-western part of the study area due to rough terrain inaccessible to vehicles. Such areas of rough terrain mostly with steep fault scarps were accessed by walking. Most of the stations were set along motorable tracks to allow fast return to the base station for monitoring of instrumental drift and diurnal variations. The equipments used in the survey were a Global Positioning System (Mangellian) for measuring station location coordinates and altitude, a Worden gravimeter (Prospector- 410), a proton precession magnetometer (Geometrics-856) and a flux-gate magnetometer model scintex.

3.1.1 Field equipment.

3.1.1.1 Worden gravimeter

A gravimeter is an instrument used in measuring relative values of gravity. A gravimeter consist of a spring balance carrying a constant mass and variations in the weight of the mass caused by gravity change causes the length of the spring to vary. The essentials of a Worden gravimeter are a very lightweight mass 5 mg and main zero spring coupled to its upper end to two subsidiary springs. The springs are of different strengths and each is attached to a micrometer. The system is held in unstable equilibrium about axis H-H as shown in the Figure 3.1. Any increase in gravitational pull causes a slight anticlockwise rotation angle between the main spring and the

inclined arm attached to its base. The decreased angle lessens the opposing clockwise moments of spring and provides necessary instability. The upper end of the main spring is attached to micrometers through two springs. The micrometers measure the displacement needed to restore the beam to its null position on its scale. One of this micrometer dials has a scale, which is adjusted to the order of 100 mgal in range and can be read to 0.01 mgal. The other is a geodetic dial having a range of several thousand milligals but can read to an accuracy of 0.2 mgal. The geodetic dial is used for measurement of large gravity differences and is a coarse adjustment used for bringing the small dial on scale when gravimeter is moved to different latitude.

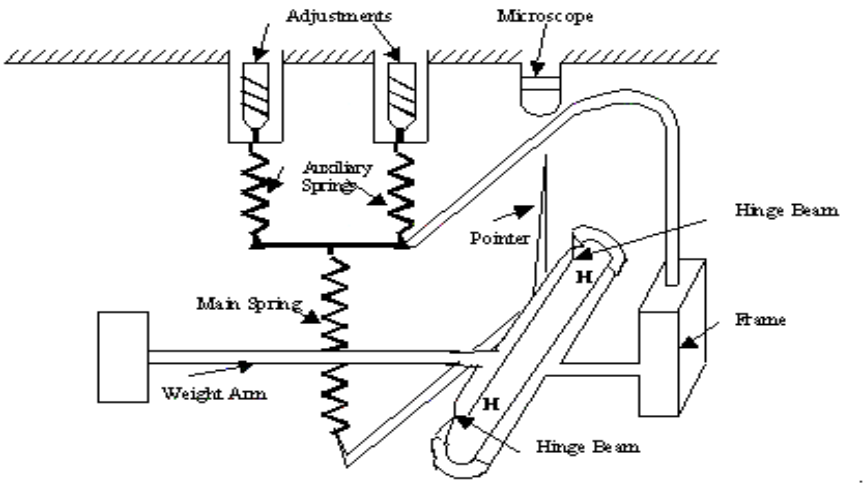

Figure 3.1. Schematic diagram Worden Gravimeter (after Dobrin, 1988).

Large deflections of the gravimeter would be produced by effect of temperature on the spring. In the Worden gravimeter, temperature effects are minimized by using quartz springs and a bimetallic beam, which compensates for temperature changes

automatically. The instrument is housed in an evacuated flask. The instrument can be read to an accuracy of 0.01 milligals.

3.1.1.2. Proton precession magnetometer

A magnetometer is an instrument for measuring the intensity of the earth's magnetic field. The proton precession magnetometer has a sensor containing a liquid rich in hydrogen atoms such as water or decane. The hydrogen nuclei in the liquid act small dipoles and normally align parallel to the ambient geomagnetic field B_e. A current is passed through the coil to generate a magnetic field B_p approximately 50 to 100 times larger than the geomagnetic field and in opposite direction. This causes the protons to align to this new direction. The current in the coil is then switched off so that the polarizing field is removed. The protons return to their original alignment with B_e precessing, in phase around this direction with a period of about 0.5 ms. The frequency of this precession is given by

$$f = \gamma_p \frac{B_e}{2\pi} , \quad \text{---------- (3.1)}$$

where γ_p is gyromagnetic ratio of the proton, which is a constant. The precession frequency is measured by a digital counter as the absolute value of the total magnetic intensity to an accuracy of ±1 nT. In a proton precession magnetometer, the total intensity measured as the frequency of precession is independent of the orientation of the sensor. The amplitude of the signal, however, does vary as $\sin^2\theta$ with θ being the angle between the direction of the applied field within the sensor and the earth's field direction. Ideally, the applied field in the sensor should be at right angles to the earth's field direction. For maximum signal amplitude, the toroidal sensor of the magnetometer is held with its axis vertical in a vertical field, and pointing north in an equatorial field.

3.1.1.3. Flux-gate magnetometer

The flux gate magnetometer consists of two ferromagnetic cores of very high susceptibility aligned in the direction of the earth's field. The two high permeability strips are wound with separate coils in opposite directions and are energized by an a.c source of about 1000 Hz with magnetization of the two coils being in opposite directions. These two coils are enclosed together in another coil carrying direct current as illustrated in figure 3.2. If there is no external magnetic field, the distortion of the magnetizing winding of the two coils will be equal and opposite resulting in no output from the pulse transformer.

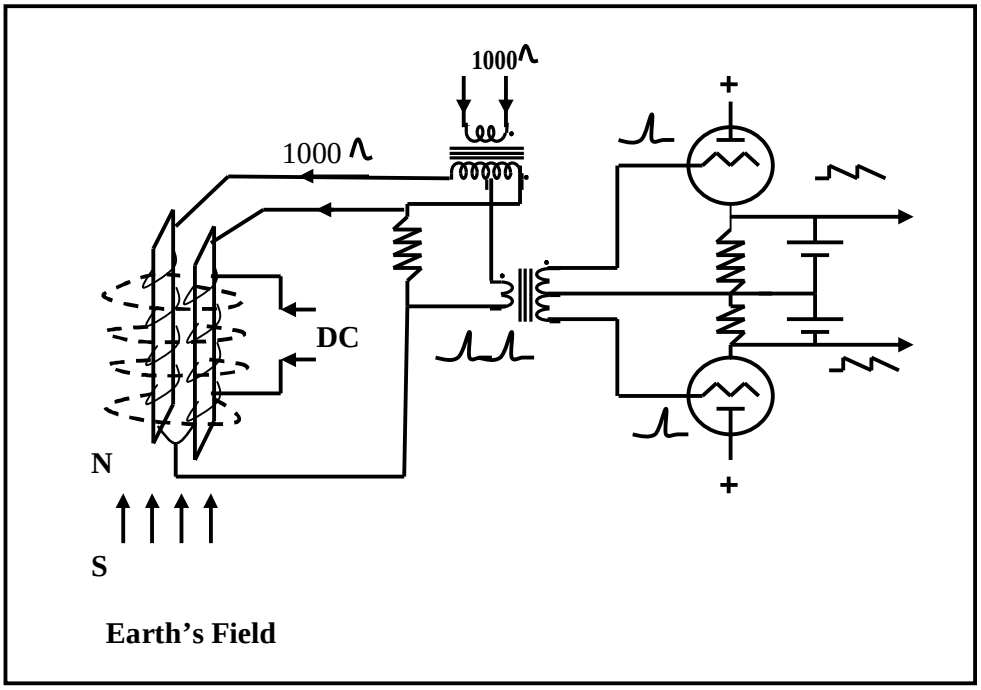

Figure 3.2. Schematic diagram of a Flux-Gate magnetometer.

In the presence of an ambient magnetic field, the hysteresis curves of the two strips are displaced in opposite directions. The pulses from the two windings no longer balance each other and there is net output pulse to the amplifier. The net output pulse is proportional to the ambient magnetic field intensity at the magnetometer element. This net output activates a balancing circuit, which changes the current in the d.c coil bringing the net field to zero. The change in the d.c balancing current is recorded digitally (Nettleton, 1976). The instrument measures the vertical component of magnetic field (Z) at an accuracy of ±1 nT.

3.2. FIELD PROCEDURES

3.2.1. Magnetic measurements

Establishing and positioning of magnetic stations including base stations was done using a Global Positioning System (GPS). A total of 58 magnetic stations were established. The total magnetic field intensity was measured at each station using a proton precession magnetometer. The vertical component of the magnetic field was also measured using a flux gate magnetometer in selected stations in order to determine the magnetic inclination of the study area. Magnetic measurements were not made near magnetic objects. A safe distance of about 150 meters was observed from such objects like bridges, railway-lines, tarmac roads and high voltage power lines. The observer when taking magnetic measurements also ensured that he was free of any magnetic material. On each day, repeated magnetic readings were carried after a period of about one hour at the base stations in order to monitor diurnal variations. From the raw magnetic data collected, diurnal corrections were carried out from observed magnetic field readings at the base stations.

3.2.2 Gravity measurements

The relative gravity measurements were carried out in the 58 established stations previously used in magnetic survey. All gravity measurements were taken using a Worden gravimeter. A local base station was established at an easily accessible location. Readings were taken at the same base station at least three times a day to monitor the instrumental drift. The gravity values of all stations measured in a day were plotted against the time of measurement. Points representing the preoccupied base station were joined with lines. The drift correction was hence the difference in gravity between measured station reading and that at the base station interpolated along a line to the same time the field measurement was made. The gravity difference was subtracted from each field measurement conducted in the day.

The absolute gravity values at survey stations were obtained by reference to the International Gravity Standardization Network (IGSN) (Morelli *et al.*, 1971) which consists of a network of stations at which the absolute values of gravity measurements have been determined. By using a gravimeter to determine the difference in gravity between an IGSN station and a field station, the absolute gravity value at the field station was determined. The calibration of this gravimeter was done by measuring gravity differences between two stations in Magadi labelled as B1 and A2 of gravity values 9777412 g.u and 9777470 g.u, respectively, which had been established in a previous gravity survey in Magadi by Githiri *et al*. (2005). These stations readings had been previously referred to the Nairobi pendulum station (IGSN 71) (Morelli *et al.*, 1974), station '35716 A', with an absolute gravity value of 9775260.7 g.u. However,

IGSN71 values include a correction of the Honkasalo term (Honkasalo, 1964) which removes the average part of the tidal force. This correction term has been deemed inappropriate (Heikkinen, 1979) because of resulting errors in calculation of the geoid from gravity values corrected with the Honkasalo term. Therefore, following the recommendations of the International Association of Geodesy (Uotila, 1980), the Honkasalo term, Δg_h, was removed from all the observed gravity values that had been referenced to the IGSN71 station. This was done by adding a latitudinal varying correction in milligals given by

$$\Delta g_h = 0.0371\left(1 - 3\sin^2 \varphi\right), \quad \text{---------- (3.2)}$$

Where φ is the latitude south or north of the gravity station. This correction was done by adding Δg_h to the observed gravity values using Microsoft excel spreadsheet.

Gravity measurements data from previous surveys covering the study area were also used in this survey and all the stations are displayed in figure 3.3. The stations labelled L1-L20 were extracted from the catalogue of gravity measurements in Kenya (Khan and Swain, 1977) whose source of data was the Leicester University surveys. All these measurements had been done with a La Coste and Romberg gravimeter G-16 and referenced to Nairobi pendulum station 35716 A with an absolute gravity value of 9775260.7 g.u. The gravity values in stations labelled WA were extracted from previous study (Githiri *et al*, 2005).

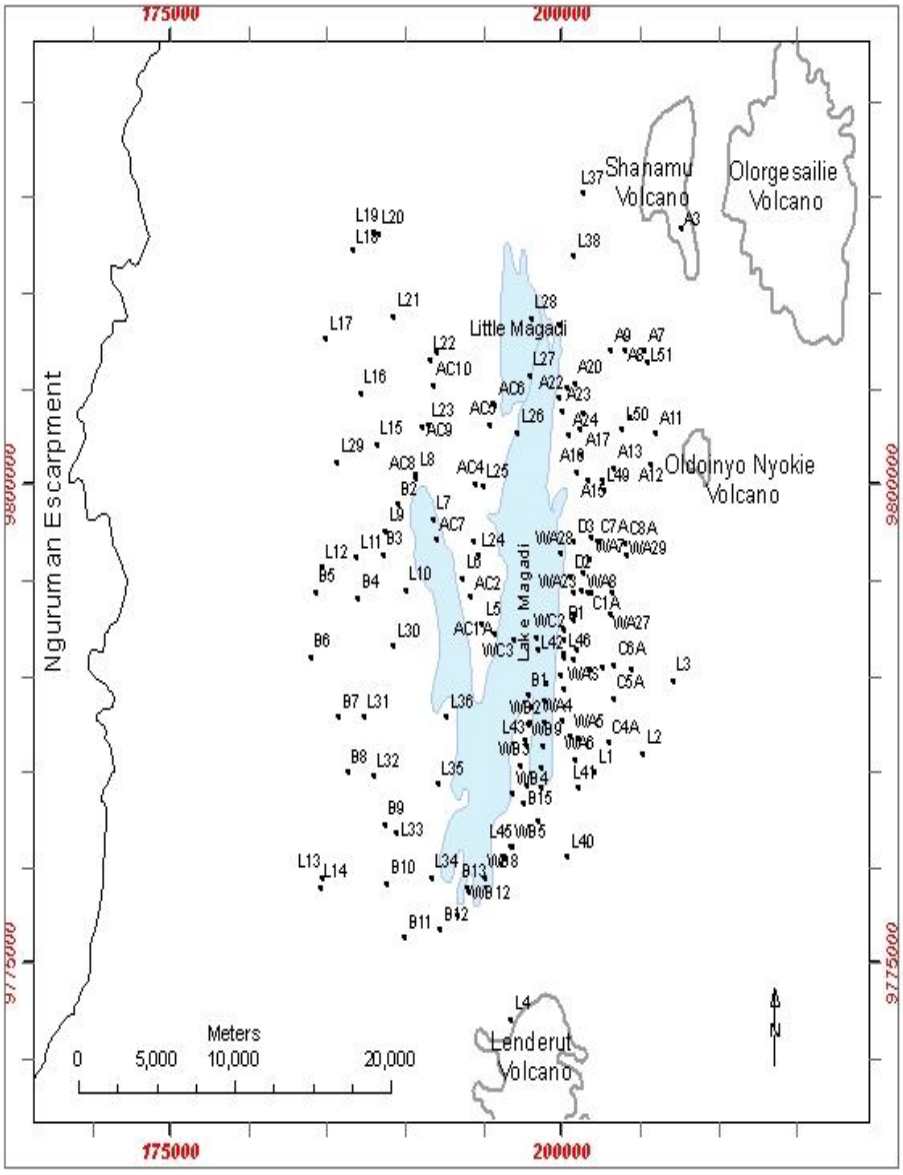

Figure 3.3 Magnetic and gravity station distribution.

1.4 3.3. DATA PROCESSING

3.3.1. Gravity data reduction

Raw gravity data are affected by a variety of effects that mask the variations due to geological bodies of interest. The raw gravity data were therefore corrected for terrain, latitude, free-air, Bouguer slab, tides and instrumental drifts. The Bouguer anomaly achieved after the removal of these effects was the contribution due to density variations in the subsurface.

3.3.1.1. Ellipsoid theoretical gravity

The theoretical or normal gravity accounting for the shape, mass and the rotation of the earth is the predicted gravitational acceleration on the best fitting terrestrial ellipsoidal surface. The 1980 Geodetic Reference System (GRS80) (Moritz, 1980) was used in computing the normal gravity. The Somigliana formula (Somigliana, 1930) for the theoretical gravity g_T was used,

$$g_T = \frac{g_e\left(1 + k\sin^2\varphi\right)}{\left(1 - \varepsilon^2\sin^2\varphi\right)^{1/2}}, \qquad \text{---------- (3.3)}$$

where the GRS80 reference ellipsoid has the normal gravity at the equator (g_e) equal to 978032.67715 mgal, k =0.001931851353 and ϵ^2 =0.0066943800229, where ϵ is the first numerical eccentricity. The theoretical gravity was calculated using this equation in Microsoft excel spreadsheet for each station latitude φ.

3.3.1.2. Free air corrections

The free air anomalies, Δg_h, were computed from the second order approximation formula (Heiskanen and Moritz, 1969) in order to correct the theoretical gravity for a height (h) relative to the ellipsoid expressed as

$$\Delta g_h = -2\frac{g_e}{a}\left[1 + f + m + \left(-3f + \frac{5}{2}m\right)\sin^2\varphi\right]h + \frac{3g_e h^2}{a^2}, \quad \text{---------- (3.4)}$$

The following parameter values for the GRS80 ellipsoid were used: (a), the semi major axis, is 6378137 m; (b), the semi minor axis, is 6356752.3141 m; f, flattening, is 0.003352810681; g_e is 9.7803267715 m/s^2; and m, which is $\omega^2a^2b^2/GM$, is 0.00344978600308, where ω is the angular velocity ($7292115x10^{-11}$ radians/sec) and the product GM is 3986005 x 10^8 m^3s^2. The second order formula for the GRS80 ellipsoid,

$$\Delta g_h = -\left(0.3087691 - 0.0004398\sin^2\varphi\right)h + 7.2125x10^{-8}h^2, \quad \text{---------- (3.5)}$$

where the ellipsoidal height h is in metres and the gravity effect is in milligals. The free air corrections, Δg_h, for each station were calculated using Microsoft excel spreadsheet with its corresponding altitude h and latitude φ.

3.3.1.3. Density determination by Nettleton's method

The near surface density was determined by a method devised by Nettleton, L. L (1939). This method is limited in flat areas and is successful in areas where near surface lithology is homogeneous and gives information to relatively shallow depth. In this method, the shape of the Bouguer anomaly is compared to that of topography plotted

across a hilly profile. In Nettleton's method, the value of density that gives a gravity profile with least or no correlation to topography was considered the correct density.

A profile was made across a hilly portion of the study area on a contour map of combined elevation and terrain corrections, which are density dependent. At each observation point, the gravity effect of the feature was calculated with different density values and this effect removed from the observed gravity at that point. A cross-section of topography of the same profile was plotted. The shape of the Bouguer gravity anomalies corresponding to different densities was compared to the shape of topography along the profile. From the results plotted in figure 3.5 (a) and (b), least correlation was observed on the closely overlapping graphs of densities 2600 Kgm^{-3}, 2670 Kgm^{-3} and 2700 Kgm^{-3}. A choice of 2670 Kgm^{-3}, as an average crustal density was considered appropriate for gravity corrections in this study. This density value has previously been used in gravity reductions in the Kenyan rift valley.

3.3.14. Bouguer corrections

The Bouguer correction accounts for the gravitational attraction of the layer of the earth between the ellipsoid and the station. This correction, in milligals, is calculated by assuming the earth between the vertical datum and the station to be represented by a horizontal slab with the equation

$$\Delta g_{bc} = 2\pi G\sigma h = 4.193x10^{-5}\sigma h, \qquad \text{---------- (3.6)}$$

where G, the gravitational constant, is 6.673± 0.001 x 10^{-11} $m^3/kg/s^2$ (Mohr and Taylor, 2001), σ is the density of the horizontal slab in kg/m^3, and h is the height of the station in metres relative to the ellipsoid. The Bouguer slab correction, Δg_{bc}, was calculated for

each station using Microsoft excel spreadsheet with its corresponding altitude h and an average crustal density of 2670 kgm^3.

3.3.1.5. Terrain corrections

The gravity effect of departures of topography from the assumed horizontal slab or spherical cap used in carrying out Bouguer corrections is referred to as the terrain corrections. The simple Bouguer correction assumes that the topography around the station is flat. Presence of valleys causes deficiency in gravity, which is not taken care of in the horizontal plane calculation. The Bouguer correction has been overcorrected and must be restored by a positive terrain correction. The presence of a hill causes an upward pull, tending to decrease gravity, which is not taken account of by the Bouguer correction. Its attraction must be corrected by a positive terrain correction.

The terrain corrections were carried out using a Hammer chart (Kearey and Brooks, 1984) constructed to a maximum radius of 5 Km for all stations. This was done using the topographic map sheets numbers 160/1, 160/2, 160/3 and 160/4 published by Survey of Kenya to a scale 1:50,000. The Hammer chart drawn on a transparent sheet was overlaid on a topographic map at the same scale and centred on the gravity station. The average elevation within each compartment was estimated as accurately as possible and the elevation difference (h) of the sector relative to the station determined. This procedure was repeated for each gravity station. Using a software TERRAIN version 2.2, (NOCK, pers., comm.) the terrain corrections at a gravity station were obtained by summing up the contribution of all the zones of the Hammer chart. The software is based on the terrain correction formula

$$T = \frac{0.4191*10^{-3}\sigma}{n\left\{r_2 - r_1 + \sqrt{r_1^{\,2} + z^2} - \sqrt{r_2^{\,2} + z^2}\right\}}, \qquad \text{---------- (3.7)}$$

where T is the terrain correction of a compartment in g.u, σ is the Bouguer correction density in kg/m^3, n is the number of compartments in a given zone, r_1 is the inner radius of a zone in metres, r_2 is the outer radius of a zone in metres and z is the modulus of elevation difference between observation point and mean elevation of a compartment in metres. The input data in the software is the terrain density, station code, station elevation and average elevation of each compartment of each zone. The inner zones were combined as D and other zones used for terrain correction were E, F, G, H, I and J. Gravity values calculated for each compartment in microgals were summed up for all zones and presented as terrain correction for a particular station.

A density of 2670 kg/m^3 was used to correct for all the stations in the study area. The total gravity correction yielding the complete Bouguer anomaly is defined by

$$g_b = g_o - g_\theta + g_{fa} - g_{sb} + g_{ter}, \qquad \text{---------- (3.8)}$$

where g_b is the complete Bouguer anomaly, g_o is the observed absolute gravity, g_θ is the theoretical sea-level gravity, g_{sb} is Bouguer slab correction, g_{fa} is free-air correction and g_{ter} is the terrain correction. The values of Bouguer anomaly together with pre-existing gravity measurements from the area was incorporated to form dense networks from which a Bouguer anomaly contour map was plotted.

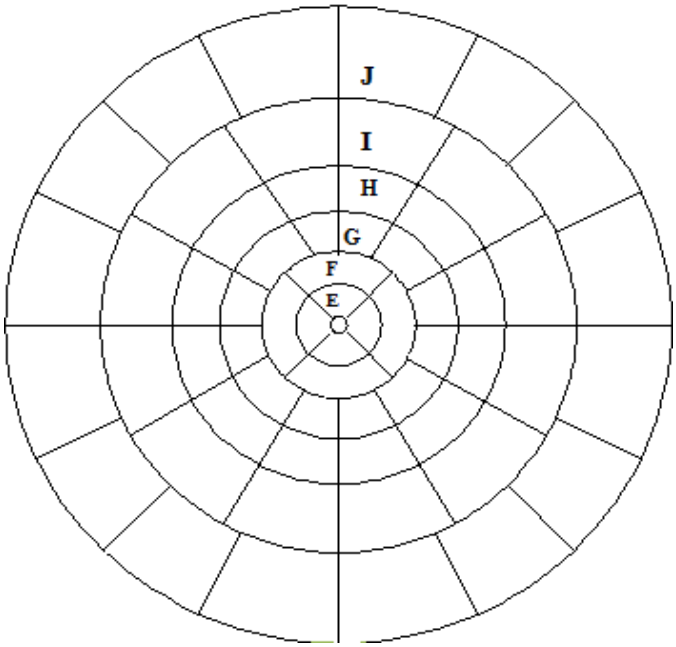

Figure 3.4. A terrain correction chart (after Hammer, 1939).

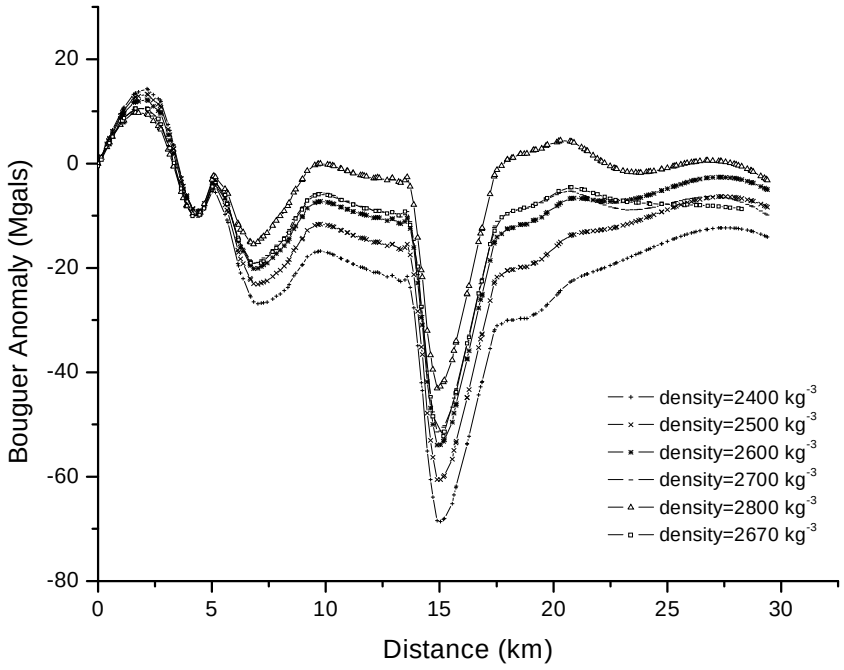

Figure 3.5 (a) Bouguer anomalies along profile B-B'.

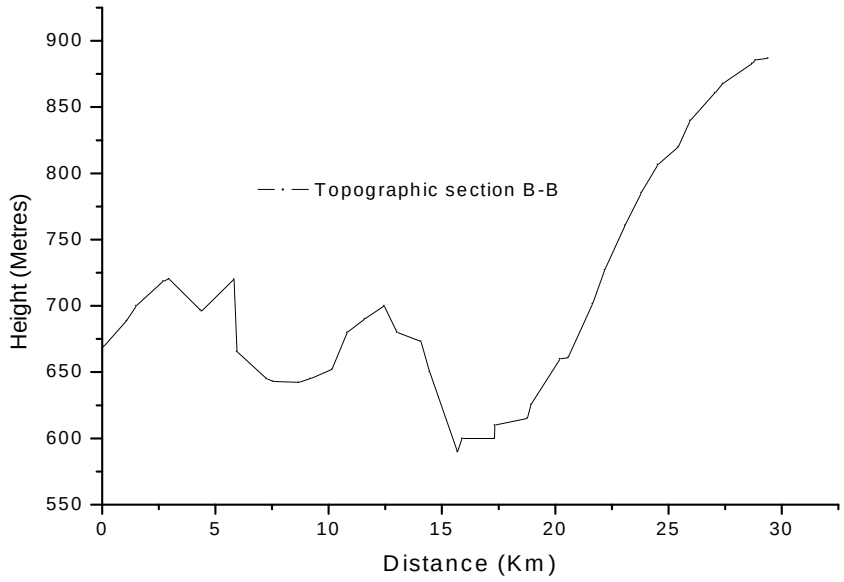

Figure 3.5(b). Cross-section of topography along profile B-B'.

3.3.2 Magnetic data reduction.

3.3.2.1. Normal Corrections.

The earth's magnetic field changes continuously in magnitude and direction as one move from one place to another. This variations cannot be correlated with geological features and have larger wavelengths compared to local anomalies of interest. Normal geomagnetic corrections were neglected in this study as the survey area was considered small relative to geological features of interest.

3.3.2.2. Diurnal Corrections.

Diurnal corrections were carried out to remove contributions due to the solar activity in the geomagnetic field. A single proton precession magnetometer was used in the survey and therefore a base station was chosen at the beginning of a day's work and reoccupied after about every two hours. A diurnal variation curve of the magnetic field against time of measurement was plotted for each survey day. Diurnal correction was effected by subtracting the magnetic reading extrapolated from diurnal curve from the field reading measured at the same time of the day.

3.3.3. Determination of Magnetic Inclination.

In eight selected stations, also the vertical component of the earth's magnetic field was measured together with the total component. The magnetic inclination at the study area was computed for the stations and displayed in Table 3.1. The average value of magnetic inclination in the study area from table 3.1 was therefore found to be 25.27° truncated to 2 decimal points.

Table 3.1. Vertical and total magnetic field with calculated inclination at selected stations.

STATION	B_T	B_Z	$B_Z/(B_T^2-B_Z^2)$	$I = \tan^{-1} (B_Z/(B_T^2-B_Z^2)^{1/2})$
B1	33490.00	14300.00	0.472204	25.27687
A21	33436.00	14275.00	0.472126	25.27321
D1	33453.00	14282.00	0.472115	25.27270
D2	33387.75	14254.26	0.472120	25.27293
D3	33370.75	14250.62	0.472311	25.28188
C2A	33390.25	14257.57	0.472211	25.27720
C7A	33345.50	14236.57	0.472134	25.27359

3.3.4 Total magnetic intensity Map

The residual total magnetic field intensity map (figure 3.6) was prepared with contour intervals of 25 nT. Solid contours were used to represent magnetic highs while hachured contours represent magnetic lows. Profiles were selected from the total intensity magnetic map passing through the discerned anomalies. A normal undisturbed geomagnetic field was approximated as 33300 nT. This is the value of magnetic field in the magnetically quiet regions in the study area as at coordinates (197, 9797) located in Lake Magadi. Also the flanks of the magnetic anomaly curves for all the profiles selected after removal of the regional field approximately approach this value asymptotically. The magnetic anomaly graphs along profiles AA', BB', CC', DD', EE' and FF' before removal of the regional field are displayed as figures 3.7, 3.8, 3.9, 3.10,

3.11 and 3.12 respectively. The magnetic field less 33300 nT was plotted against profile distance.

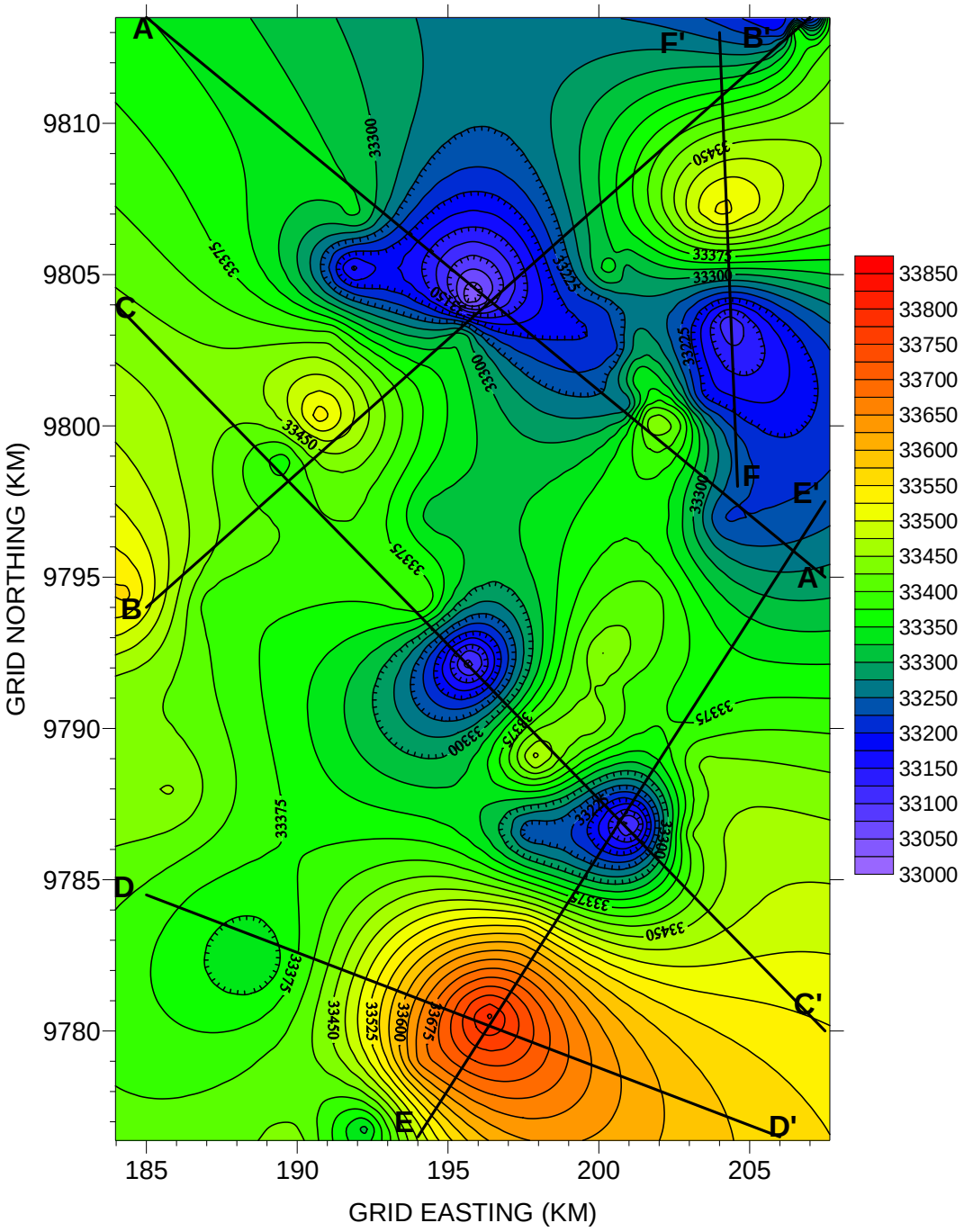

Figure 3.6 Magnetic Intensity map of contour interval 25 nT.

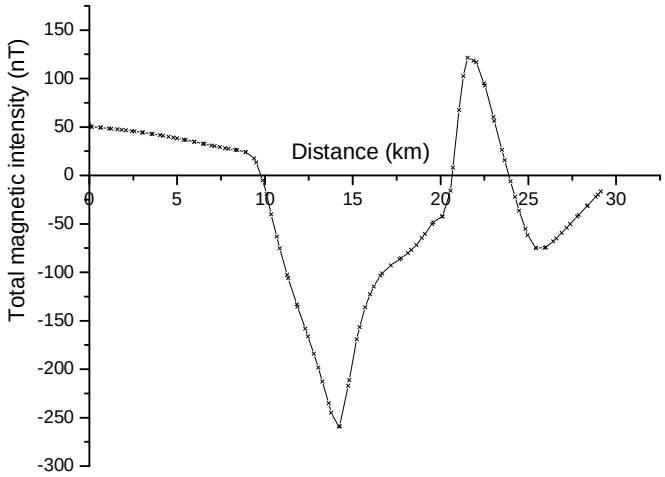

Figure 3.7 Magnetic anomaly along profile AA'.

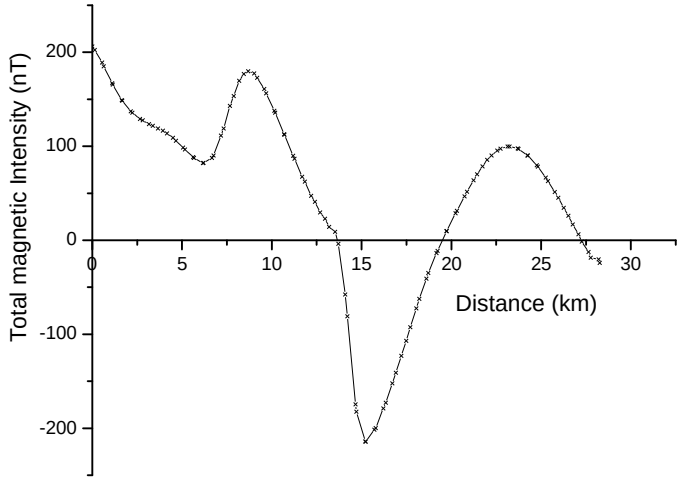

Figure 3.8 Magnetic anomaly along profile BB'.

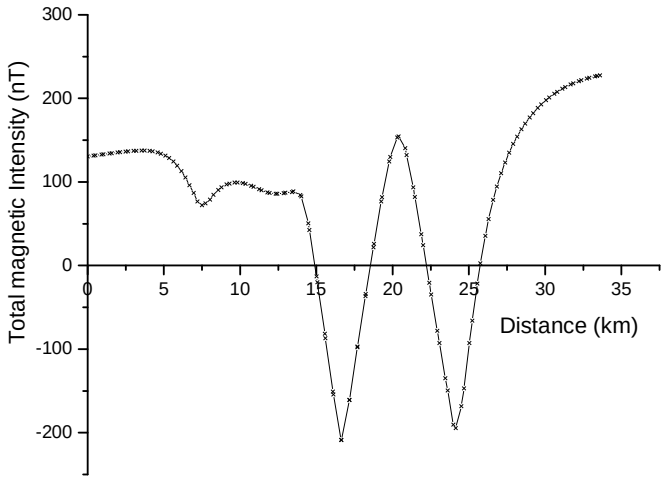

Figure 3.9 Magnetic anomaly along profile CC'.

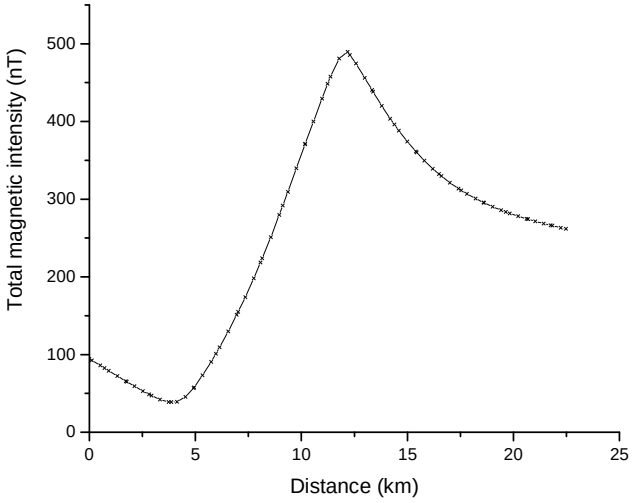

Figure 3.10 Magnetic anomaly along profile DD'.

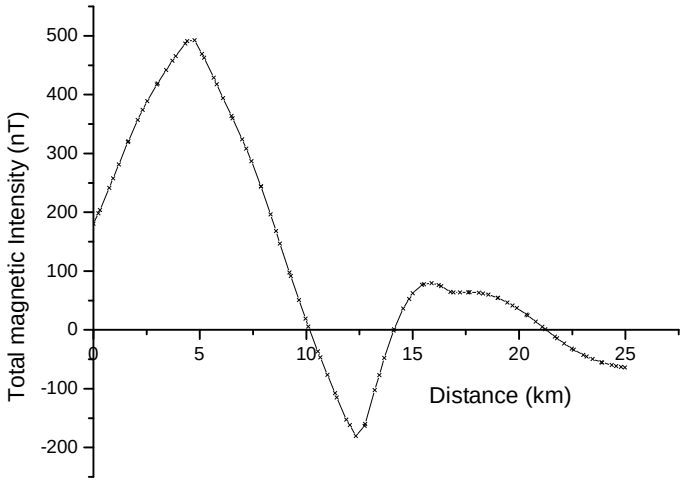

Figure 3.11 Magnetic anomaly along profile EE'.

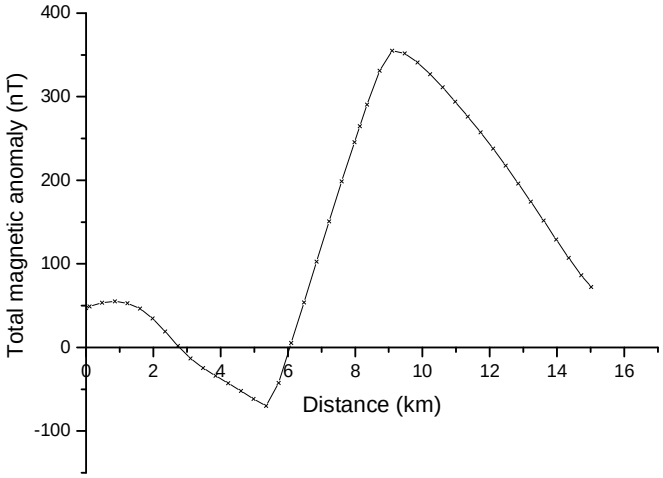

Figure 3.12 Magnetic anomaly along profile FF'.

3.3.5. Bouguer anomaly map

A Bouguer anomaly map (figure 3.13) for the study area was prepared at contour intervals of 5 mgals from the complete Bouguer anomaly data. Profiles AA', BB', CC, DD', EE' and FF' were selected along directions cutting across regions associated with the discerned anomalies on the contour map.

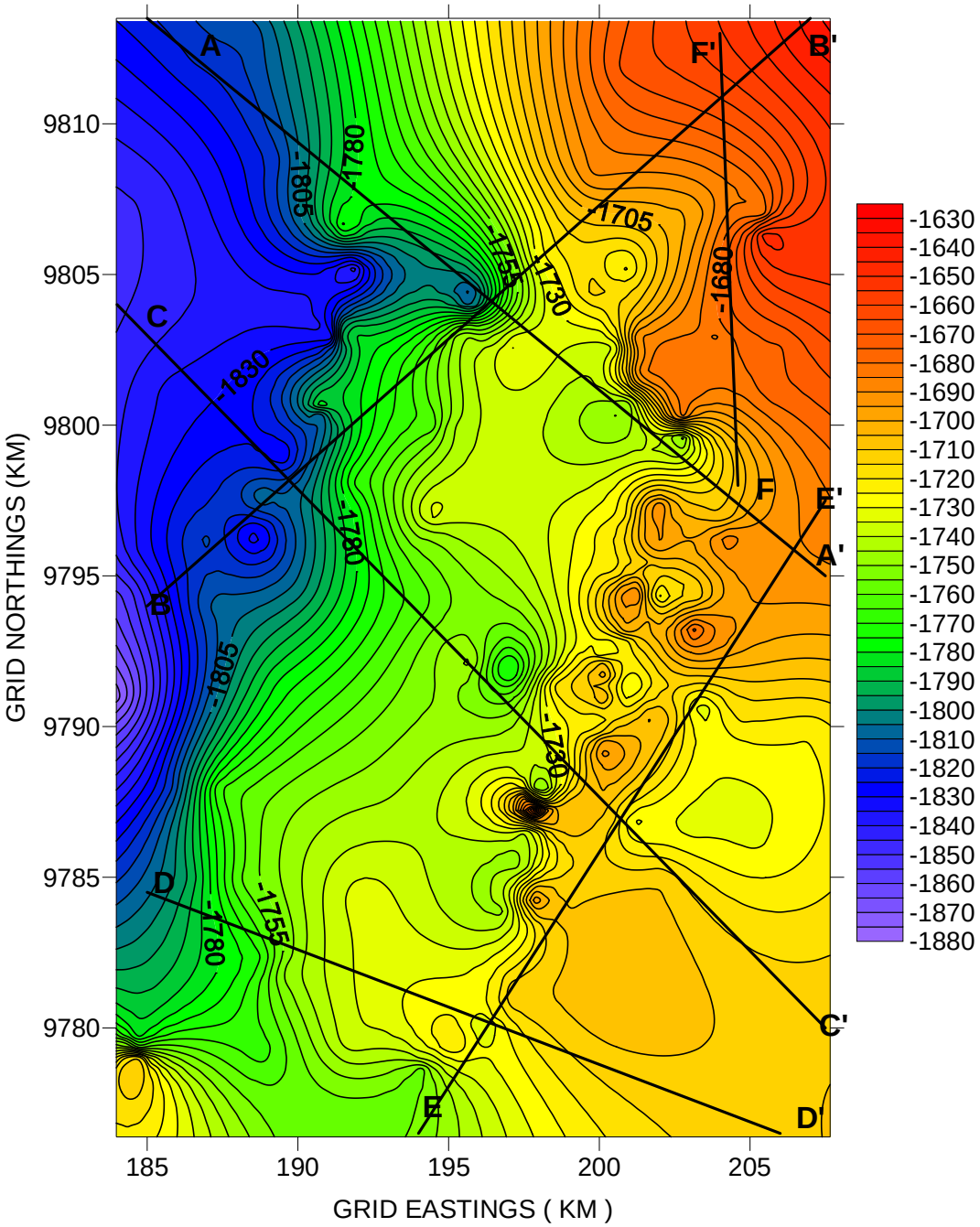

Figure 3.13 Bouguer anomaly map with contour interval of 5 mgals.

A constant of 1800 mgals was subtracted from the complete Bouguer anomaly and the result plotted against profile distance. The Bouguer anomaly graphs along profiles AA', BB', CC', DD', EE' and FF' before removal of the regional field are displayed as figures 3.14, 3.15, 3.16, 3.17, 3.18 and 3.19 respectively.

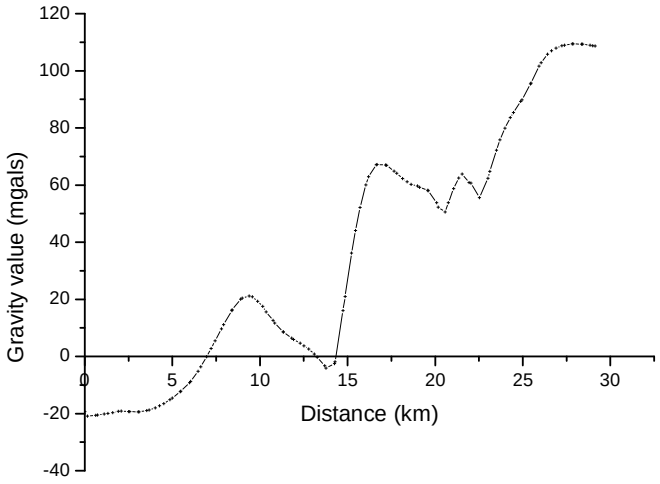

Figure 3.14 Bouguer anomaly along profile AA'.

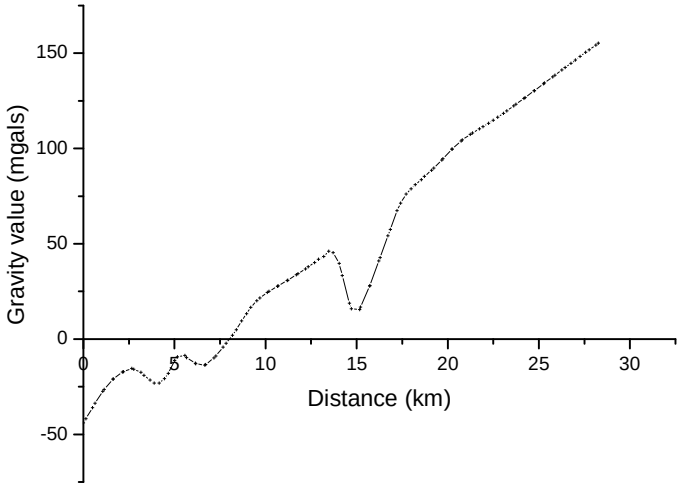

Figure 3.15 Bouguer anomaly along profile BB'.

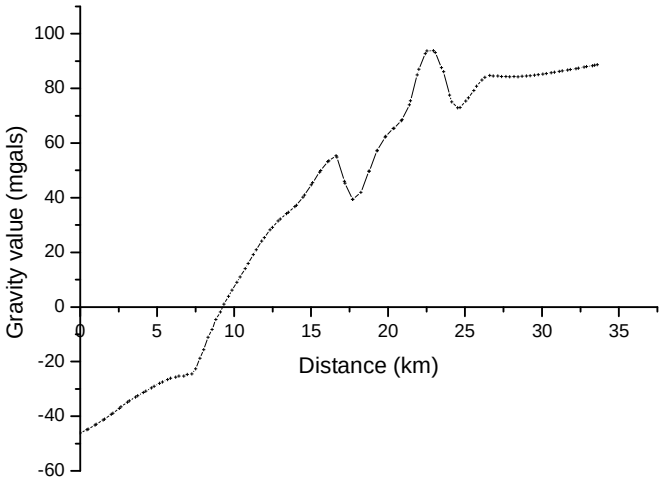

Figure 3.16 Bouguer anomaly along profile CC'.

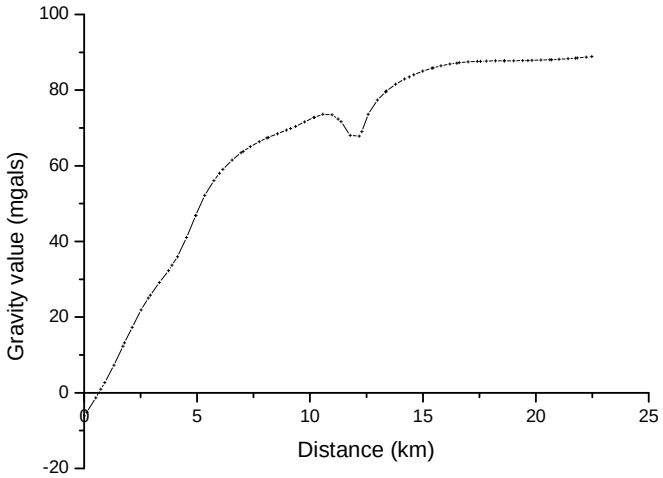

Figure 3.17 Bouguer anomaly along profile DD'.

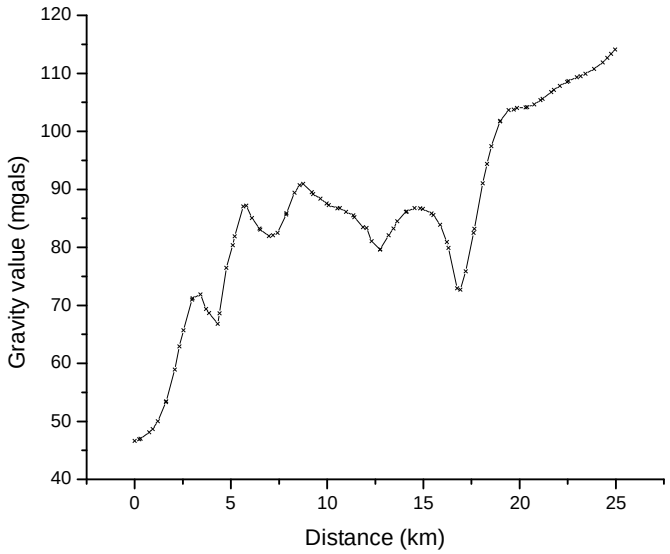

Figure 3.18 Bouguer anomaly along profile EE'.

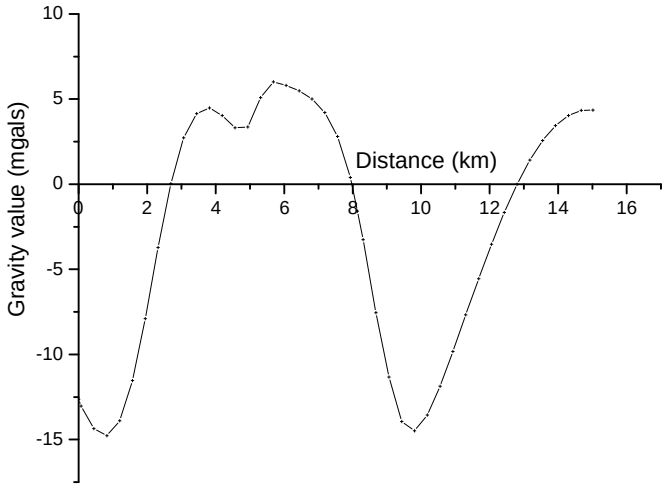

Figure 3.19 Bouguer anomaly along profile FF'.

3.3.6. Removal of regional gradient

Regional gradients caused by deep-seated structural features distort effects of shallow structures. In both the gravity and magnetic data, the regional fields have to be separated from the residual fields. The residual fields are responsible for the relatively shallow local anomalies of interest in this study, which are to be interpreted. For this reason, the regional effects have to be subtracted to isolate shallower structures of interest. The mathematical approach of isolating the residual was used whereby the regional field was fitted either as linear or a polynomial and then subtracted from the observed gravity field interpolated from the contours along a profile. The mathematical approximation of the regional field by a trend line was done using the software Grav2dc 2.10, (Cooper, pers., comm.) for the gravity profiles and Mag2dc 2.10, (Cooper, pers., comm.) for the magnetic field profiles. The regional field for gravity profiles AA', BB' and CC' were fitted as polynomials of second degree using Origin Pro 7.0 software. The listings of all the trend equations fitted to both gravity and magnetic data are given in appendix A.

CHAPTER FOUR

INTERPRETATION AND DISCUSSION

4.1. QUALITATIVE INTERPRETATION

4.1.1 Magnetic data interpretation

The total magnetic intensity map, (figure 3.6) displays several anomalies. At the southern part of the study area, a circular anomaly is present. This anomaly may be associated with granitic or basic intrusion. A profile DD' was drawn across it. Extended negative anomalies occupy regions centred at coordinates (196, 9792) and (201.5, 9786.5). The anomalies are elongated in the NW-SE directions and may represent dike structures or tectonic shear zones. A profile CC' was drawn across the anomalies. There are also extensive negative anomalies centred at (196, 9805) with a NW-SE lineation. These anomalies are located at the little lake Magadi and both profiles AA' and BB' were drawn across them. At the north-eastern region of the study area is a dipolar magnetic anomaly centred at coordinates (205, 9805) probably caused by intrusive material as it is close to Oldonyo Nyokie volcano. A profile FF' was drawn running N-S across the anomaly.

4.1.2 Gravity data interpretation

The Bouguer anomaly map (figure 3.13) is characterised by long wavelength gravity low superimposed by positive anomalies. Several closed circular anomalies cluster the south-eastern part of the study area. Most of these anomalies are aligned in the NNE-SSW direction. The anomalies have high gradient and may be shallow intrusives. A few low gradient anomalies are present in the same region also implying presence of deeper sources. From figures 3.14 to 3.19, the maximum anomaly amplitudes along the

profiles AA', BB', CC', DD', EE' and FF' are -40 mgals, -50 mgals, 50 mgals, 40 mgals, 30 mgals and 10 mgals, respectively.

4.2. QUANTITATIVE INTERPRETATION

4.2.1. Euler deconvolution technique

Euler deconvolution is a technique, which uses potential field derivatives to image subsurface depth of a magnetic or gravity source (Hsu, 2002).

Mushayandebvu et al (2001) described 2D space Euler's deconvolution equation as

$$(X - X_0)\frac{\partial T}{\partial X} + (Z - Z_0)\frac{\partial T}{\partial Z} = -N\Delta T, \quad \text{---------- (4.1)}$$

where (X_o, Z_o) is the position of the top of the source, Z is the depth measured as positive down, X is the horizontal distance, ΔT is the value of the residual field, and N is the structural index. The structural index is a measure of the rate of change or fall off rate with distance of a field and therefore it is a function of the geometry of the causative bodies. Thus, the magnetic field of a point dipole falls off as the inverse cube, giving an index of three, while a vertical line source gives an inverse square field fall off and an index of two. Extended bodies will form assemblages of dipoles and will therefore have indices ranging from zero to three.

If ΔT_i is the residual field at the i^{th} point in a magnetic or gravity survey, with the point of measurement at (X, Z) and the centre of the body at (X_0, Z_0), then equation 4.1 can be written as,

$$\begin{bmatrix} \frac{\partial}{\partial x}\Delta T_i & \frac{\partial}{\partial z}\Delta T_i \end{bmatrix} \begin{bmatrix} X - X_0 \\ Z - Z_0 \end{bmatrix} = N\Delta T_i, \quad \text{---------- (4.2)}$$

By calculating the horizontal and vertical gradients of the field, the equation 4.2 has only three unknowns X_0, Z_0 and N, where the first two describe the location of the

body. Many simultaneous equations can be obtained for various measurement locations which can give rise to one matrix equation.

$$\begin{bmatrix} \frac{\partial}{\partial x}\Delta T_1 & \frac{\partial}{\partial z}\Delta T_1 \\ \frac{\partial}{\partial x}\Delta T_2 & \frac{\partial}{\partial z}\Delta T_2 \\ - & - \end{bmatrix} \begin{bmatrix} X - X_0 \\ Z - Z_0 \end{bmatrix} = N \begin{bmatrix} \Delta T_1 \\ \Delta T_2 \\ - \end{bmatrix}, \text{ ---------- (4.3)}$$

.

The least squares method can be used to obtain the unknowns X_0 and Z_0 if the structural index N is known.

A software EULER 1.0, (Cooper, pers., comm.) for carrying out two-dimensional Euler deconvolution was used to image both the magnetic and gravity sources, where the 2D space defines depth (Z) positive down and horizontal distance (X). The input data to the software was profile magnetic and gravity field data. For the magnetic Euler solutions other than profile data, other input information included magnetic inclination, declination and the background normal total magnetic field. Magnetic declination of value 1º 56˚ was used for the study area as from topographic map sheet 160/4 printed by survey of Kenya. By qualitative interpretation of the magnetic contour map's quiet areas, a normal total field was approximated as 33300 nT. The magnetic inclination of -25.27º as determined from field measurements displayed in Table 3.1 was used. The source distribution is assumed to be two-dimensional such that the first derivatives of T that is $\frac{\partial T}{\partial X}$ and $\frac{\partial T}{\partial Z}$ at all the above locations are calculated by the software. When magnetic or gravity data in a profile is run in EULER 1.0 software, (Cooper, pers., comm.), the profile is divided into windows of set of data points ranging from 7 to 19. A source location (X_0, Z_0) is calculated for each set of points using equation and least-

squares methods. Source locations were plotted in cross-section, which clustered around magnetised sources.

4.2.1.1. Choice of structural index (S.I)

Real data set is likely to contain anomalies from various geological features with varied structural indices. Therefore depth solutions for different structural indices (0.5, 1.0, 1.5, 2.0. 2.5 and 3.0) were obtained for each profile. The solution maps were examined and the index that gave the best cluster was chosen for the feature. This procedure also gave an idea about the nature of the causative feature. The solutions generated for single data sets showed that imaged depth increased with increasing assumed structural index. According to Reid *et al* (1990), the structural index for faults varies between zero (for large throws) and one (for small throws). Therefore an average structural index of 0.5 was optimum in imaging fault and contacts. Table 4.1 illustrates the structural indices of corresponding geological features after Reid *et al* (1990).

Table 4.1. Structural indices for different geological structures

Structural Index	Magnetic Field	Gravity Field
0	Contact	Sill / Dike / Step
0.5	Thick Step	Ribbon
1	Sill / Dike	Vertical Pipe
2	Vertical Pipe	Sphere
3	Sphere	

4.2.1.2. Boundary Analysis by horizontal gradients

The steepest horizontal gradient of a gravity anomaly or a pseudo gravity anomaly caused by tabular body tends to overlie the edges of the body. The steepest gradient is

located over the edge of the body if the edge is vertical and far removed from all other edges or sources. This characteristic of gravity anomalies is useful in locating abrupt lateral changes in density from gravity measurements (Cordel, 1979). This can also be applied to magnetic measurements by first transforming them into pseudo gravity anomalies, in which the steepest horizontal gradient would reflect abrupt lateral changes in magnetisation (Cordel and Grauch, 1985).

The horizontal gradient is given by equation 4.3.

$$h(x,y)=\left[\left(\frac{\partial g_z(x,y)}{\partial x}\right)^2+\left(\frac{\partial g_z(x,y)}{\partial y}\right)^2\right]^{\frac{1}{2}} \qquad \text{---------- (4.3)}$$

When applied to two-dimensional surveys, the horizontal gradient tends to place narrow ridges over abrupt changes in magnetisation or density. Location of maxima in horizontal gradient can be done by simple inspection. The assumption in this procedure is that the contrast in physical properties such as magnetisation and density occur across vertical and abrupt boundaries isolated from other sources.

4.2.1.3. Reduction to the pole

Positive gravity anomalies tend to be located over mass concentration but the same is not necessarily true for magnetic anomalies when the magnetisation and ambient field are not both directed vertically. In reduction to the pole procedure, the measured total field anomaly is transformed into the vertical component of the field caused by the same source distribution magnetised in the vertical direction. The acquired anomaly is therefore the one that would be measured at the north magnetic pole, where induced magnetisation and ambient field both are directed downwards (Blakely, 1995).

The software Euler was used in reducing to the pole magnetic profile data. This was important for outlining magnetic units and positioning magnetic discontinuities, which may correspond to faults. Reduction to the pole is usually unreliable at low magnetic latitudes, where northerly striking magnetic features have little magnetic expression. Some bodies have no detectable magnetic anomaly at zero inclination. The validity of the reduction to the pole is doubtful for inclinations lower than approximately 15º. The average inclination in the survey area was -25.27º and is located at average magnetic latitude of 10.47º and therefore reduction to the pole may be considered reliable.

4.2.1.4. Discussion of Euler deconvolution results.

From magnetic profile AA' in Figure 4.1 calculated solutions map the depth to the subsurface structure. A structural index of 1.0 was used which best represents sill edge, dike, or fault with limited throw. The horizontal and vertical gradients highly fluctuate over a distance of 14 km to 22 km along the profile. This may represent abrupt lateral change in magnetisation over the distance range. The depth to the magnetic structure is shallowest from 14-22 km at a depth of approximately 0.8 km from the surface. The deepest part of the profile was 8 km. The shoulders of the Reduction to the pole (RTP) outlines the edges of a possible thick dyke located at profile distance 15-21 km. From gravity profile AA' in Figure 4.2, the gravity anomalies in the profile is superimposed and may represent multiple features. A structural index of 0.5 was used which best represents dike structures. Maximum depth imaged along the profile is approximately 2 km while the shallowest is almost to the surface. Most solution cluster is at a profile distance ranging 14 km to 21 km. From 17 km to 26 km, the gravity anomaly displays a gravity low with a high superimposed at about 21.5 km. This may represent high-

density material impregnated in relatively low-density material. This structure may be the same feature observed at the same position in the magnetic profile.

From magnetic profile BB' in Figure 4.3 solution cluster is observed at 11 km, 14 km, 17 km and 25 km. There is an abrupt change in both horizontal and vertical gradients between 14-16 km profile distances and also at the same location; the shallowest depth of approximately 0.5 km is attained along the profile. The shoulders of the RTP curve outlines the probable edges to causative structures at profile distances 7 km, 14 km, 17 km and 26 km. From gravity profile BB' in Figure 4.4, it is a gravity low superimposed by a high at a profile distance of 5 km.

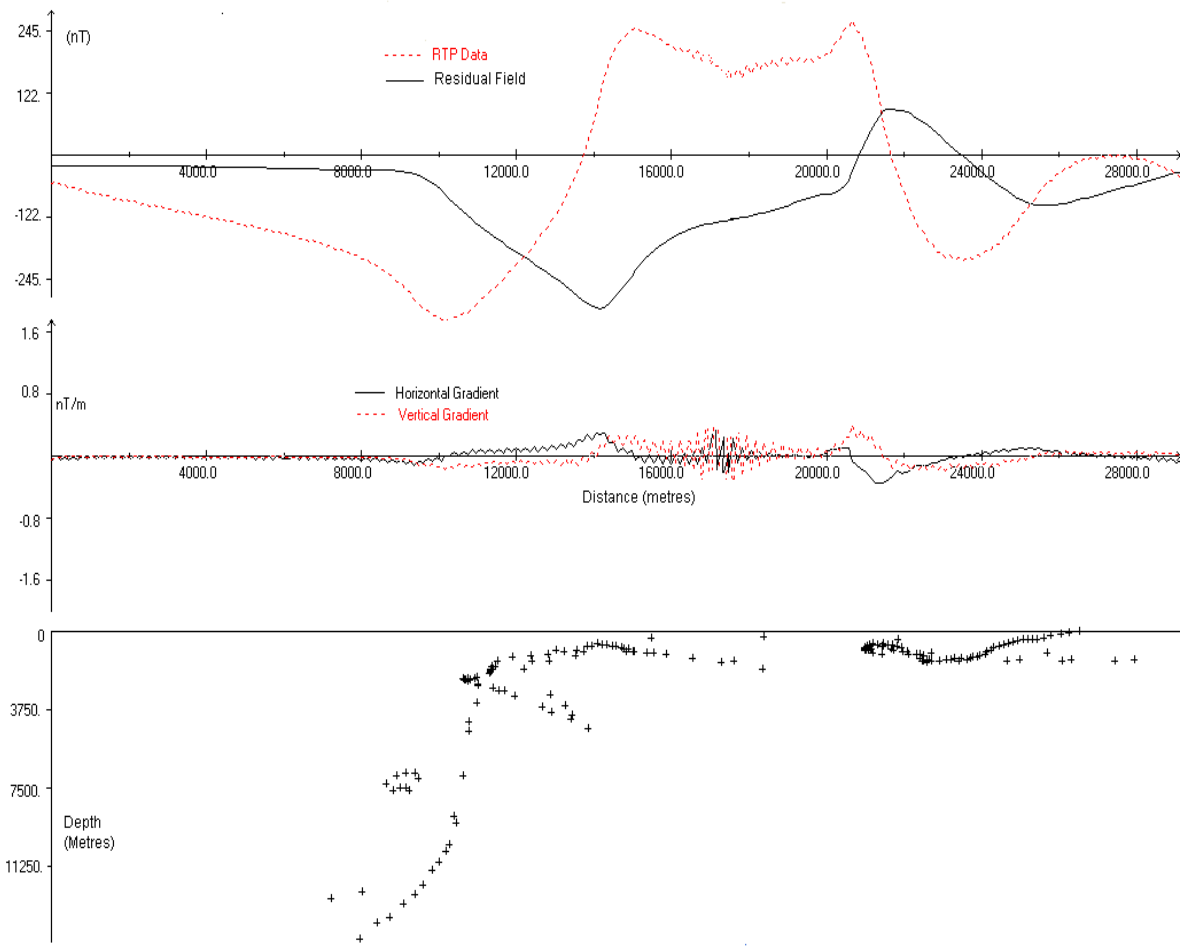

Figure 4.1 Euler depth solutions along magnetic anomaly profile A-A'.

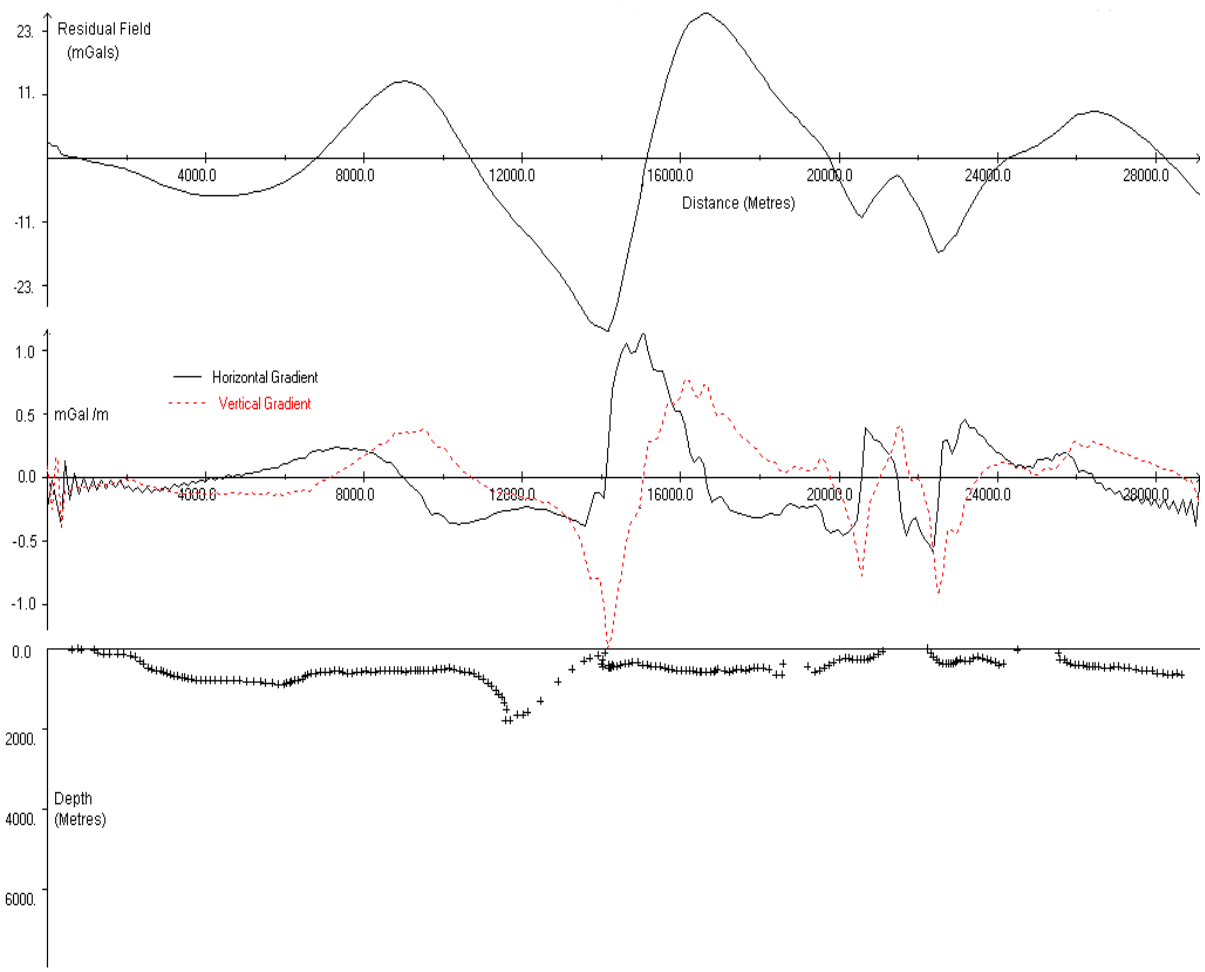

Figure 4.2. Euler depth solutions along gravity anomaly profile A-A'

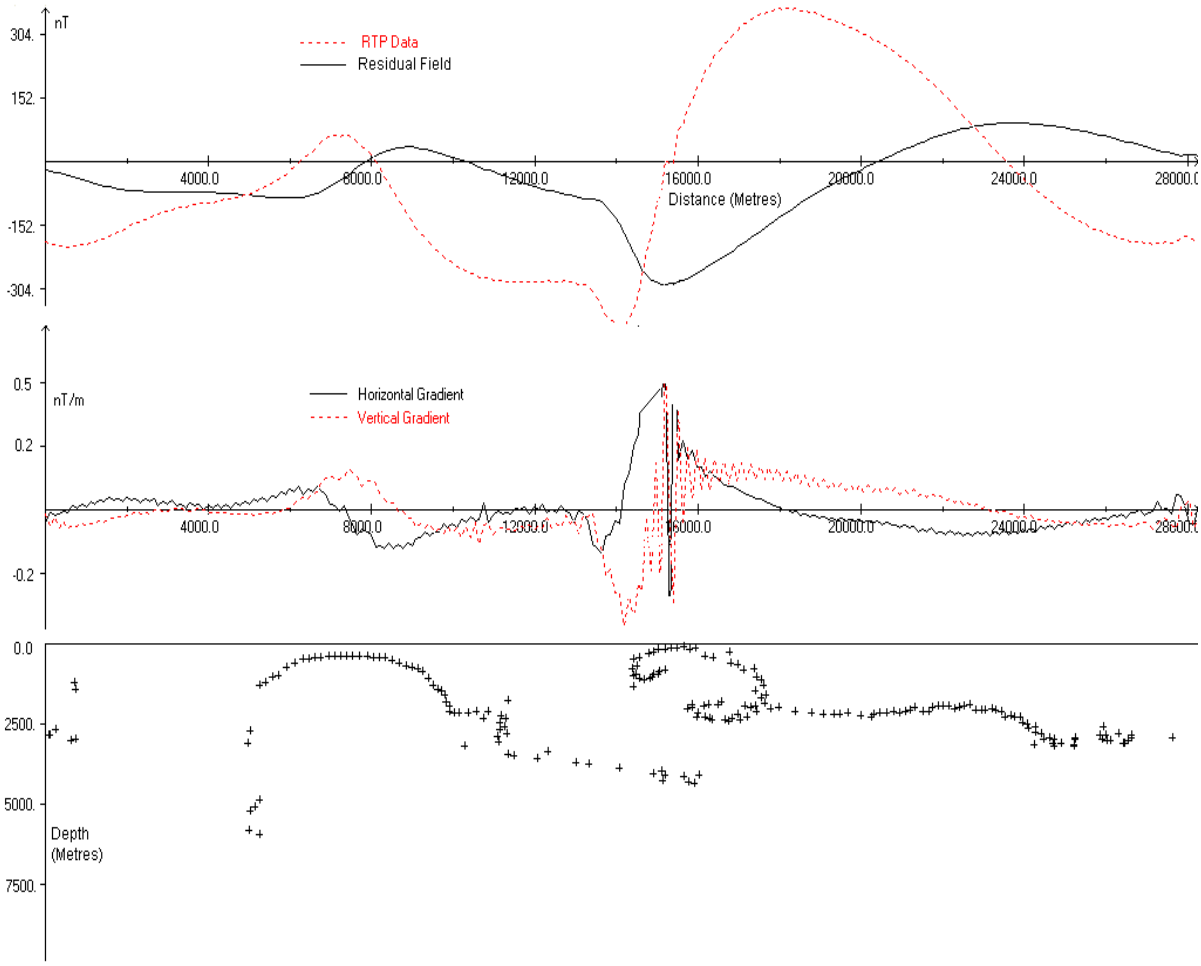

Figure 4.3 Euler depth solutions along magnetic anomaly profile B-B'

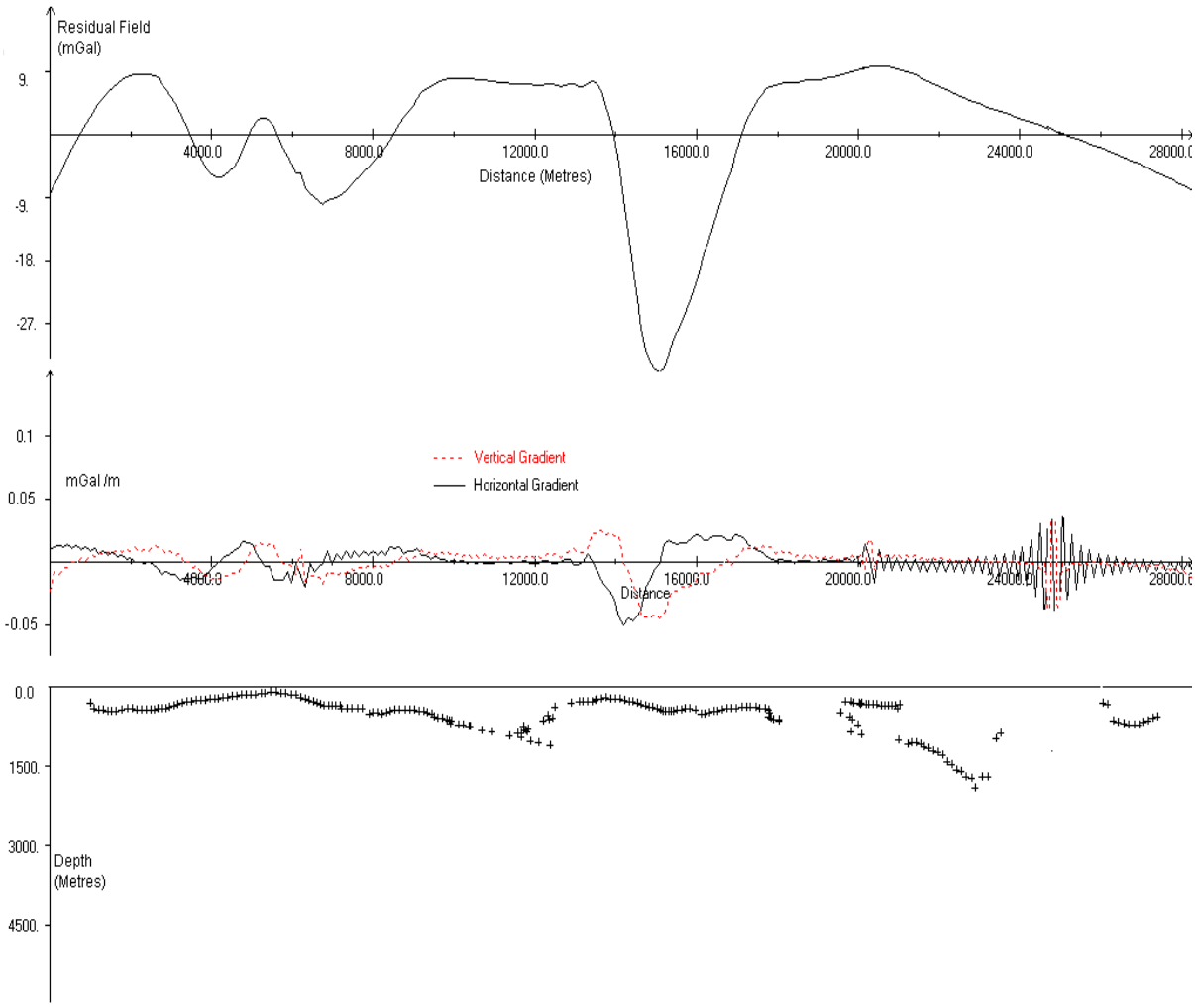

Figure 4.4 Euler depth solutions along gravity anomaly profile B-B'

The most conspicuous lows are at profile distances 7 km and 15 km with corresponding imaged depths of approximately 0.5 km and 0.7 km respectively. The lows also coincide with solution cluster. Major discontinuities are observed from 8-20 km and from 24-26 km. Abrupt change in both horizontal and vertical gradients was observed from 4-5 km, 5-7 km, 14-15 km, 17-18 km and 24-25 km which most probably represents lateral change in magnetisation. Depths to the gravity structure displayed are rather shallow ranging from 0.2-1.5 km.

From magnetic profile CC' in Figure 4.5, a structural index of 1.0 was used and solutions found reflected major discontinuities from 6 km, 9 km, 16 km and 21 km. These may represent faulted structures. There are also abrupt changes in both horizontal and vertical gradients at 17.5 km. The gravity profile CC' in Figure 4.6 is a gravity high superimposed by local lows at 7.5 km, 18 km and 25 km. The imaged depth solutions also indicated several discontinuities at horizontal profile distances 5-7 km, 14-15 km, 18-20 km and 22.5 km. Maximum depth imaged is approximately 1.5 km with the shallowest being close to the surface. Abrupt change in horizontal and vertical gradients occurs between 18 km and 20 km, which may represent lateral change in magnetisation.

The Euler solutions along magnetic profile DD' in Figure 4.7 maps the magnetic structure with the shallowest depth of 0.9 km and deepest at 4.2 km. The horizontal and vertical gradients fluctuate at a profile horizontal distance of 4km and 12 km. This position also coincides with the inflection point of the corresponding R.T.P curve.

This may represent position of top of a magnetic body.

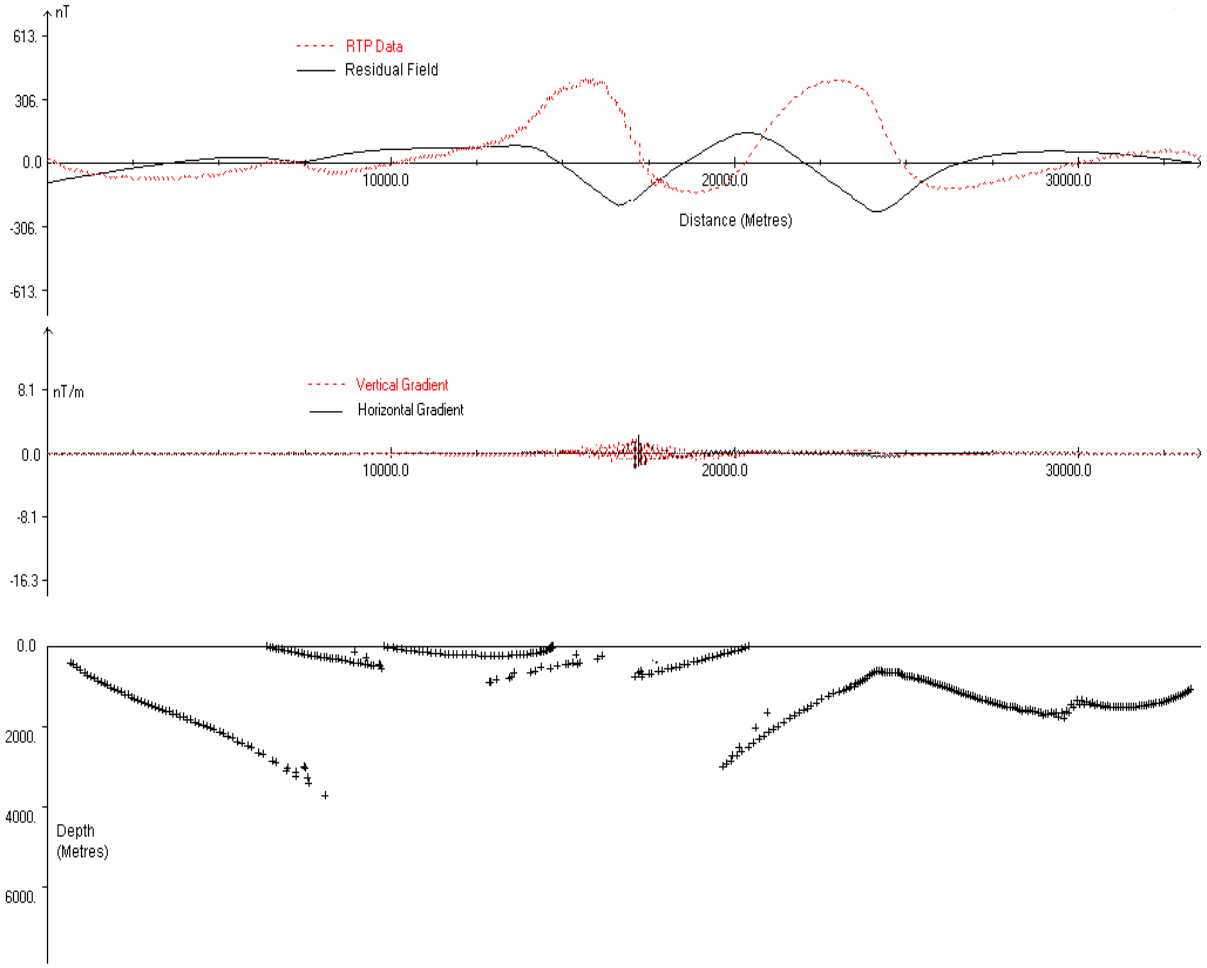

Figure 4.5 Euler depth solutions along magnetic anomaly profile C-C’

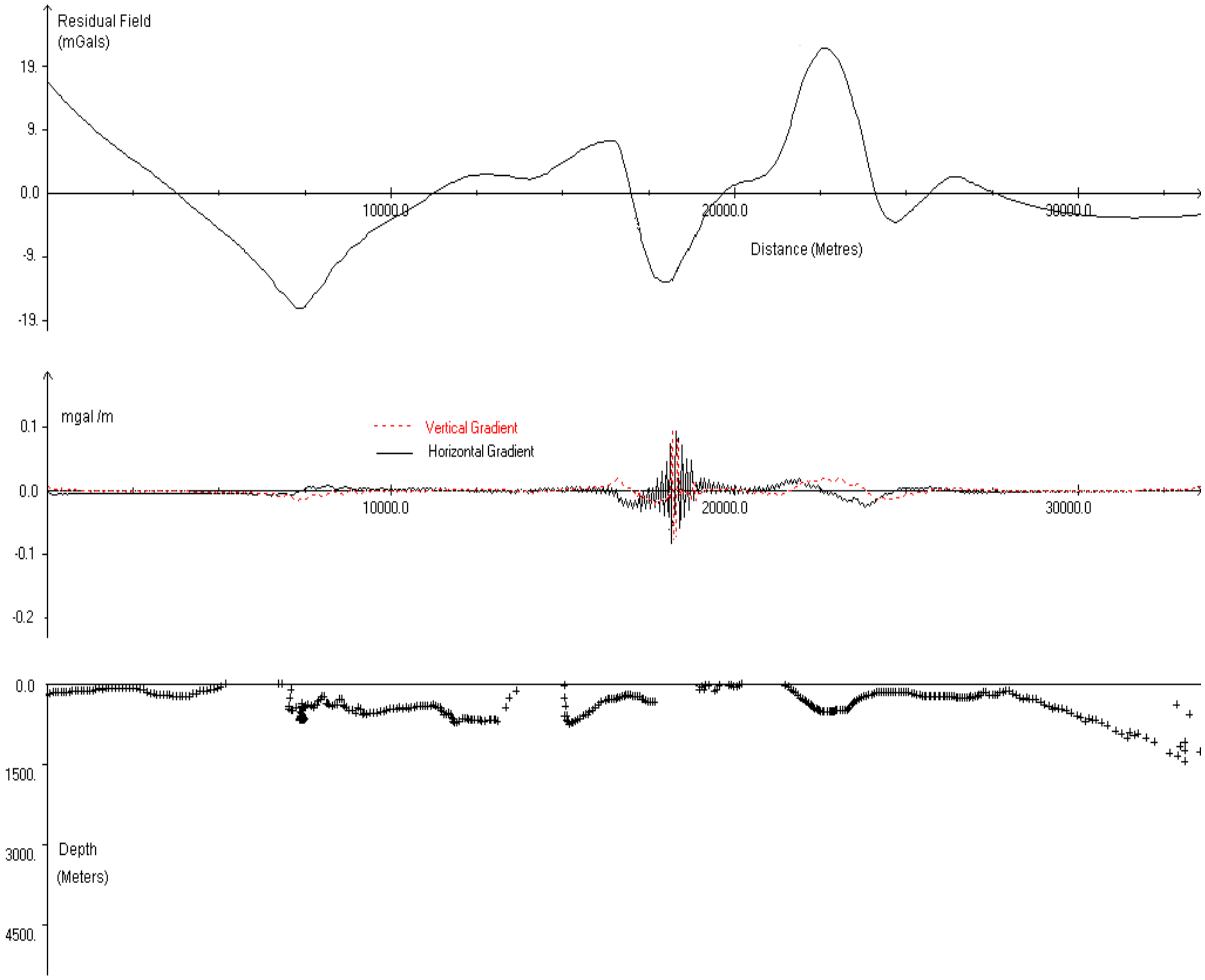

Figure 4.6 Euler depth solutions along gravity anomaly profile C-C'.

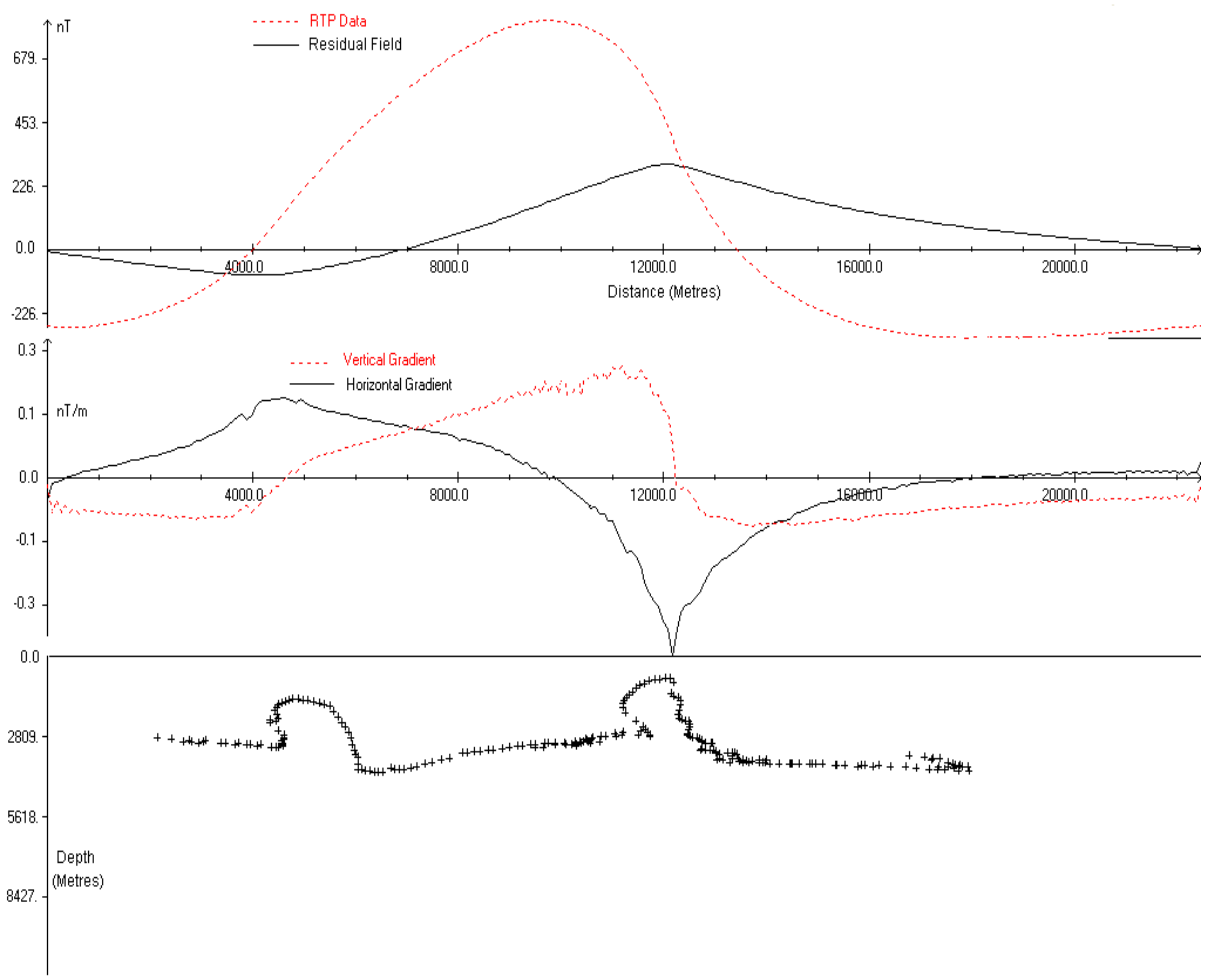

Figure 4.7 .Euler depth solutions along magnetic anomaly profile D-D'.

The gravity profile DD' in Figure 4.8 is a long wavelength gravity high superimposed by local gravity lows at horizontal profile distances of 4 km and 12 km respectively. The Euler solutions indicate a discontinuity at a horizontal profile distance of 6-9 km, which may be indicative of faulted structure. The Euler solutions along magnetic profile EE' in Figure 4.9 has the shallowest depth of 0.2 km and the deepest is 2 km. The R.T.P curve display a magnetic low at 7 km and a magnetic high at 13 km, which may represent rocks of low and high magnetic susceptibility relative to the host rocks. Fluctuations of magnetic gradients are evident at 8 km, 13 km and 19 km possibly indicating changes in magnetization. Gravity profile EE' in Figure 4.10 displays a long wavelength gravity high with fluctuating lows. Sharp changes in gradients are observed at 4 km, 8 km, 12 km and 16 km. The deepest depth imaged is 1.5 km and the shallowest close to the surface.

The Euler magnetic analysis along profile FF' in Figure 4.11 reveals a shallow magnetic structure to a maximum depth of 1.7 km at a point of inflection of the magnetic anomaly curve. This is at a horizontal profile distance of 7 km. R.T.P curve has a maxima close to this point indicating the effect of the body at this point. There is a sudden change in the horizontal magnetic gradients at profile distances of 3 km, 4.5 km, 5.5 km and 9 km which may be points defining edges of the body where magnetisation changes. The gravity profile FF' in Figure 4.12 has a positive anomaly with an amplitude of about 10 mgals and a negative anomaly at 4 km and 10 km horizontal profile distances respectively. The horizontal gradients indicate sudden fluctuations at profile distances of 3 km, 4.5 km, 5.5 km, 8 km and 9.5 km. These fluctuations are observed at same positions as in the corresponding magnetic curve, an

indication that the density contrast in the structure coincide with changes in magnetisation. Discontinuities are also observed at a profile distance of 3-4 km.

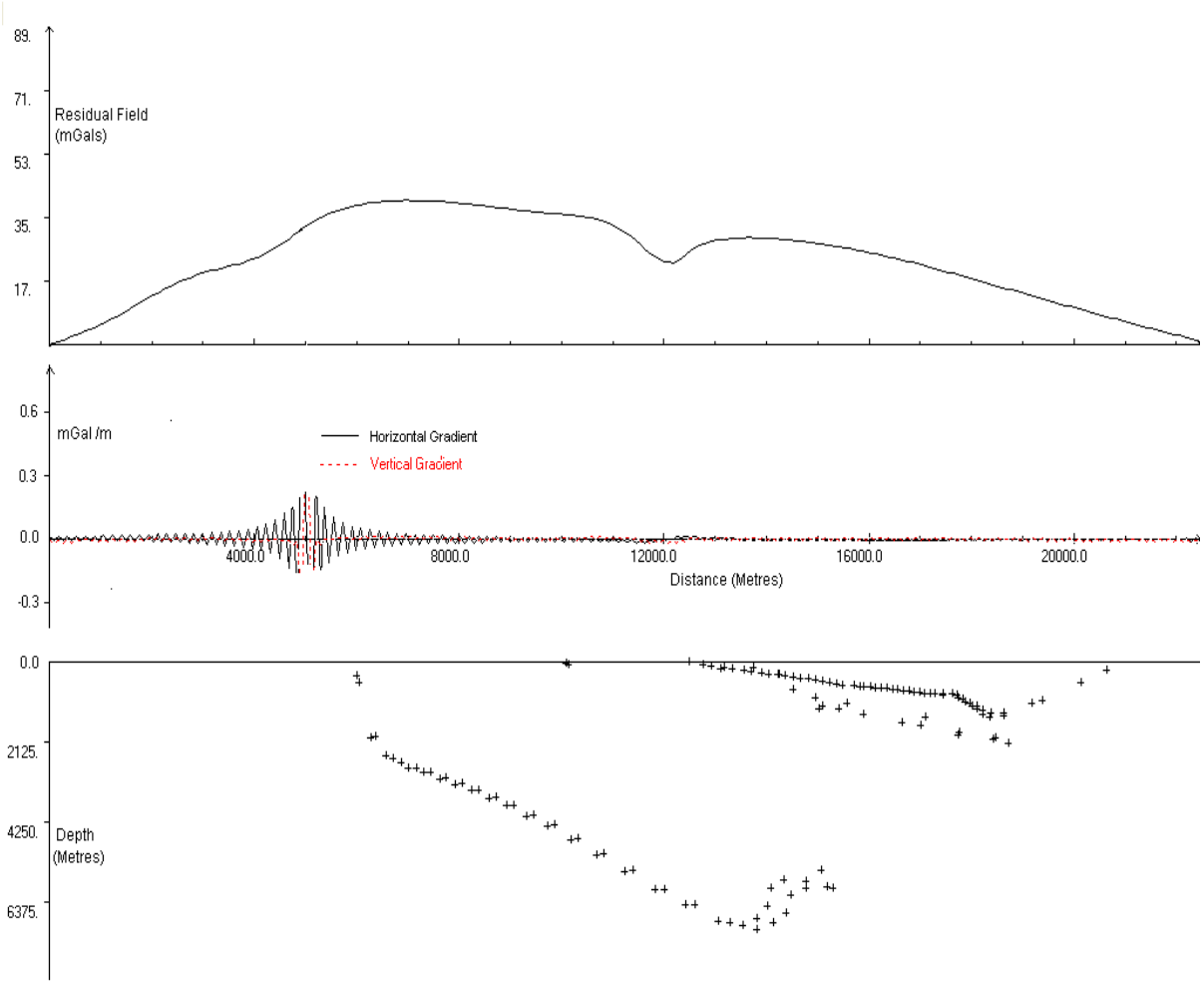

Figure 4.8 Euler depth solutions along gravity anomaly profile D-D'.

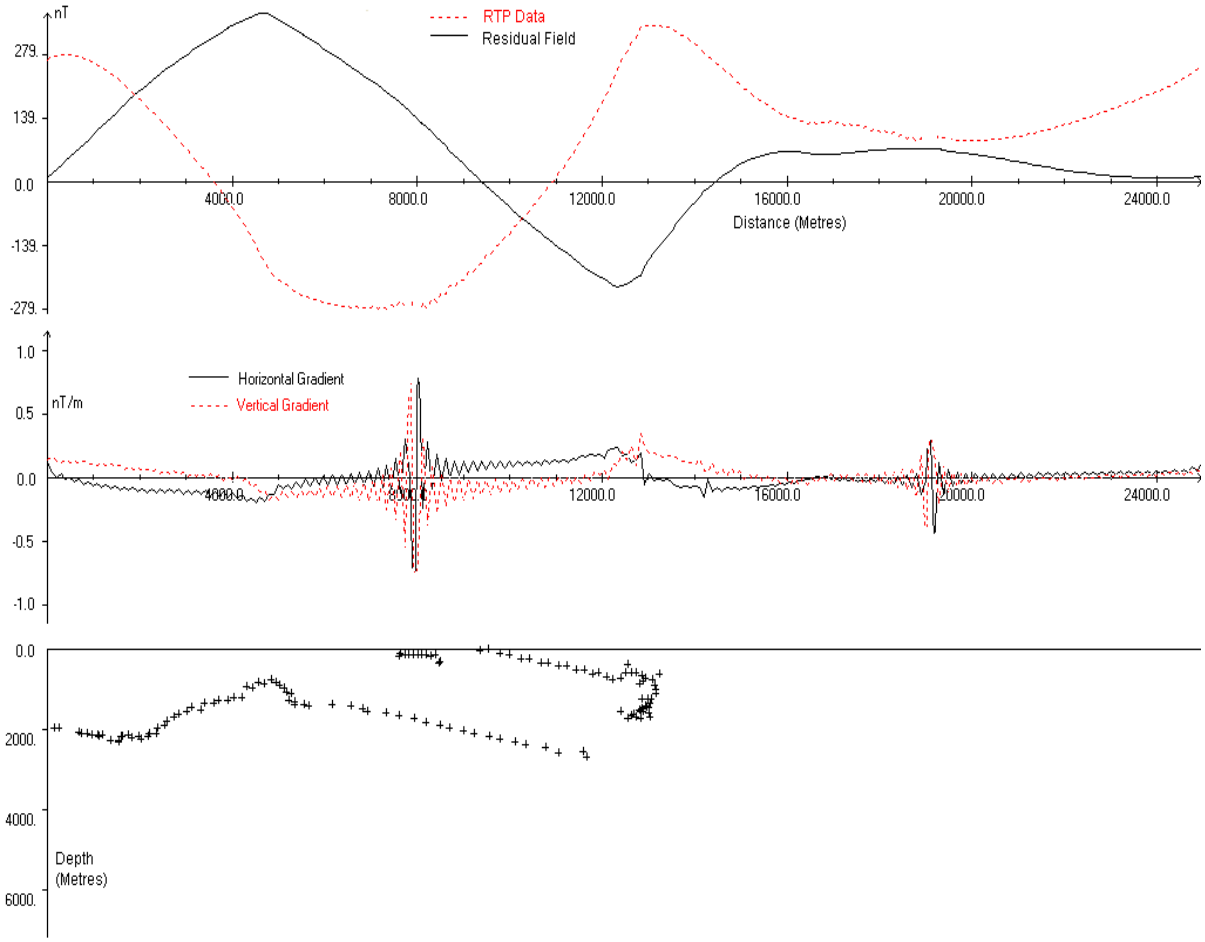

Figure 4.9.Euler depth solutions along magnetic anomaly profile E-E'.

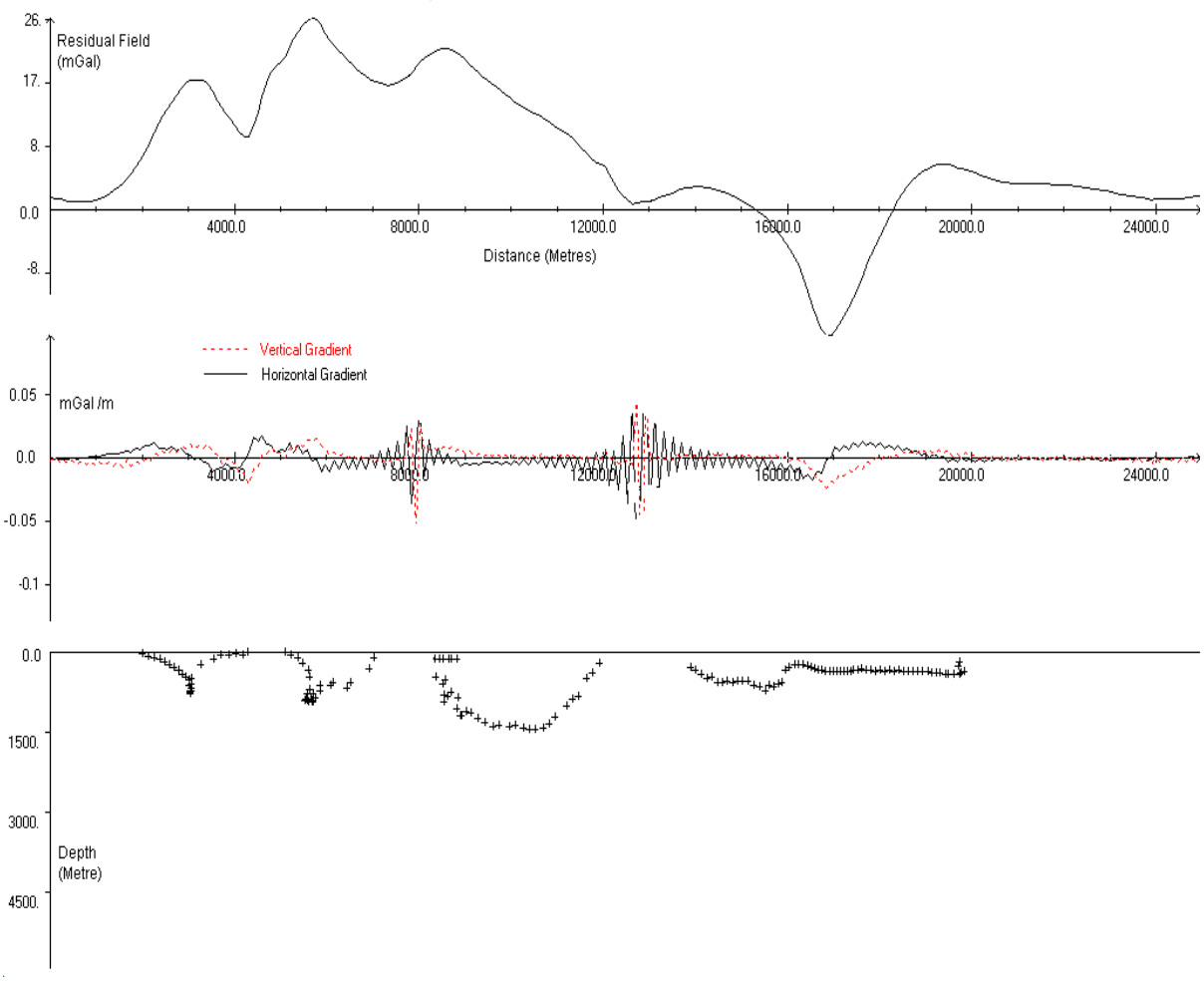

Figure 4.10 Euler depth solutions along gravity anomaly profile E-E'.

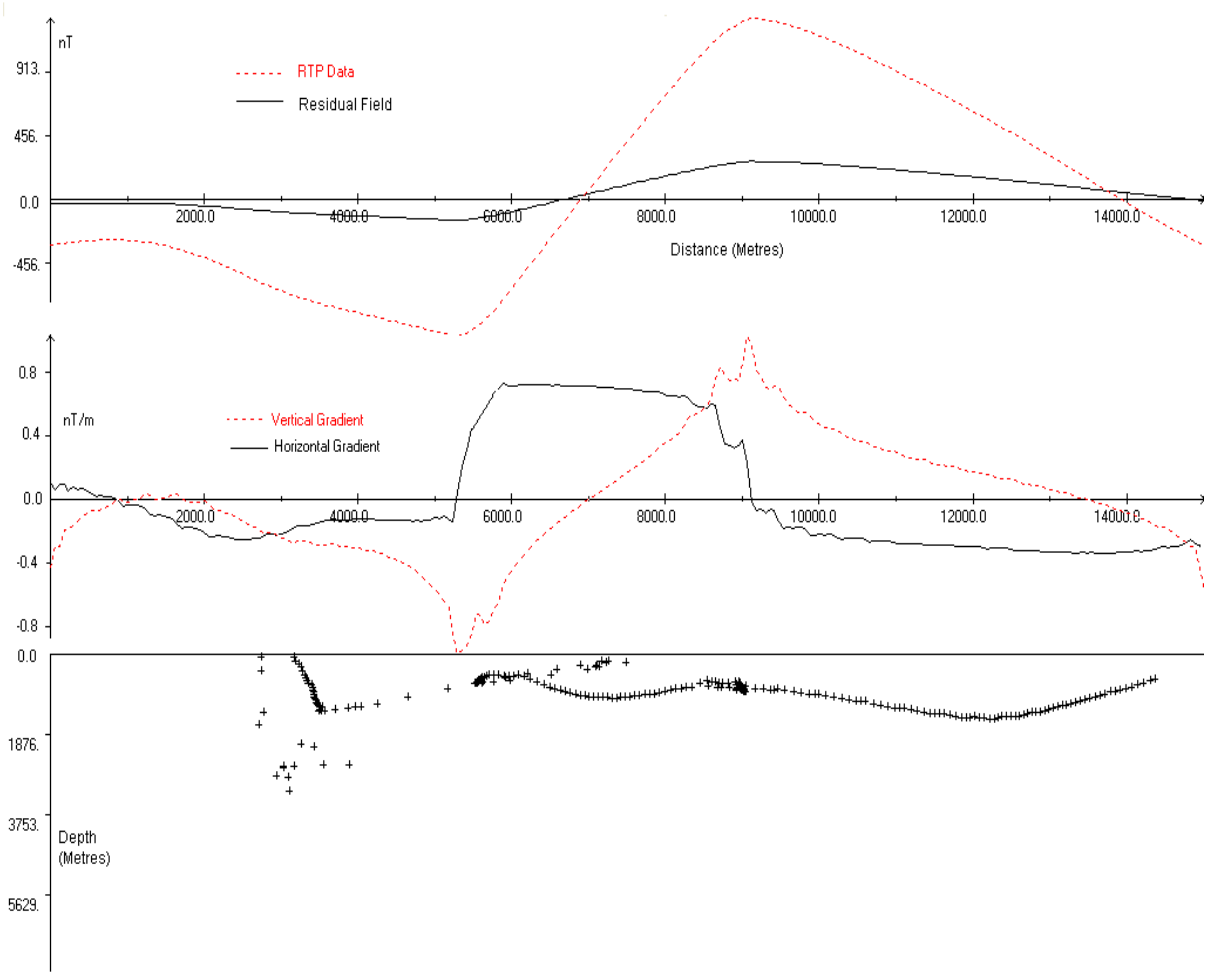

Figure 4.11. Euler depth solutions along magnetic anomaly profile F-F'.

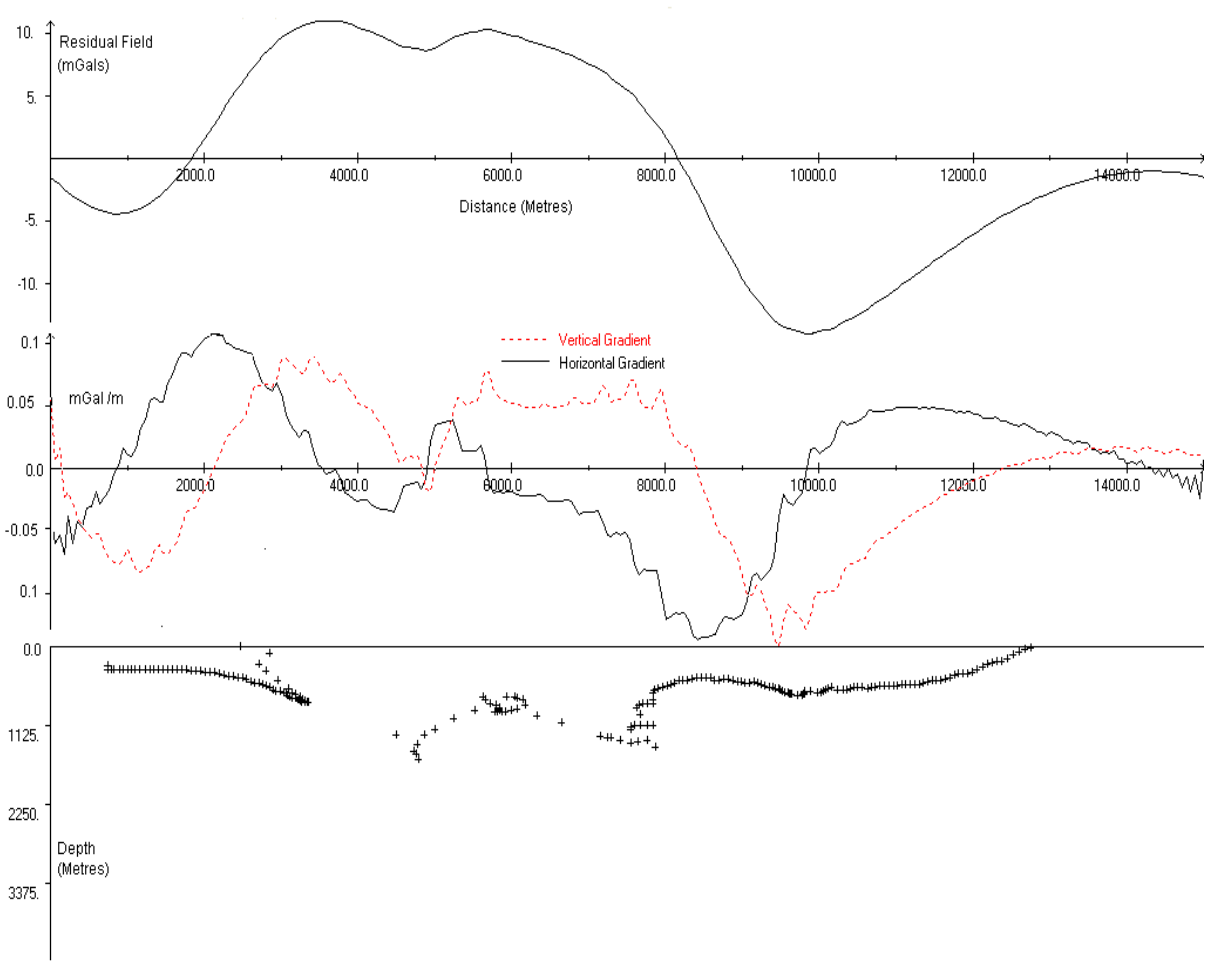

Figure 4.12 Euler depth solutions along gravity anomaly profile F-F'.

4.2.1.5 Merits and demerits of Euler deconvolution.

The main advantage of using this technique is that it provided a fast method for imaging approximate depths to subsurface bodies. The identified locations and depths to the causative sources are independent of magnetization directions or distortion of field caused by remanent magnetism. The form of the feature was also inferred from the optimum structural index applied. The approximate source depth locations acquired were used later for start models in generating forward models.

The use of Euler deconvolution in interpretation of potential fields for source depths and location developed by Reid *et al*. (1990) is limited due to uncertainty of depth estimates generated and also absence of susceptibility, density contrast and dip estimates. The convectional Euler deconvolution applied in this study also suffers limitation such that the structural index is subjectively chosen before generation of results depending on the structures expected in the study area. Application of incorrect structural index may therefore yield scattered solutions and biased depth estimates. The appropriate index was done by generating solutions using different indices. The index that gave the best solution clustering was chosen. Reid *et al.* (1990) suggests that for the structural indices 0.0, 0.5 and 1.0 the acceptance level to imaged depths are 25%, 18% and 15% respectively.

4.2.2. Spectral Analysis

4.2.2.1. Introduction

Magnetic fields reflect distribution of magnetisation in the internal structure of the earth. This field results from superposition of large number of sources of variable sizes and can appear similar over many spatial scales. There exists a relationship between wave number and depth (Spector and Grant, 1970; Nnange, *et.al.*, 2000) that can be used to separate regional field from residual field.

Mathematically the Fourier transform of a space domain function f (x,y) is defined in equation 4.3 whereas the inverse relation is shown in equation 4.4

$$\bar{f}(\mu,\nu) = \int_{-\infty}^{\infty}\int_{-\infty}^{\infty} f(x,y).e^{i(\mu x+\nu y)}dxdy \quad \text{---------- (4.3)}$$

$$f(x,y) = \frac{1}{4\pi^2}\int_{-\infty}^{\infty}\int_{-\infty}^{\infty} \bar{f}(\mu,\nu).e^{i(\mu x+\nu y)}d\mu d\nu \quad \text{---------- (4.4)}$$

Where μ and υ are wave numbers in the x and y directions respectively, measured in radians per meter if x and y are in metres. These are related to spatial frequencies, which are measured in cycles per meter. A grid in space domain is transformed to wave number domain by use of a Fast Fourier Transform (FFT). Just as a grid samples a space domain function at even distance increments, a transform samples the Fourier domain function at even increments of 1/(grid size) in cycles per meter between 0 and the Nyquist wave number. The Nyquist frequency is given by the equation 4.5.

$$N = \frac{1}{2\Delta X} \quad \text{---------- (4.5)}$$

Where ΔX is the sample interval. This is the highest frequency that is possible to measure given a fixed sample interval (Billings and Richards, 2000). A given potential field function in the space domain has a single and unique wave number domain

function. The addition of two functions (anomalies) in the space domain is equivalent to the addition of their transforms.

A Fourier transform F (k) in one dimension consists of a complex function with real and imaginary parts which can be expressed as

$$F(k) = |F(k)|e^{i\Theta(k)} = \mathrm{Re}\,F(k) + i\,\mathrm{Im}\,F(k) \quad \text{,---------- (4.6)}$$

where $|F(k)| = \left[(\mathrm{Re}\,F(k))^2 + (\mathrm{Im}\,F(k))^2\right]^{\frac{1}{2}}$ and $\Theta(k) = \tan^{-1}\left[\dfrac{\mathrm{Im}\,F(k)}{\mathrm{Re}\,F(k)}\right]$,

$|F(k)|$ and $\Theta(k)$ are the energy and phase spectrum respectively. The total energy of f (x) is given by

$$E = \int_{-\infty}^{\infty} |F(k)|^2\, dx. \quad \text{---------- (4.7)}$$

The energy density spectrum is expressed as $|F(k)|^2$

4.2.2.2 Estimation of Curie-Point Depth by spectral analysis

The Curie point depth is the depth at which the dominant magnetic mineral in the crust passes from a ferromagnetic state to paramagnetic state under the effect of increase in temperature (Nagata, 1961). Spector and Grant (1970), by analysing statistical patterns of magnetic anomalies, have proven a relationship between the spectrum of observed anomalies and depth of a magnetic source by transforming the spatial data into frequency domain as shown in equation F.12 of appendix F. According to Okubo *et. al* (1985), the basal depth of a magnetic source was considered to be the Curie point depth. In this study, Fast Fourier Transform (FFT) was applied to reduced to the pole

(RTP) magnetic profile data that had earlier been acquired using Euler software. The pole-reduced data software was sampled at an equal spacing of 0.125 Km.

The forward FFT was done using Origin Pro software version 7. The input data consisted of two columns that is the profile distance sampled at a spacing of 0.125 km against the corresponding RTP magnetic data. The sampling intervals of 0.125 km used in all the magnetic profiles correspond to a maximum frequency of 4cycles/km equivalent to 8π radians/km. The Origin FFT calculated and gave an output of the frequency, real, imaginary, complex, phase and power components Therefore the FFT estimated Fourier components between zero frequency and the Nyquist limit of 4cycles/km.

The Curie point depth was estimated as suggested by Bhattacharyya and Leu (1975) and Okubo *et. al.*, (1985). The first power spectrum was obtained by plotting a log of square root of power per absolute wave number against absolute wave number. These variables are related as in equation 4.8.

$$Ln\left[\frac{P^{\frac{1}{2}}}{|S|}\right] = LnA - 2\pi|S|z_0 \qquad \text{---------- (4.8)}$$

Equation 4.7 can simplify to the form as

$$LnQ = LnA - 2\pi z_0 X \qquad \text{---------- (4.9)}$$

where $Q = \frac{P^{\frac{1}{2}}}{|S|}$, $X = |S|$ which represents the absolute wave number, P is the power spectra of the anomaly and A is a constant. The depth to the centroid z_o of the magnetic source was determined from the slope of the longest wavelength part of the power spectrum as expressed in equation 4.9. Another power spectrum of logarithm of square root of power against the wave number was plotted for the same profile. Equation 4.10

relates the variables for the spectrum. Both the first and second spectrum for each profile was fitted using the five point adjacent averaging smoothing method.

$$Ln\left[P^{\frac{1}{2}}\right] = LnB - 2\pi|S|z_t \quad \text{---------- (4.10)}$$

Equation 4.10 can be simplified to

$$LnR = LnB - 2\pi z_t X\ , \quad \text{---------- (4.11)}$$

where B is a sum of constants independent of the wave number X.

The depth to the top boundary z_t was obtained from the slope of the second longest wavelength of the spectral segment of the second spectrum. The basal depth which was assumed to be the Curie point depth (Okubo *et.al*, 1985) was calculated from equation 4.12 for profiles AA', BB', CC', DD', EE' and FF' and the results are displayed in Table 4.2. The power spectra of the profiles are displayed as figures 4.14(a), 4.14(b) 4.15(a), 4.15(b), 4.16(a) , 4.16(b), 4.17(a), 4.17(b), 4.18(a), 4.18(b), 4.19(a) and 4.19 (b) respectively.

$$z_b = 2z_0 - z_t \quad \text{---------- (4.12)}$$

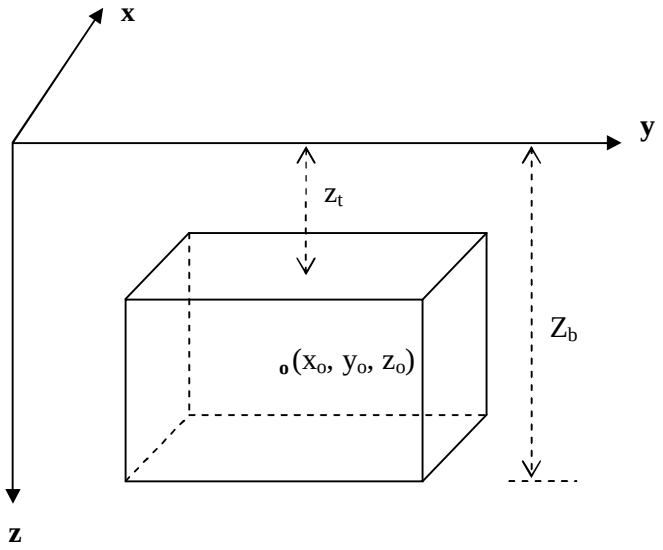

Figure 4.13 Illustration of Curie point depth in a parallelepiped body.

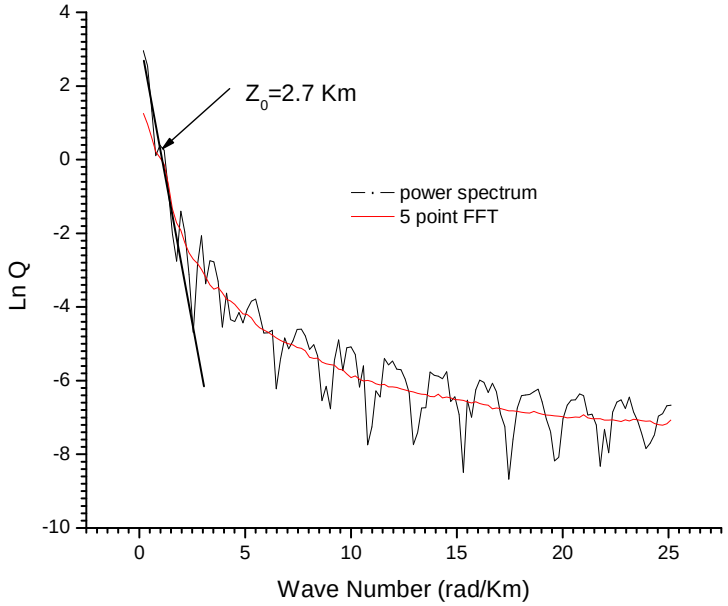

Figure 4.14 (a) Power spectrum of LnQ against wave number for profile AA'.

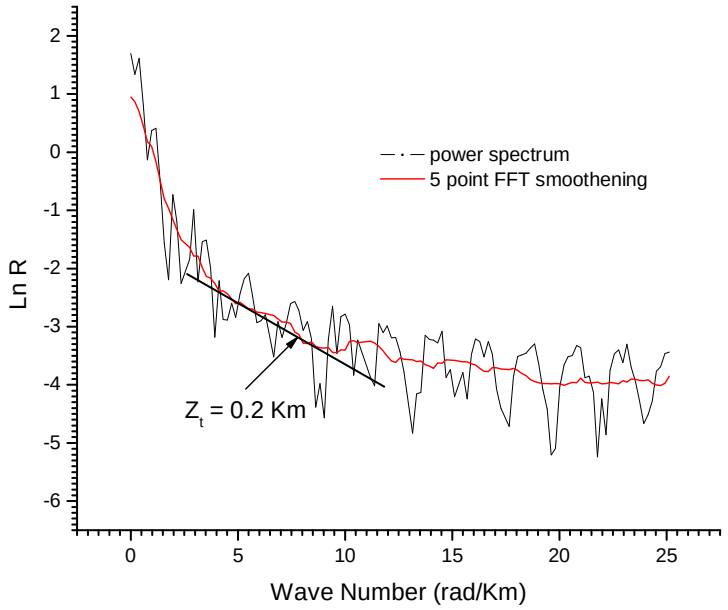

Figure 4.14 (b) Power spectrum of LnR against wave number for profile AA'.

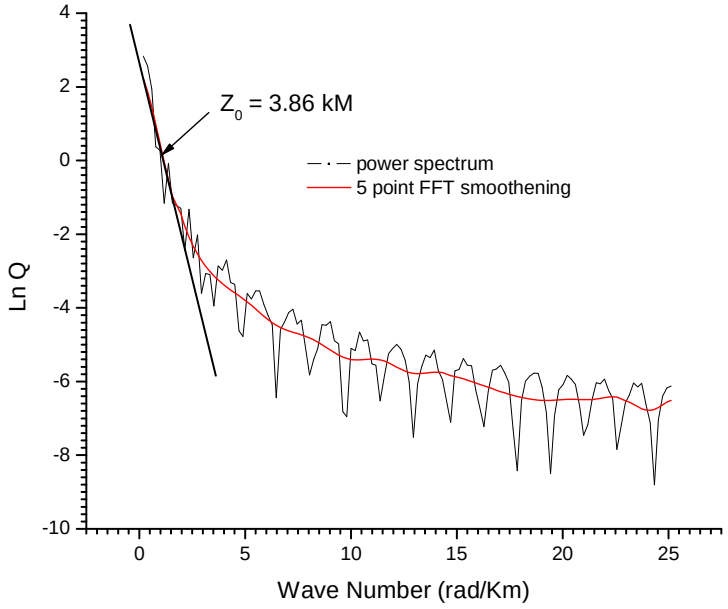

Figure 4.15 (a) Power spectrum of LnQ against wave number for profile BB'.

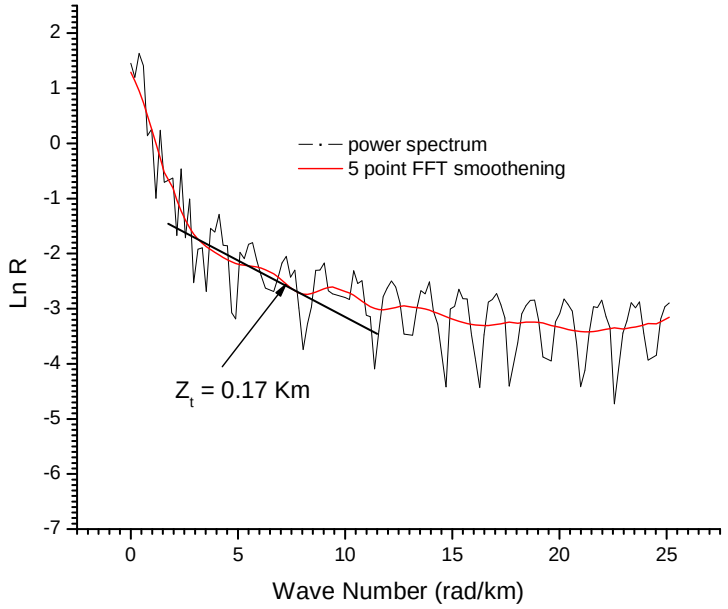

Figure 4.15 (b) Power spectrum of LnR against wave number for profile BB'

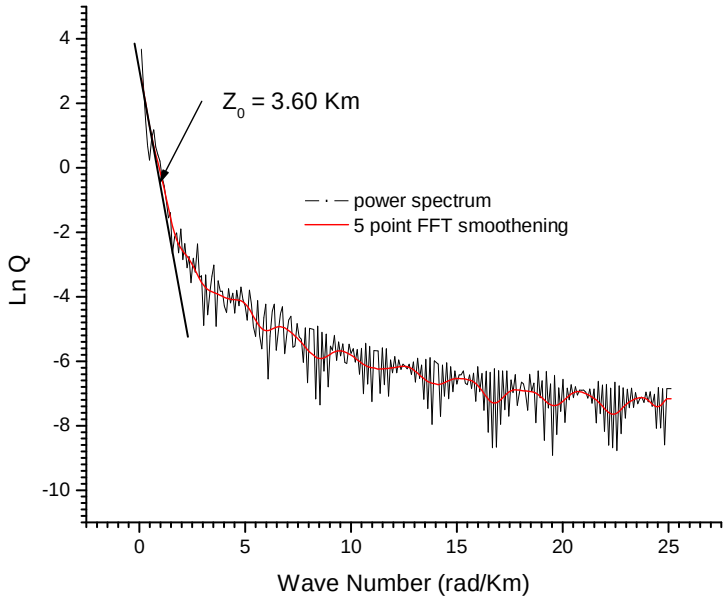

Figure 4.16 (a) Power spectrum of LnQ against wave number for profile CC'.

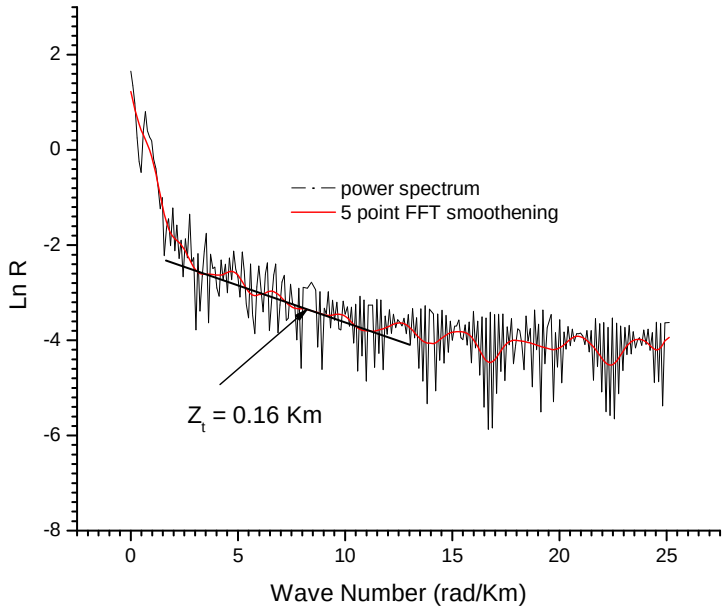

Figure 4.16 (b) Power spectrum of LnR against wave number for profile CC'.

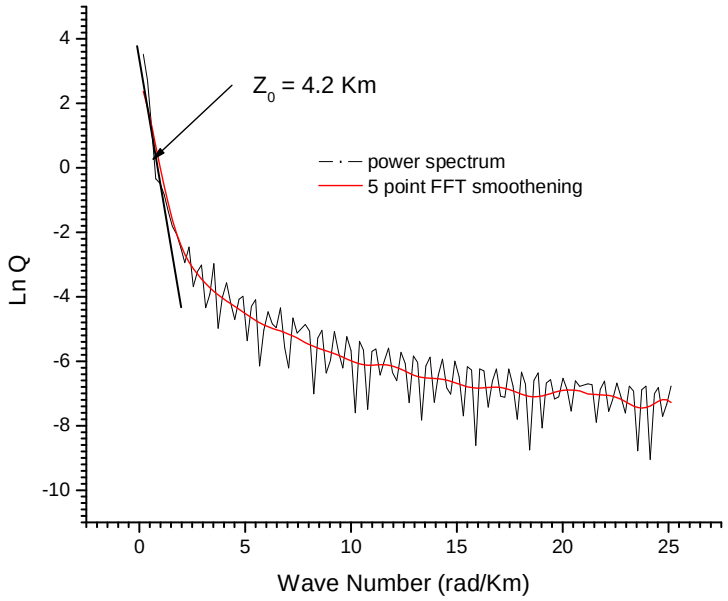

Figure 4.17 (a) Power spectrum of LnQ against wave number for profile DD'.

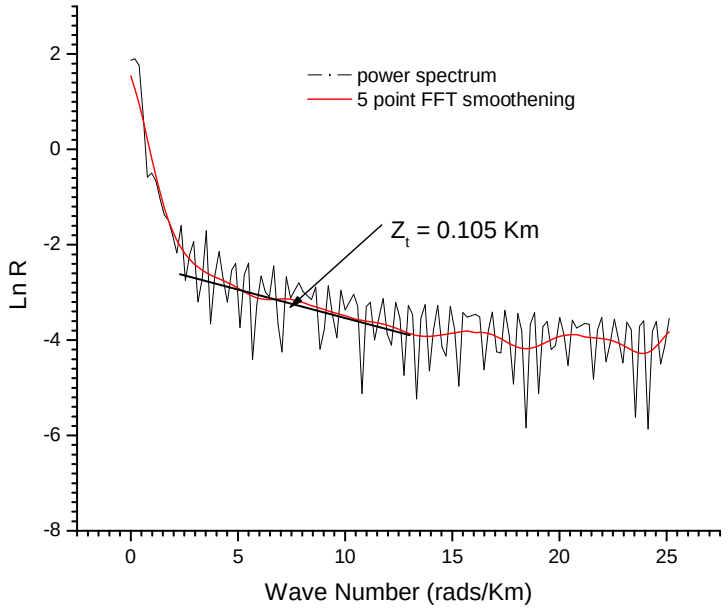

Figure 4.17 (b) Power spectrum of LnR against wave number for profile DD'.

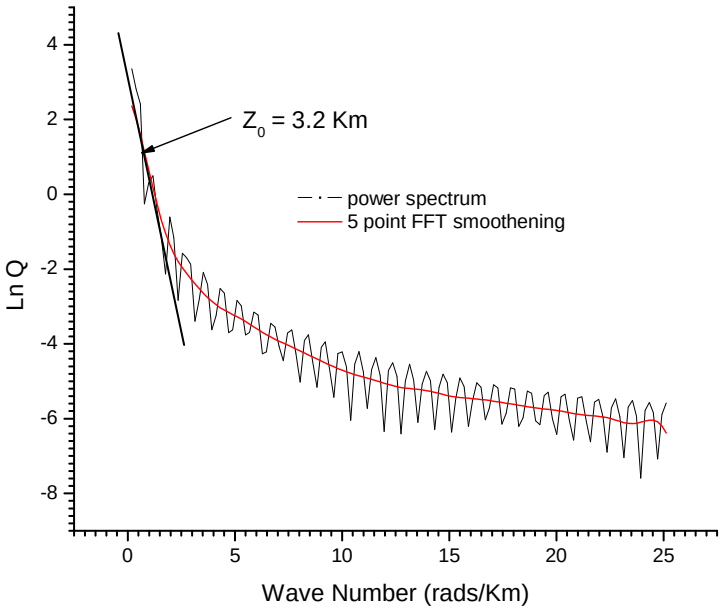

Figure 4.18 (a) Power spectrum of LnQ against wave number for profile EE'.

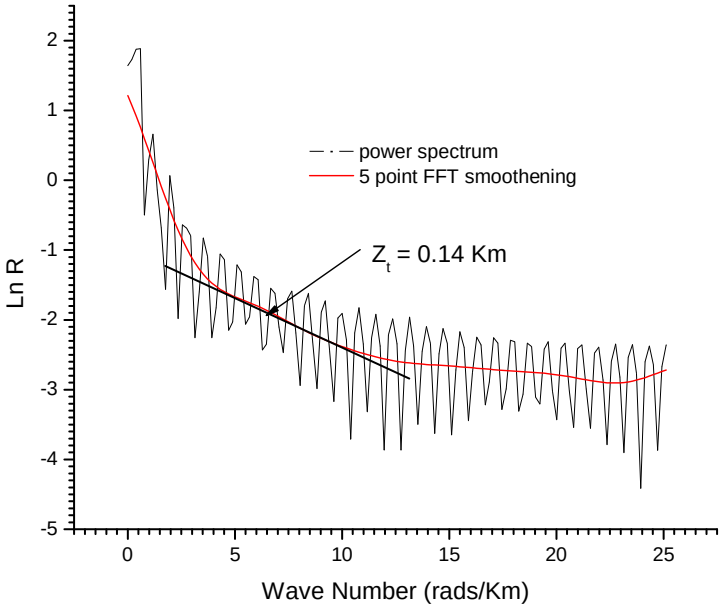

Figure 4.18 (b) Power spectrum of LnR against wave number for profile EE'.

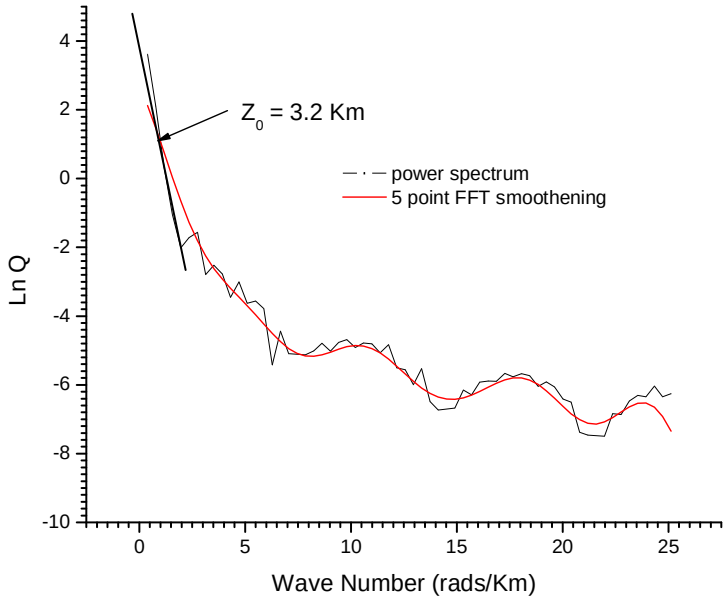

Figure 4.19 (a) Power spectrum of LnQ against wave number for profile FF'.

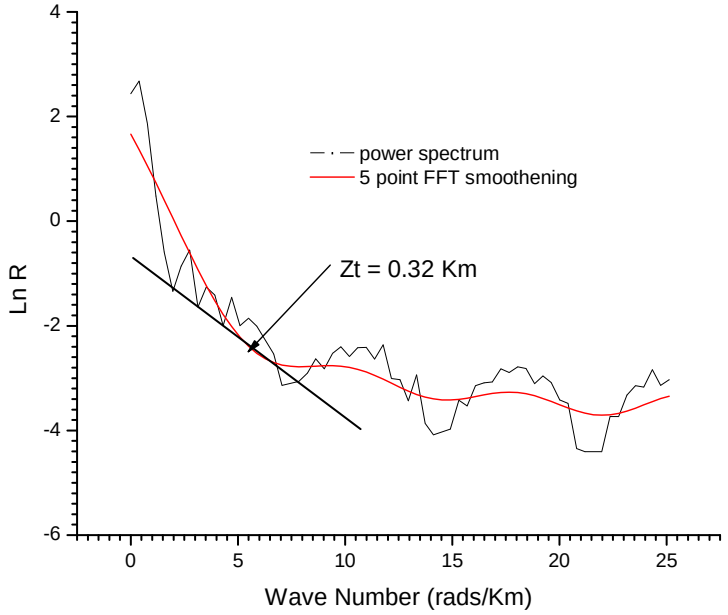

Figure 4.19 (b) Power spectrum of LnR against wave number for profile FF'.

Table 4.2 Curie-point depth estimate along selected profiles.

Profile	Z_o (Km)	Z_t (Km)	Z_b (Km) (Curie-Point depth)
AA'	2.700	0.200	5.200
BB'	3.860	0.170	7.550
CC'	3.600	0.160	7.040
DD'	4.200	0.105	8.295
EE'	3.200	0.140	6.260
FF'	3.200	0.320	6.080

4.2.2.3 Discussion of Curie point depths

The depth Z_t computed using the power spectrum method (Spector and Grant, 1970) and modified by Okubo *et al*. (1985) is the thickness of the sediments overlying the volcanics. The sediments depth Z_t determined along profiles AA', BB', CC', DD', EE' and FF' were 0.2 km, 0.17 km, 0.16 km, 0.105 km and 0.14 km respectively. The Curie point depths calculated were 5.20 km along profile AA', 7.55 km along BB', 7.04 km along CC', 8.29 km along DD', 6.26 km along EE' and 6.08 km along FF'as displayed in Table 4.2. The Curie point depths were considered shallow and are located within the crust. The shallowest depths are on profiles AA' and FF' which traverse along the northern part of the study area. This may indicate presence of the thermal anomaly responsible for the earthquake swarms in the northern region near the little Lake Magadi. The previously determined Curie point depth was used to estimate temperature gradients in the crust. Thermal gradient of each profile was calculated by assuming that rocks are dominated by magnetite which has a Curie temperature of 580˚C. Therefore by dividing the temperature by the depths, the estimated vertical temperature gradients

along profiles AA', BB', CC', DD', EE' and FF'are 111.53˚C/km, 76.82˚C/km, 82.38˚C/km, 69.92˚C/km, 92.65˚C/km and 95.39˚C/km respectively.

4.2.3 Forward Modeling

4.2.3.1 Introduction

This involves determination of the causative body parameters such as its geometry, density contrast, depth of burial and magnetic susceptibility contrast. In this study, two dimensional forward modeling technique was used to generate the source body parameters. In forward modeling, an initial model for the source body is constructed based on prior geological and geophysical knowledge of the study area. The model anomaly is calculated and compared with the observed anomaly. The model parameters are adjusted to improve the fit between the observed and the calculated anomaly. The three-step procedure of body adjustment, anomaly calculation and comparison is repeated until both the calculated and observed anomaly curves achieve a 'best fit'. Due to non-uniqueness in both gravity and magnetic interpretation, prior geophysical and geological information are used as controls to the final models.

4.2.3.2 Forward Modeling of Gravity and Magnetic data

To better understand the geometries, densities and susceptibility contrasts of the causative bodies, forward 2-D modeling for both gravity and magnetic data was done along profiles AA', BB', CC', DD', EE' and FF' using the software Grav.2dc and Mag.2dc(Cooper, pers., comm.) respectively. The modeling software was used to calculate gravitational attraction and magnetic field respectively at each observation point due to polygonal shaped bodies, with each body having a specific density and susceptibility value. In this method, the 2-D arbitrary body is assumed to have an

infinite strike length. A body is approximated by polygons whose gravity or magnetic effects are summed up by numerical integration using an algorithm in both the Grav.2dc and Mag.2dc software. The interactive nature of these software allowed adjustment of the initial start model until an acceptable fit was obtained for the models. The initial body geometries for the modeling process were based on results from Euler deconvolution, spectral analysis and previous geophysical study in the area. The start parameters derived from Euler results were depth and shape of causative body inferred from the structural index used. The Curie point depths determined previously using spectral analysis was used as maximum depth modeled for each of the profiles. As a control, the same density or susceptibility contrast was assigned to bodies above which any two profiles crossed over.

From gravity survey along line G of the KRISP 94 experiment that traversed through Magadi, Birt *et al.* (1997) assigned the near surface sediments and volcanics densities ranging from 2.4 to 2.6 g cm^{-3}. Simiyu (1996) modeled shallow basin structures in the southern Kenyan rift valley by assigning the average density of 2.3 to 2.4 gcm^{-3} for the rift graben fill. Assuming an average crustal density of 2.67 g cm^{-3} in the rift valley as had been deduced from Nettleton's near surface method, a density contrast of -0.27 g cm^{-3} was used for near surface sediments. Birt *et al.* (1997) also assigned basement densities ranges of 2.68 to 2.80 gcm^3 and mid crustal units a range of 2.84 to 2.86 g cm^3. Hay *et al*. (1995) had also modeled the Kenya Rift Ponolites and the lowest crustal unit had a density of 2.95 g cm^{-3} outside the rift and 3.0 g cm^{-3} beneath the active rift zone. This was also used as a control to the density contrasts to avoid unrealistic contrasts. The gravity model generated for a particular profile was used as

the initial start magnetic model. The susceptibility contrast, depth and shape for the individual polygons representing the bodies were interactively altered until a best fit is achieved.

4.2.3.3 Discussion of forward modeling Results

The gravity model along profile AA' in figure 5.1(a) displays three peaks of highs corresponding to relatively denser bodies of density contrasts 0.257, 0.5335 and 0.288 g cm^{-3}. The first and third are within the range as for crustal material as assigned by Birt *et al.* (1997). The gravity high located at a profile distance of 16.7 km has the highest density contrast of 0.5335 g cm^{-3}. Assuming the contrast is relative to average crustal density of 2.67 g cm^{-3}, then the absolute density of the body responsible is 3.20 gcm^{-3} which may be mantle material and hence an intrusive. From the magnetic model AA' in figure 5.1(b), the boundaries do not exactly with those of the gravity model of the same profile. The intrusive in the gravity model is reflected as a highly magnetic body with the highest susceptibility contrast of 0.0428 (SI). The near surface sediments range from a depth of approximately 0.2 km to 2 km for both the gravity and magnetic models. The sediments were modeled to have density contrast of -0.270 gcm^{-3} and susceptibility contrast of 0.0085(SI).

The gravity model along profile BB' has three prominent gravity highs of density contrasts 0.2349. 0.4185 and 0.5335, which corresponds to densities of approximately 2.90, 3.01 and 3.20 respectively. The first density represents lower crust materials while the second or third may represent mantle material. This is also indicated by their susceptibility contrasts being relatively high that is 0.0542(SI) and 0.0428(SI) respectively. Magnetic profile CC' has two lows at profile distances 7 km, 18.5 km and

27.5 km corresponding to bodies of densities 2.5 gcm^{-3}, 2.457 gcm^{-3} and 2.435 gcm^{-3}. The low situated at 7 km profile distance corresponds to a basin to a depth of up to 1km filled with sediments of low susceptibility contrast. The gravity low at 18.5 km corresponds to high magnetic susceptibility contrast that may represent unconsolidated magnetized sediments. A gravity high located 23.5 km is also modeled to have a density of 3.20 gcm^{-3} and susceptibility contrast 0.0503(SI).

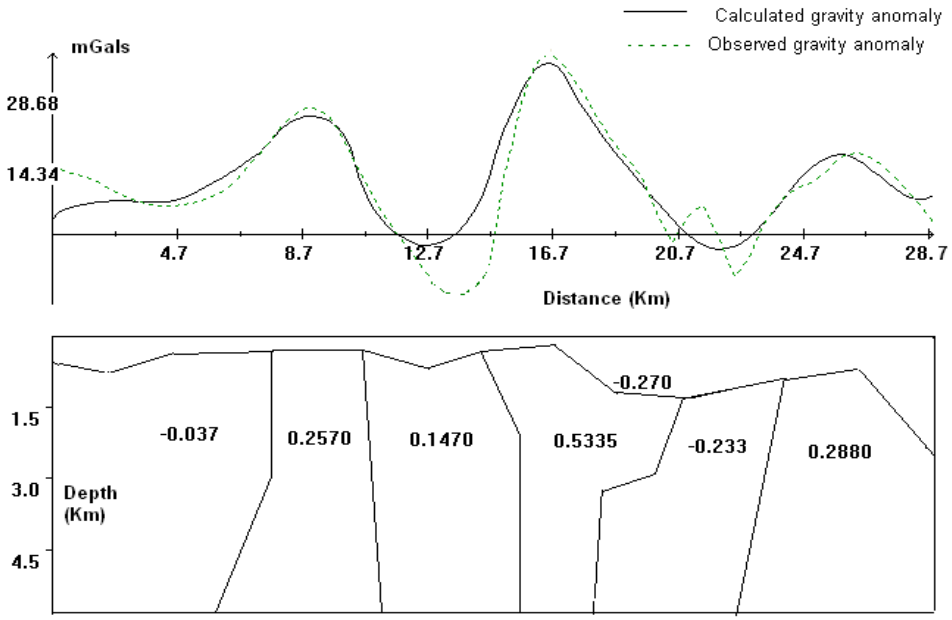

Figure 5.1 (a) Gravity model along profile AA'.

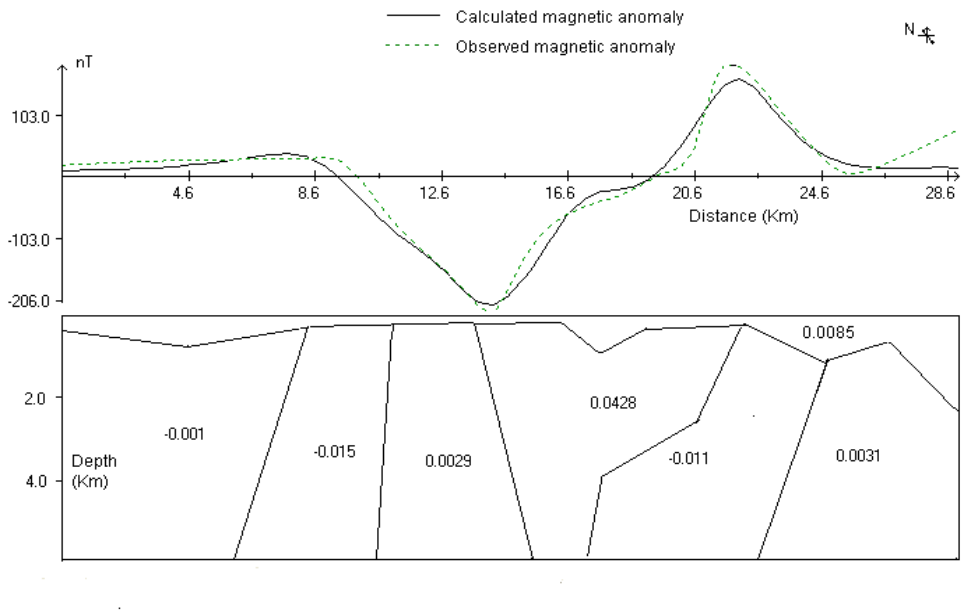

Figure 5.1(b) Magnetic model along profile AA'.

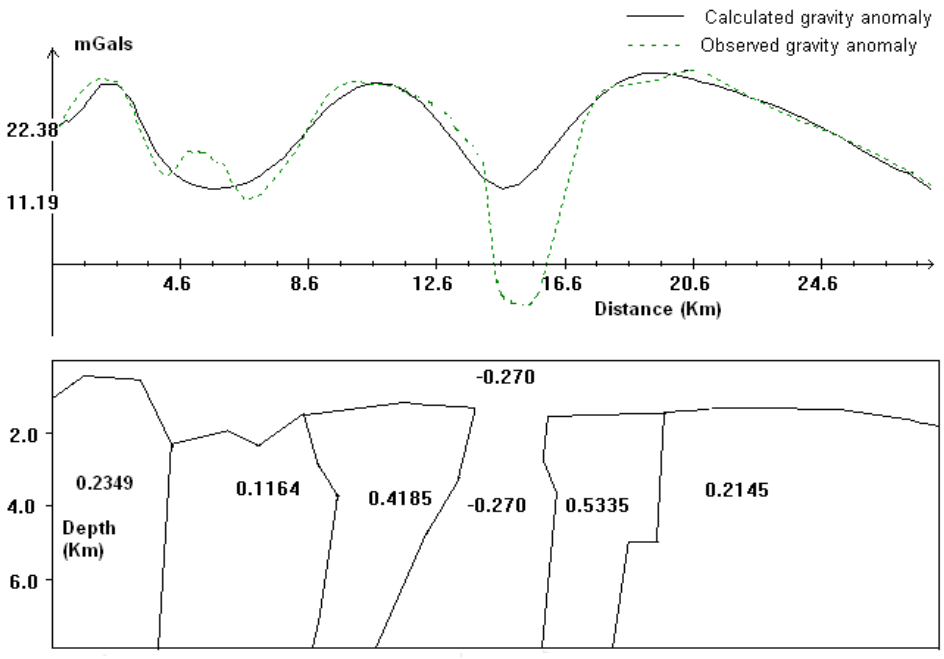

Figure 5.2(a) Gravity model along profile BB'.

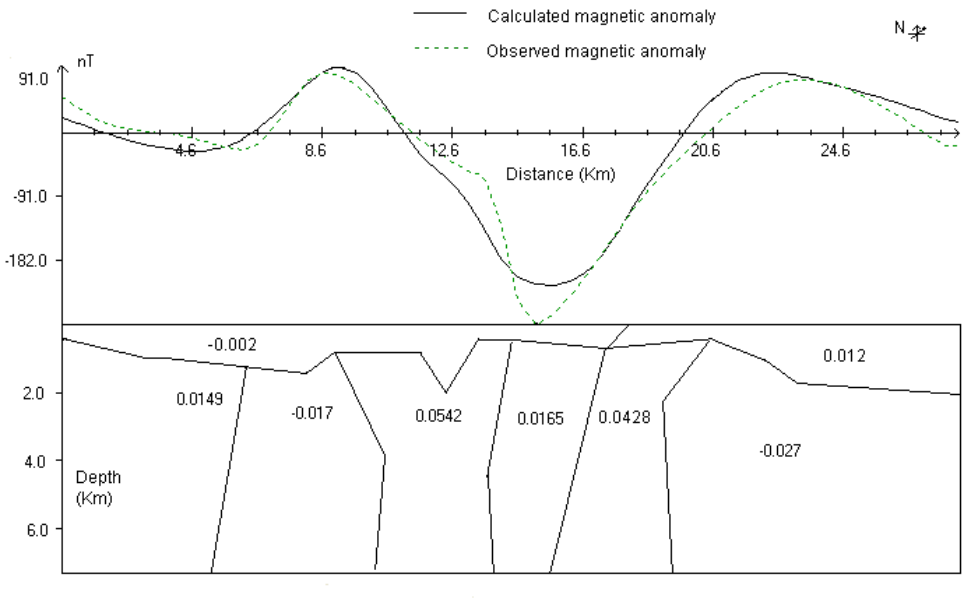

Figure 5.2(b) Magnetic model along profile BB'.

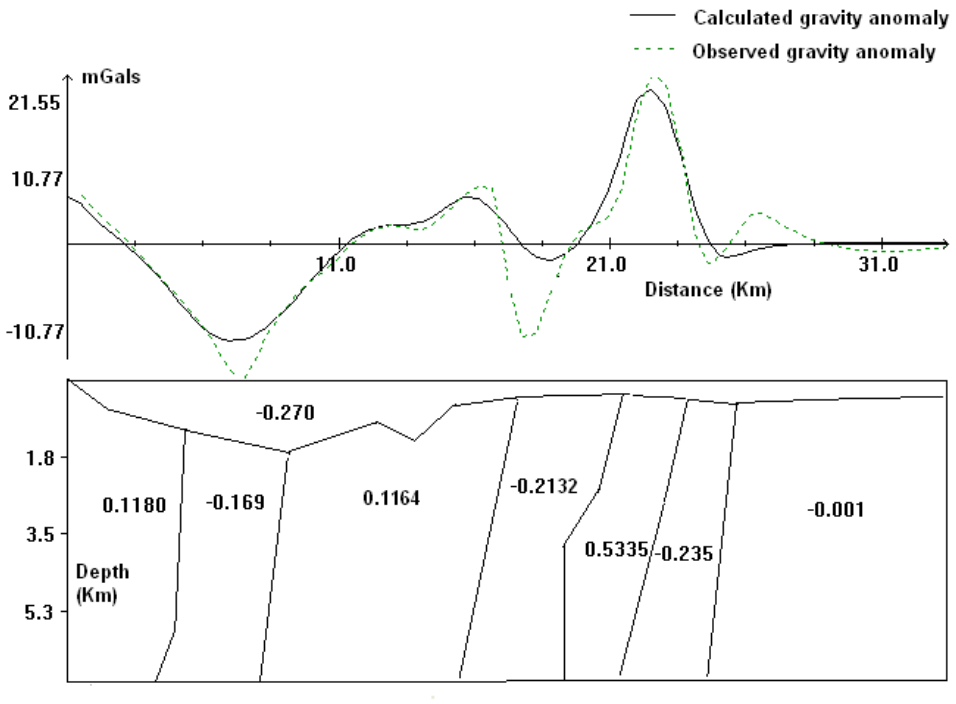

Figure 5.3(a) Gravity model along profile CC'.

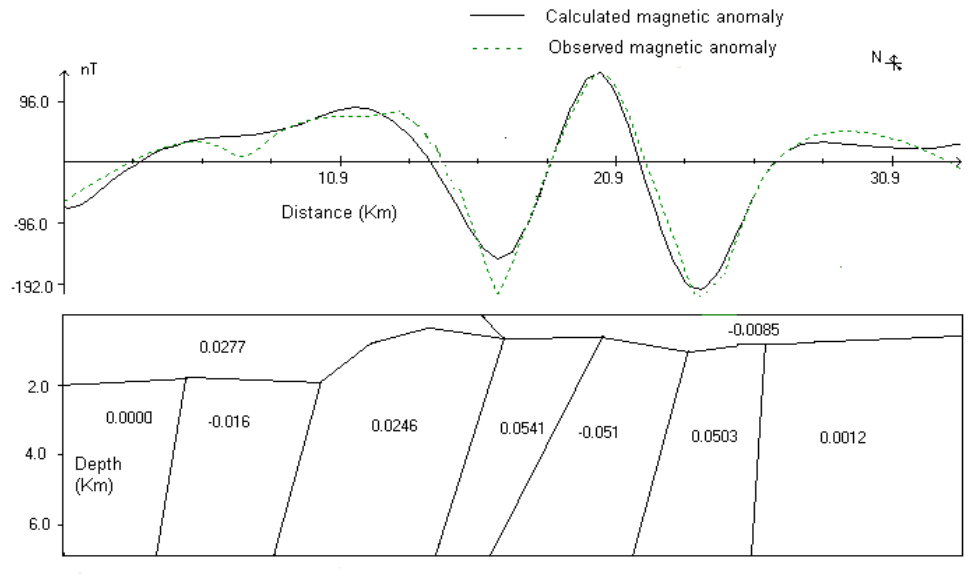

Figure 5.3(b) Magnetic model along profile CC'.

Gravity profile DD' in figure 5.4(a) consists of a long wavelength gravity high superimposed by a gravity low. This high was modeled to consist of a rock of density 3.07 gcm^{-3} impregnated by a material of density 2.445 gcm^{-3}. These may be unconsolidated magnetized sediments of susceptibility contrast of 0.0310 (SI). The near surface sediments were assigned susceptibility contrasts of 0.0063 and 0.0085 (SI) respectively. Gravity profile EE' (figure 5.5(a)) has a high of density 2.88 gcm^{-3} at 6.8 km and a low of 2.4 gcm^{-3} extending from the surface to a depth of more than 5 km. Relatively low susceptibility contrasts of -0.006 and -0.012 (SI) respectively of the sediments indicates that they are unmagnetized. These are lake sediments occurring at Lake Magadi.

At a distance of 11.4 km along profile EE', (figure 5.5), a body is modeled with low density contrast and high susceptibility contrast. This feature had previously been mapped by Githiri *et al,* (2004) and interpreted as magnetized sediments. Along profile FF', (figure 5.6), the sediments from the surface extends up to a maximum depth of 3 km. A gravity high centered at 5.4 km is due to a body of density 2.95 gcm^{-3} which is possibly an intrusive. Its susceptibility contrast is -0.193 (SI) which is relatively low implying an unmagnetized high density material. At 10.4 km profile distance, the gravity model has a low which may be contributed to by a deeper sediment basin underlain by volcanics of density 2.545 gcm^{-3} but the magnetic profile indicates the material to be from a depth of approximately 0.5 km. This is displayed as a discrepancy in depth between the depth from the density and magnetic models. In all the profiles, the depth to basement was not clearly discerned because anomalies due to the basement were interfered to by stronger magnetic contrasts from volcanics.

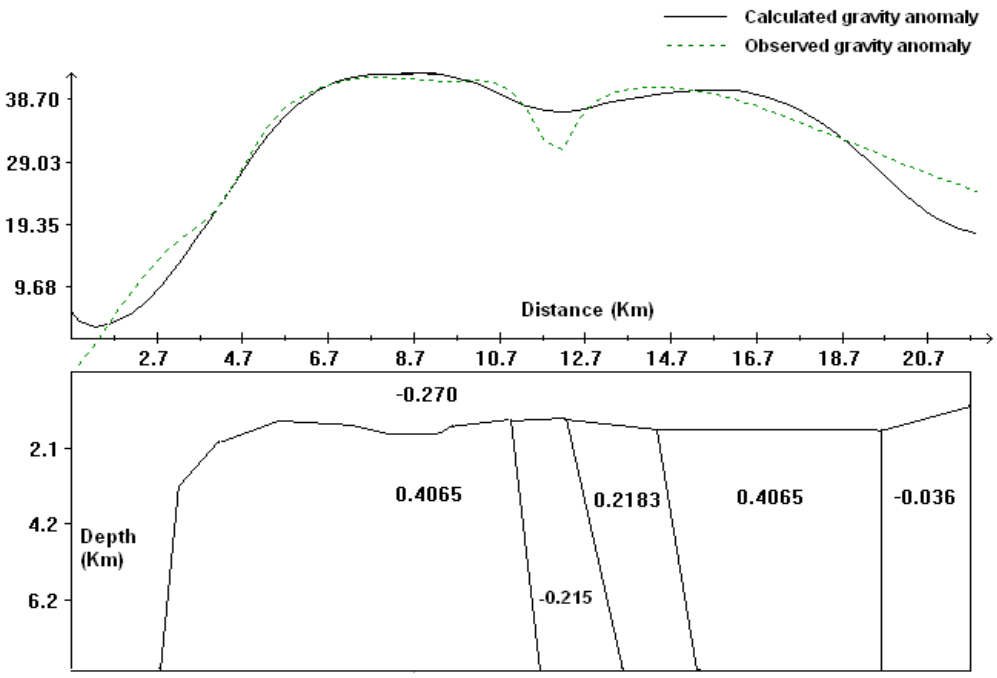

Figure 5.4(a) Gravity model along profile DD'.

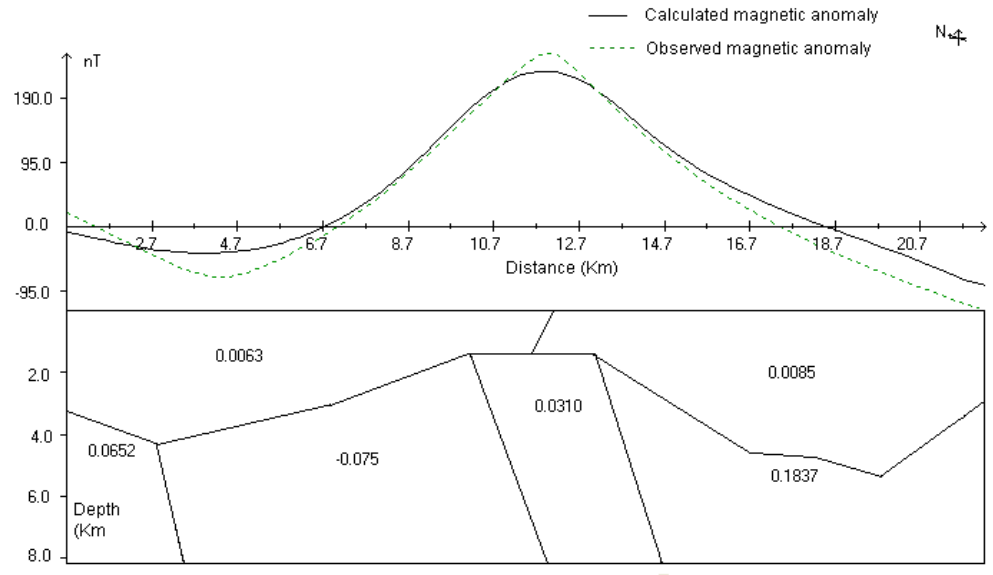

Figure 5.4(b) Magnetic model along profile DD'.

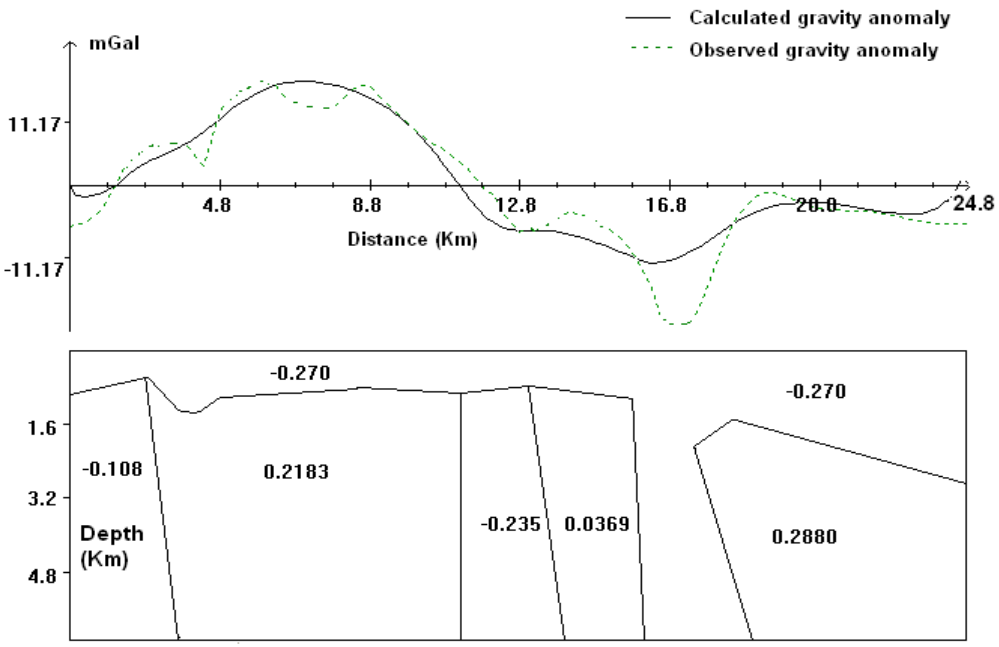

Figure 5.5(a) Gravity model along profile EE'.

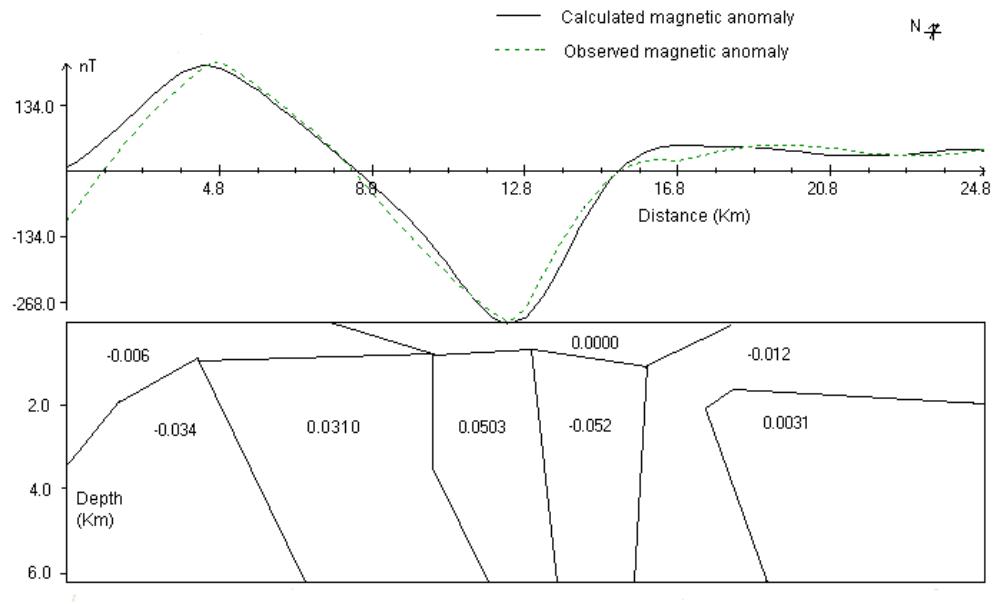

Figure 5.5(b) Magnetic model along profile EE'.

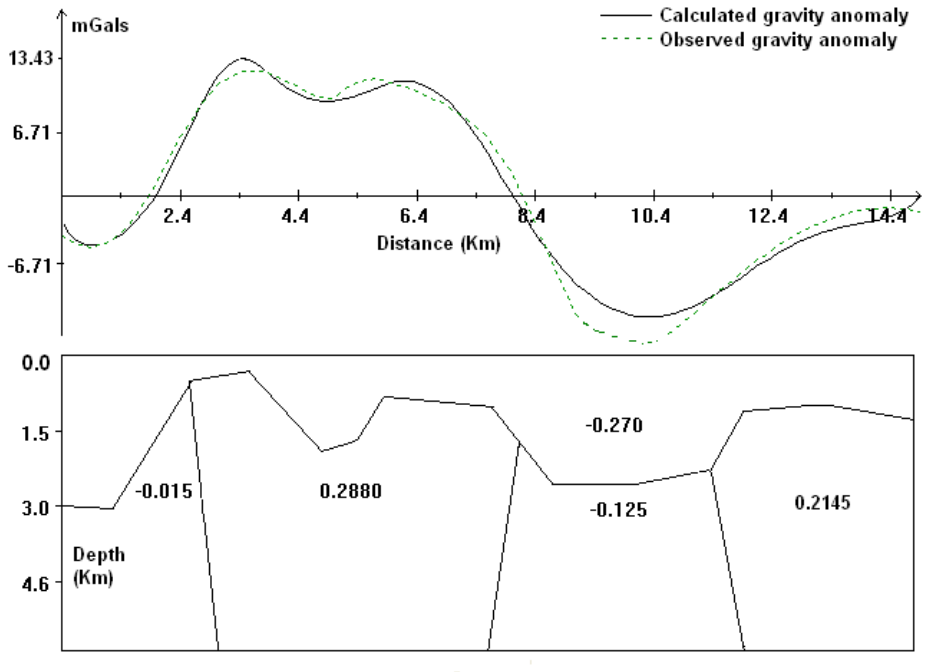

Figure 5.6(a) Gravity model along profile FF'.

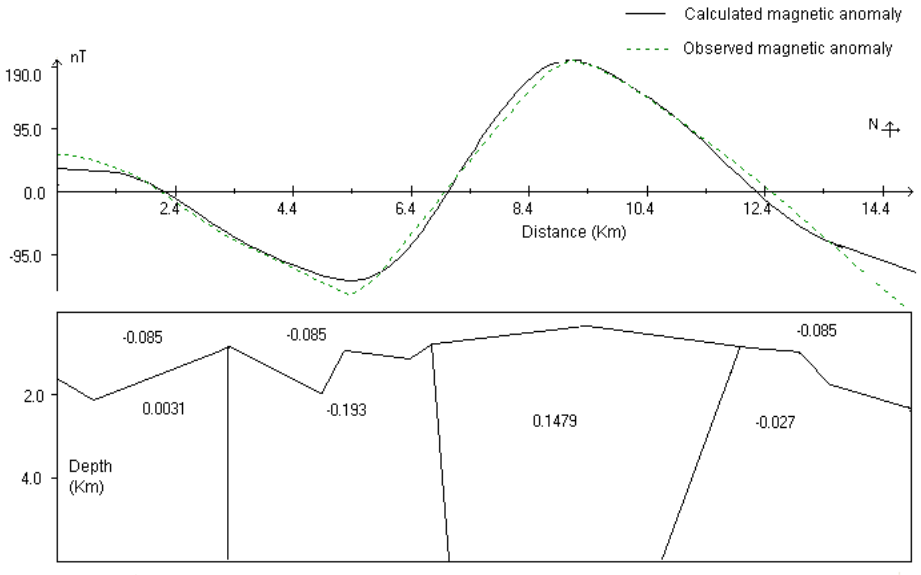

Figure 5.6(b) Magnetic model along profile FF'.

CHAPTER FIVE

CONCLUSION AND RECOMMENDATIONS

5.1 CONCLUSION

The application of both gravity and magnetic prospecting methods in Magadi has revealed presence of bodies with density contrast and susceptibility contrast that may be magmatic intrusions. The most prominent such bodies transacted by both profiles AA' and BB' is centred at location with coordinates (196, 9805) and another by profile CC' centred at coordinates (197, 9789). They are both modelled to have density of 3.20 gcm^{-3} and susceptibility contrast of 0.0428 SI and 0.053 SI. It is evident from spectral analysis that the Curie point depths estimated at Magadi are relatively low, ranging between 5.2 and 8.3 km. The Curie point depth along profile AA' is 5.2 km which is the shallowest followed by profile FF' with a depth of 6.08 km, all traversing the northern part of the study area. The estimated vertical temperature gradients along profiles AA', BB', CC', DD', EE' and FF' were found to be 111.53˚C/km, 76.82˚C/km, 82.38˚C/km, 69.92˚C/km, 92.65˚C/km and 95.39˚C/km respectively. The results clearly indicate presence of a shallow heat source at the northern part of Lake Magadi traversed by profiles AA' and FF'. The body of high density and susceptibility contrasts modeled along profile CC' may have cooled and hence the isotherm is deeper. From the seismotectonic study by Ibs-Von Seht *et al* (2001), a locally up-warped brittle-ductile transition was found to occur at a depth of 15 km in the south and 10 km in the north. This confirms presence of a low shear strength material at a relatively shallow depth north than south. The location of the earthquake swarms is traversed by profile AA' on the northern region and coincides in position to the body modelled with the high density and magnetic susceptibility contrasts. Therefore from the results of this

study, the detected relatively shallow intusives of high density and high susceptibility contrast at high temperature may be emanating from a magma chamber. Therefore this magma may be used as a heat source for a geothermal resource. The hot magma penetrates through the rocks increasing stress which on release causes the earthquakes. Chances of an occurrence of a major earthquake are still high as the hot magma is continually increasing strain in the rocks. This section of the southern rift is still active as recently demonstrated when Oldoinyo-Lengai a volcano in Tanzania at close proximity to Magadi area erupted. Prior to its eruption, major earthquakes were experienced whose effects were felt all over East-Africa.

5.2 RECOMMENDATIONS

The results of this study have highlighted areas with potential for geothermal energy exploration. The detected heat sources could in future trigger major seismic events which may cause destruction of building structures in the proximity. Therefore design of earthquake resistant structures is recommended in cities close to the study zone.

Nevertheless, the gravity and magnetic stations established in the northern region affected by the earthquake cluster in this study were not adequately spaced to offer high resolution imaging of the subsurface. A portion of this area is occupied by the General Service Unit training school, a paramilitary wing of the Kenya police. This being a restricted area, no data was collected at the locality. The north western region is of rough terrain making it inaccessible by road. The area was accessed by foot from the main road and hence few stations were established.

A detailed gravity and magnetic reconnaissance survey needs to be carried out in the northern region bounded by grid northing 9800 to 9825 and grid easting 190 to 215. In the southern region, the survey should be concentrated on the area bounded by grid northing 9774 to 9784 and grid easting 194 to 204. Due to the above limitations encountered in the northern region, an operation camp to be set near these sites to ease accessibility to an adequate number of stations. Prior to the survey, permission should be sought from the Kenya police so as to cover the region occupied by the training school.

REFERENCES

Am, K., 1972. The arbitrarily magnetised dike: interpretation by characteristics: Geoexpl, 10, pp. 63-90.

Atmaoui, N., 1999. Sructural analysis of neotectonic joints at Lake Magadi area and their relationship with regional faults using remote sensing imagery interpretation. M.Sc thesis, University of Nairobi pp.100-101.

Baker, B.H., 1958. Geology of the Magadi area. Report Geological survey of Kenya 42. The Government printer, Nairobi.

Baker, B.H., 1963. Geology of the area south of Magadi. Report Geological survey of Kenya 61. The Government printer, Nairobi.

Baker, B.H., Mohr, P.A. and Williams, L.A.J., 1972. Geology of the Eastern Rift system of Africa. Geol. Soc. Am., special paper, 136, p.67.

Baker, B.H. and Wohlenberg, J, 1971. Structure and evolution of the Kenya Rift Valley. Nature, 229: pp. 538-542.

Baker, B.H., 1986. Tectonics and Volcanism of the Southern Kenya Rift valley and its influence on rift sedimentation. In: Frostick, L.E. et al. (eds) 1986, sedimentation in the African Rifts. Geol. Soc. Spec. Publ. No 25, pp. 45-47.

Bhattacharyya B.K., and Leu L.K., 1975, Spectral analysis of gravity and magnetic analysis due to two dimensionless structures. Geophysics 40, pp. 993-1013.

Billings, S., and Richards, D., 2000, Quality control of gridded aeromagnetic data, Exploration Geophysics, vol. 22, pp. 547-555.

Birt C.S, Maguire, P.K.H., Khan, M.A., Thybo, H., Keller, G.R., Patel, J., 1997. The influence of pre-existing structures on the evolution of the southern Kenya

rift valley- evidence from seismic and gravity studies. Tectonophysics 278, pp. 211-242.

Blakely, R. J., 1995. Potential theory in Gravity and Magnetic applications. Cambridge university press, United Kingdom p. 70, and pp. 285-303.

Bonjer, K.P., Fuchs K., and Wohlenberg, J., 1970. Crustal structure of the East African Rift System from spectral response ratios of long period body waves .Z. Geophys. 36: pp. 287 - 297.

Bosum, W., 1968, Ein automatisches Verfahren Zur Interpretation magnetischer Anomalien nach der Methode der Kleinsten Quadrate: Geophys. Prosp., 16, pp. 107-126.

Bullard, E.C., 1949. The Magnetic field within the Earth. Proc. Roy. Soc. A, 197, p. 433.

Cordell, L., 1979. Gravimetric expression of graben faulting in the Santa Fe country and the Espanola Basin, New Mexico. Guide book to Santa Fe country, 30th field conference, R.V Ingersol (ed), New Mexico Geological society, pp. 59-64.

Cordell, L., and Grauch, V.J.S., 1985. Mapping basement magnetisation zones from aeromagnetic data in the San Juan basin, New Mexico. Utility of regional gravity and magnetic anomaly maps, William J. Hinze (ed), Society Of Exploration Geophysicists, Tulsa, OK, pp.181-197.

Crossley, R., 1979. Structure and volcanism in the southern Kenya Rift. In Geodynamic evolution of the Afro- Arabian Rift System. Acad. Nazionale dei Lincei, Rome, pp. 89-98.

David G.S., 1981. Cambridge Encyclopedia of Earth Sciences. Cambridge university press, London, p. 400.

Dobrin, M.B. and Savit, C.H., 1988. Introduction to Geophysical prospecting. McGraw-Hill Inc, New York. p.706.

Elasser W.M., 1956. Hydro-Magnetic dynamo theory. Revs. Mod. Phys. Vol 28, p. 135.

Fukushima N and Kaminde Y., 1973. Partial ring currents model for world wide geomagnetic disturbances. Rev. Geophys. Space phys, 11 pp. 795-853.

Girdler, R.W., Fairhead, J.D., Seale, R.C., and Sowerbutts, W.T.C., 1969. Evolution of rifting in Africa, Nature (London), and Physical Science, 224: pp.1178-1182.

Githiri, J.G., Stangl R.L., Waithaka J.W. and Dindi E.W., 2004. Ground magnetic survey of Magadi geothermal field. East African journal of Physical sciences, Vol: 5-2, pp. 69-80.

Githiri, J.G., Waithaka J.W., Okumu J., and Stangl R.L. 2005. Gravity survey of Lake Magadi area. East African journal of Physical sciences, Vol: 6-2, pp. 89-100.

Gregory, .W., 1921, The rift valleys and geology of East Africa: London, Seeley, Service, p. 479

Hammer, S., 1939. Terrain corrections for gravimeter stations. Geophysics. 4: pp.184-194.

Hay, D.E., Wendlandt, R.F., Keller, G.R., 1995. Origin of Kenya Rift plateau-type phonolites: Integrated petrological and geophysical constraints on the evolution of the crust and upper mantle beneath the Kenya Rift.J. Geophys. Res. 100, pp.10549-10557.

Healey, J., 1975. Geothermal fields in zones of recent volcanism. Proc. Second U.N. Symp. Development and Use of Geothermal resources, San Francisco, Carlifornia, pp. 415-422.

Heikkinen, M., 1979, On the Honkasalo term in tidal corrections to gravimetric observations: Journal of Geodesy, 53, pp. 239-245.

Heiskanen, W.A., and Moritz, H., 1969, Physical geodesy: W.H. Freeman Co.

Henry, W.J., Mechie, J., Maguire, P.K.H., Khan, M.A. Prodehl, C., Keller, G.R and Patel, J., 1990. A Seismic Investigation of the Kenya Rift Valley. Geophys. J. Int., 10: pp. 107-130.

Honkasalo, T., **1964,** On the tidal gravity correction: Bulletin of Theoretical and Applied Geophysics, 6, pp. 34-36.

Hsu Shu-Kun, 2002. Imaging magnetic sources using Euler's equation. Geophysical prospecting Vol. 50, pp. 15-25.

Ibs-Von Seht, M., Blumenstein, S., Wagner, R., Hollnack, D. and Wohlenberg, J., 2001. Seismicity, Seismotectonics and Crustal structure of the southern Kenya Rift-new data from Lake Magadi area. Geophys.J Int. Vol. 146, pp. 439-453.

Jung, K., 1961. Schwerkraftverfahren in der angewandten Geophysik: Geest und Portig, p.8.

Kearey, P., and Brooks M., 1984. An Introduction to Geophysical Exploration. Blackwell Scientific Publications, pp. 125-126.

Khan, M.A., and Swain, C.J., 1977. A catalogue of Gravity measurements in Kenya. Department of Geology, Leicester Univ, pp. 21-22.

KRISP working group, 1987. Structure of the Kenyan rift from Seismic refraction. Nature, 325: pp. 239-242.

Maguire, P.K.H and Long, R.E., 1976. The structure of the Western flank of the Gregory Rift, Part 2. The Mantle. Geophys. J.R. Astron. Soc., 44: pp. 677-688.

McCall, G.H., 1967. Geology of Nakuru-Thompsons falls-Lake Hannington areas, Geological survey of Kenya, report 78. Altherr, R., Muller, B. and Prodehl, C. (editors), Stress and stress release in the lithosphere, Tectonophysics, 278: pp.17.

Mohr, P.J., and Taylor, B.N., 2001. The fundamental physical constant: Physics Today, 54, pp. 6-16.

Molnar, P. and Aggarwal, Y.P., 1971. A micro-earthquake survey in Kenya, Bull. Seism. Soc. Am, Vol. 61: pp. 195-201.

Morelli, C., 1974. The International Gravity Standardization Net 1971: International Association of Geodesy, Special Publication 4.

Moritz, H., 1980, Geodetic Reference System 1980: Journal of Geodesy, 54, pp. 395-405.

Mushayandebvu, M.F., Van Driel, P., Reid, A.B. and Fairhead, J.D., 2001, Magnetic source parameters of two-dimensional structures using extended Euler deconvolution: Geophysics, 66, pp. 814-823.

Nagata, T., 1961. Rock Magnetism, Maruzen, Tokyo, p. 350.

Nnange, J.M., Ngako, V., Fairhead, J.D., and Ebinger, C.J., 2000. Depth to density discontinuities beneath the Adamawa plateau region, central Africa, from spectral analyses of new existing gravity data, Journal of African Earth science Ltd., vol 30, no. 3, pp. 887-901.

Nettleton, L.L., 1939. Determination of density for reduction of gravimeter observations. Geophysics, Vol. 4 pp. 176-183.

Nettleton, L.L., 1954. Regionals, Residuals and structures. Geophysics, Vol. 19: pp. 1-22.

Nettleton, L.L., 1976. Gravity and Magnetic in Oil prospecting. International series in the Earth and planetary sciences., Mc Graw-Hill, Inc., p. 333.

Okubo, Y., Graf J.R., Hansen R.O., Ogawa K., and Tsu H., 1985. Curie point depths of the island of Kyushu and surrounding areas, Japan, Geophysics, 53, pp. 481-494.

Parasnis D.S., 1986. Principles of Applied Geophysics, Chapman and Hall, U.S.A. pp. 14-29.

Riaroh, D., Okoth, W., 1994. The geothermal fields of the Kenya Rift. Tectonophysics 236: pp.117-130.

Reid A.B., Allsop J.M., Granser H., Millets A.J., and Somerton I.W., 1990. Magnetic interpretation in three dimensions using Euler deconvolution. Geophysics, Vol. 55: pp. 80-91.

Searle, R.C., 1970. Evidence from gravity anomalies for the thinning of the lithosphere beneath the rift valley of Kenya, Geophysical Journal.21: pp 13-21.

Simiyu, S.M., 1996. Intergrated geophysical study of the crustal structure of the southern Kenya Rift, East Africa. Tectonics ,12, pp. 591-606.

Simpson, F., Haak, V. and Khan, M.A., 1997. The KRISP-94 magnetotelluric survey of early 1995: first results. Tectonophysics 128, pp. 27.

Smith, M., 1994. Stratigraphic and structural constraints on mechanisms of active rifting in the Gregory Rift, Kenya, in; Prodehl, C., Keller, G.R and Khan, M.A (editors), crustal and upper-mantle structure of the Kenya Rift, Tectonophysics, 236: pp. 3-22.

Smith, M. and Mosley, P., 1993. Crustal heterogeneity and basement influence on the development of the Kenya Rift, East Africa Tectonics, 12: pp. 591 - 606.

Somigliana, C., 1930, Geofisica-Sul campo gravitazionale esterno del geoide ellissoidico: Atti della Accademia nazionale dei Lincei. Rendiconti. Classe di scienze fisinche, matematiche e naturali, 6, pp. 237-243.

Spector, A., and Grant, F.S., 1970, Statistical models for interpreting aeromagnetic data: Geophysics, 35, pp. 2983-3002.

Uotila, U.A., 1980, Note to users on International Gravity Standardization Net 1971: Journal of Geodesy, 54, pp. 407-408.

Williamson, K. H., 1975. Terrestrial heat flow studies in Kenya. Ph.D. Thesis**, Univ**. London p. 290.

Wohlenberg, J. and Bhatt, N.V., 1972. A report on aeromagnetic surveys of two areas in the Kenya Rift Valley: Tectonophysics, 15/ 1, 2 pp. 143-149.

Wolff. H., 1992. Interpretation Magnetischer Daten aus dem Sudlichen Kenya Rift. Geologische Diploma beit Vorgelegt Von p.59.

Appendix: A

The tables A1 display listings of trend equations fitted as regional for different profiles.

Table: A.1. Listing of regional trend equation for gravity profiles.

Gravity Profiles Trend Analysis	
Profile	**Regional Trend**
AA'	$Y = 11.76 - 1.327*X + 0.07628*X^2$
BB'	$Y = 8.19 – 3.306*X + 0.10617*X^2$
CC'	$Y = -23.49 + 4.935*X – 0.12161X^2$
DD'	$Y = 2.83*X - 1761.9$
EE'	$Y = 2.04*X - 1737.6$
FF'	$Y = 2.34*X - 1695.0$

Table: A.2. Listing of regional trend equation for magnetic profiles.

Magnetic Profiles Trend Analysis	
Profile	**Regional Trend**
AA'	$Y = - 4.47*X + 33355.9$
BB'	$Y = - 4.88*X + 33438.4$
CC'	$Y = - 0.16*X + 33397.1$
DD'	$Y = 15.25*X + 33348.1$
EE'	$Y = - 18.74*X + 33691.5$
FF'	$Y = 1.584*X + 33188.1$

Appendix B: Gravimeter Drift Curves

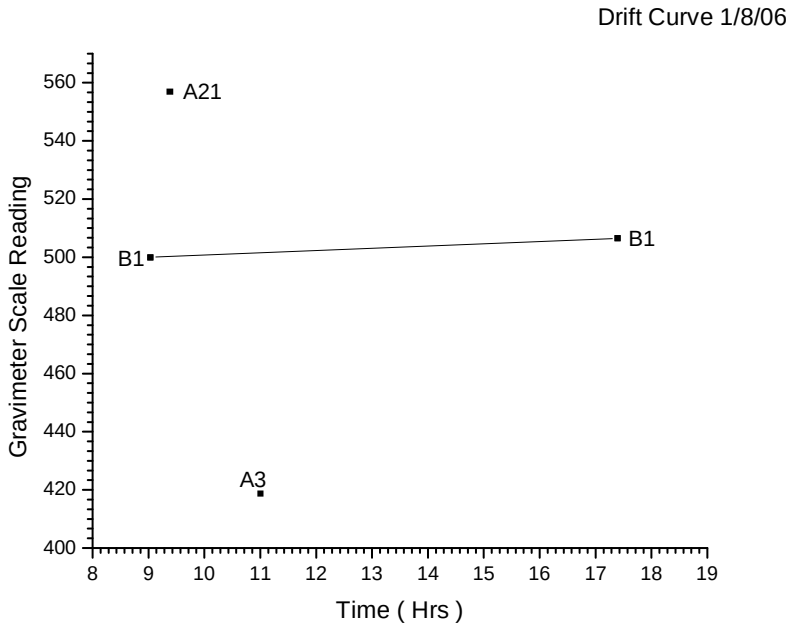

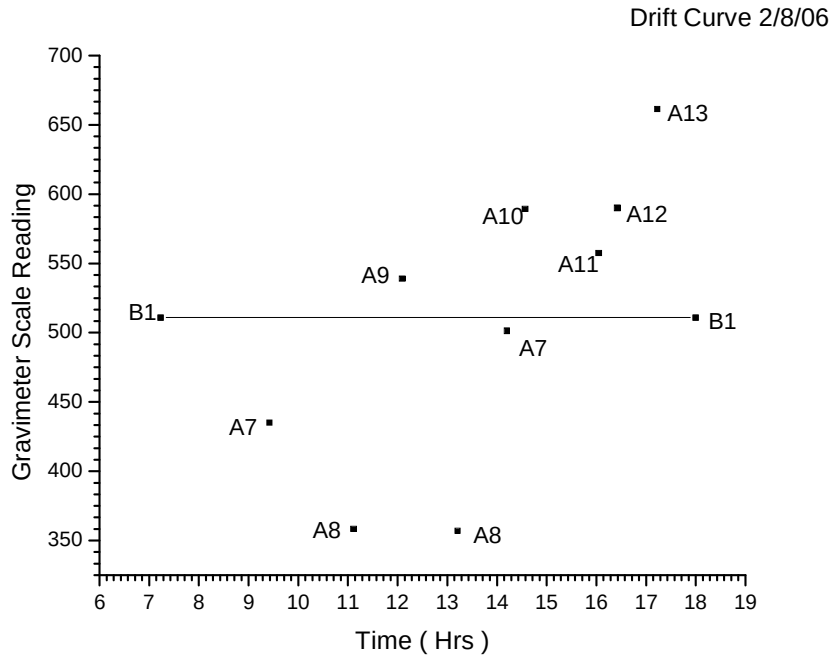

Drift Curve 3/8/06

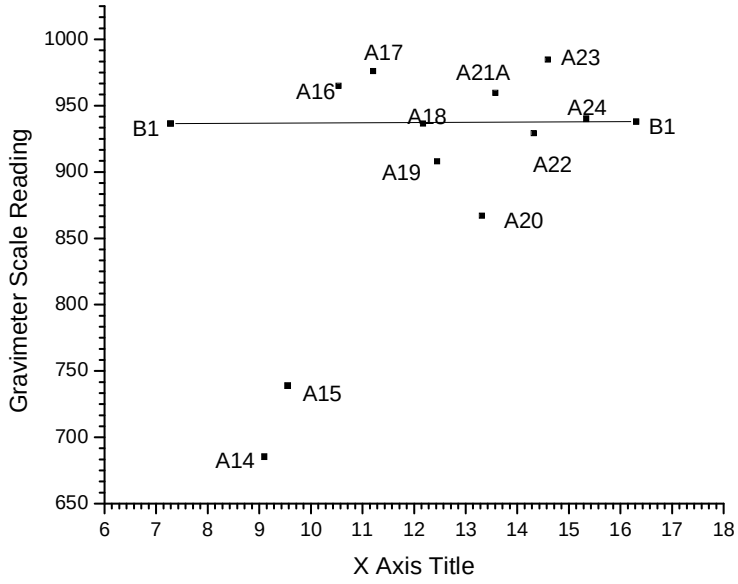

Drift Curve 4/8/06

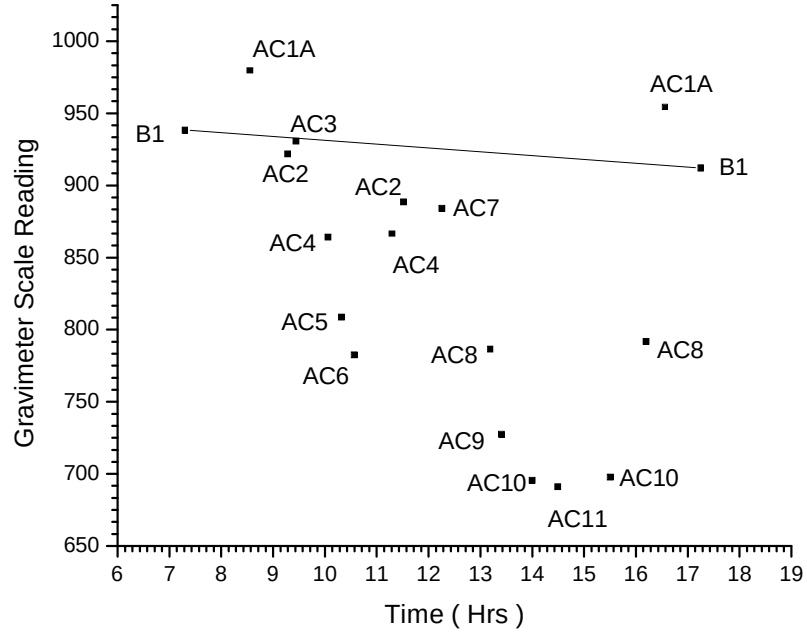

Drift Curve 5/8/06

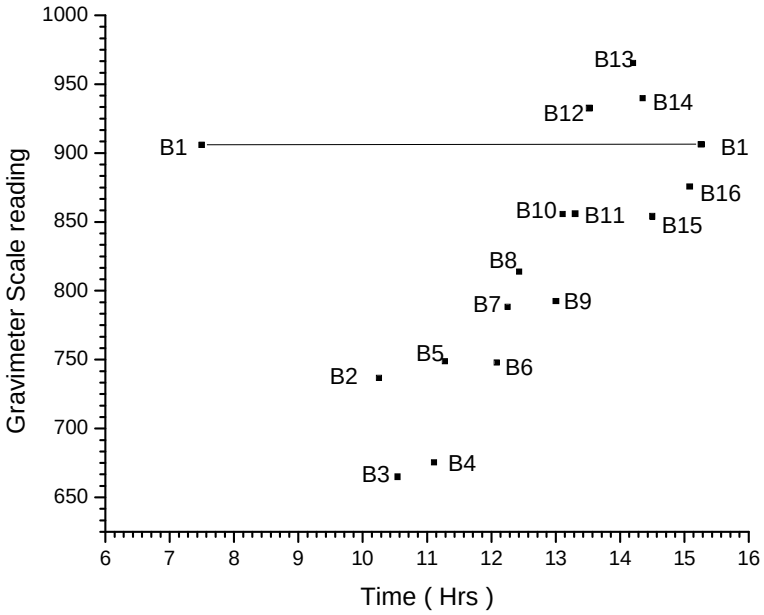

Drift Curve 7/8/06

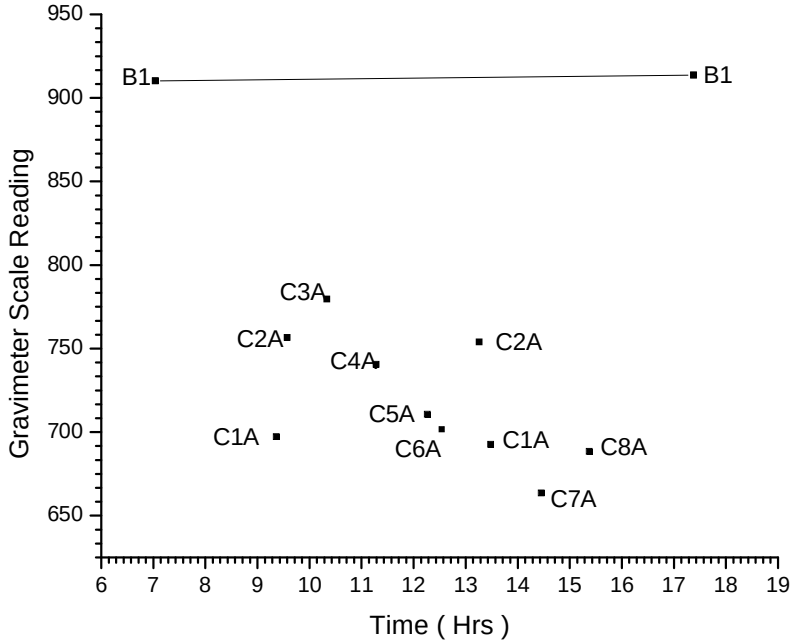

Drift Curve 8/8/06

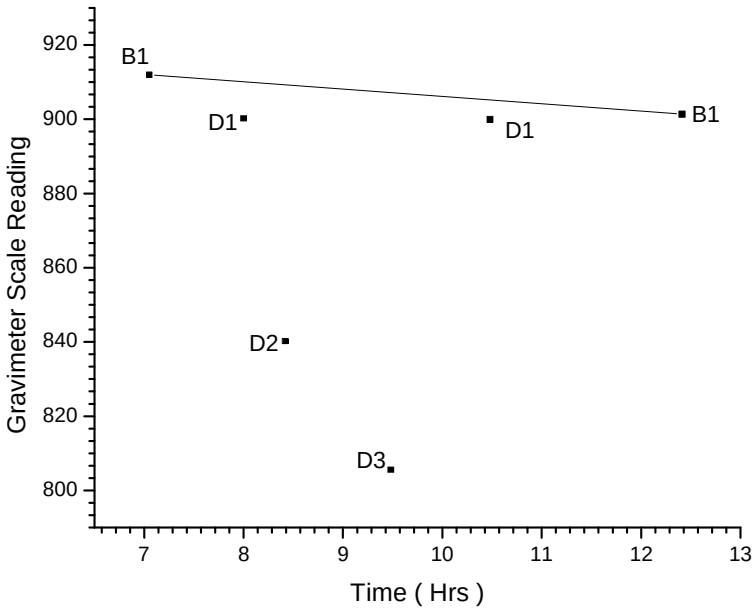

Appendix C: Diurnal Variation Curves

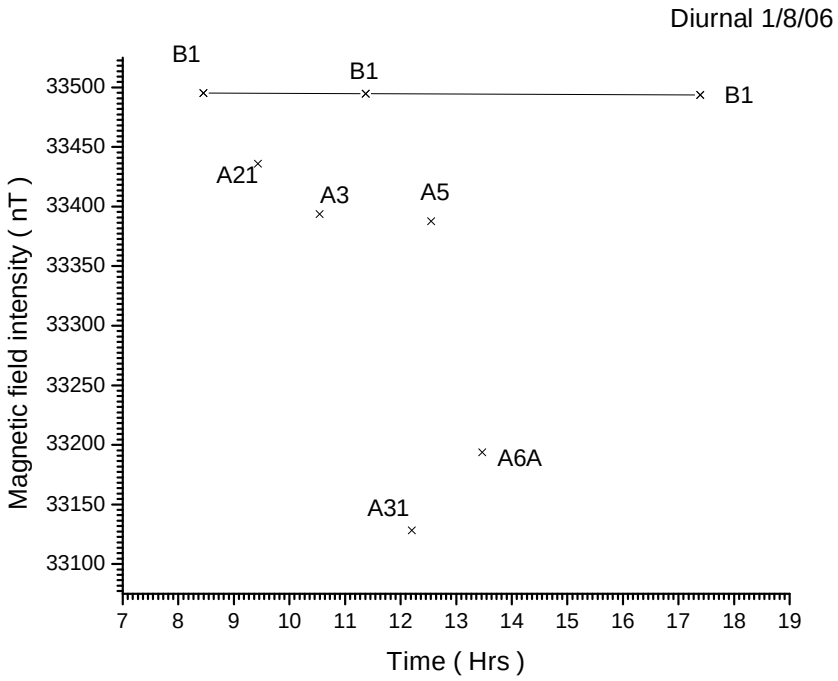

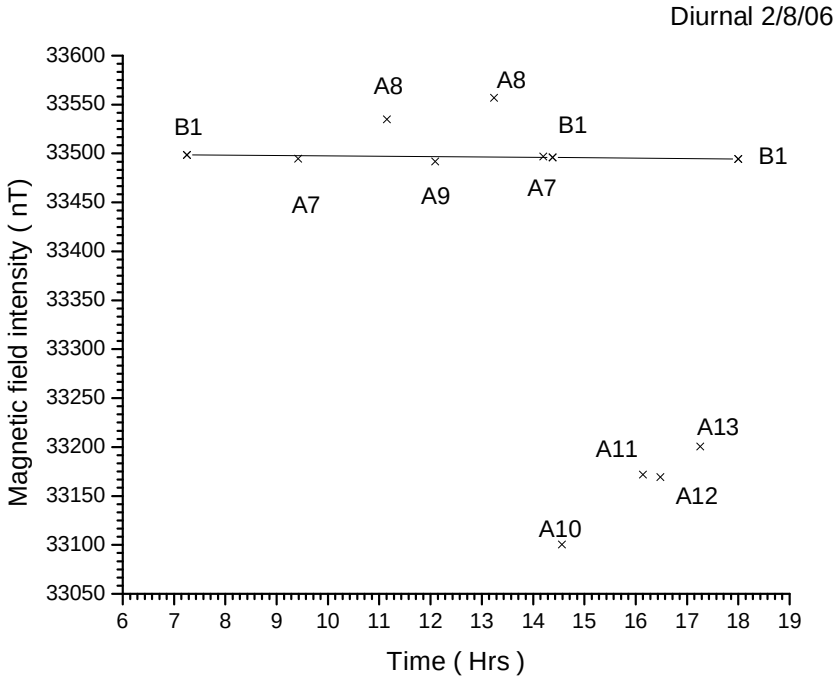

Diurnal 3/8/06

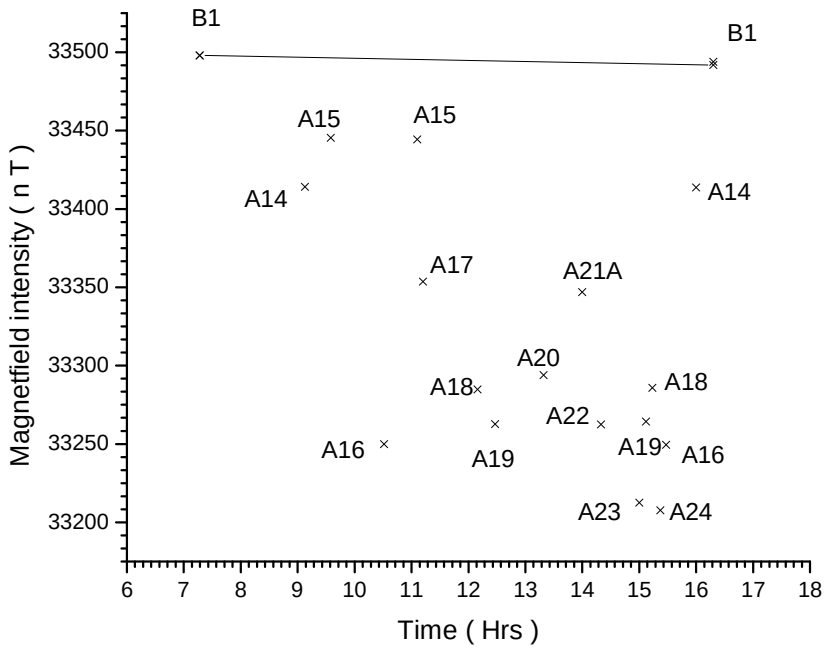

Diurnal 4/8/06

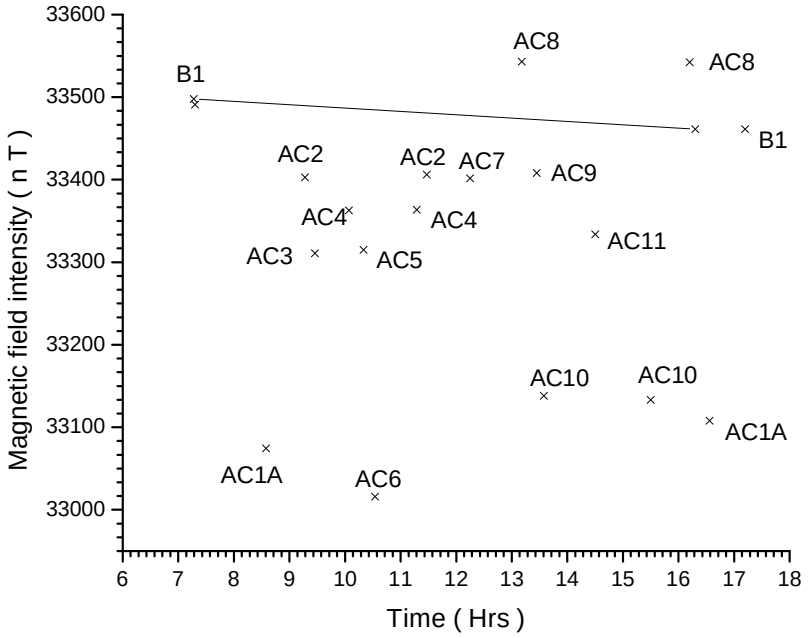

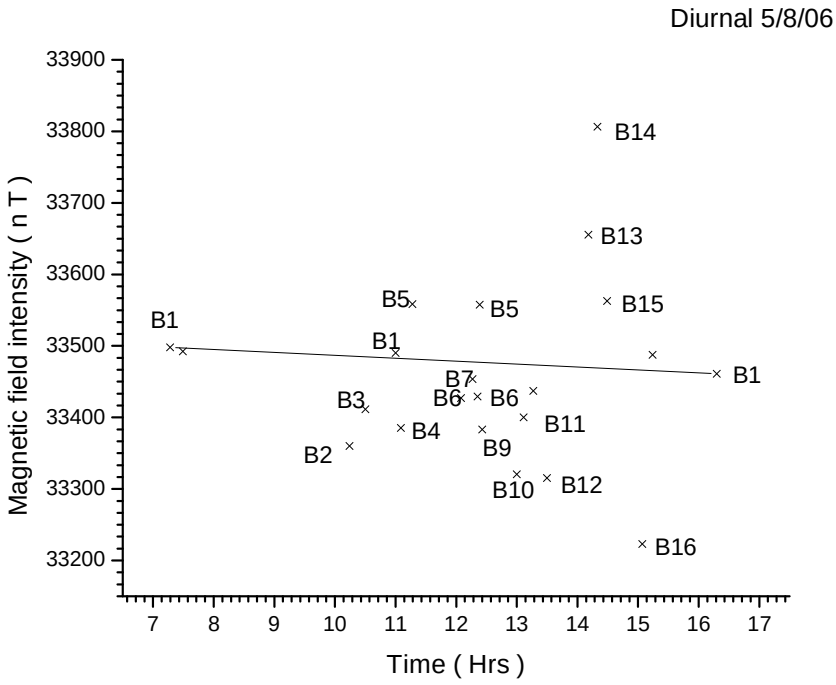
Diurnal 5/8/06
Magnetic field intensity (n T)
Time (Hrs)
33900
33800
33700
33600
33500
33400
33300
33200
7
8
9
10
11
12
13
14
15
16
17
B1
B1
B1
B2
B3
B4
B5
B5
B6
B6
B7
B9
B10
B11
B12
B13
B14
B15
B16

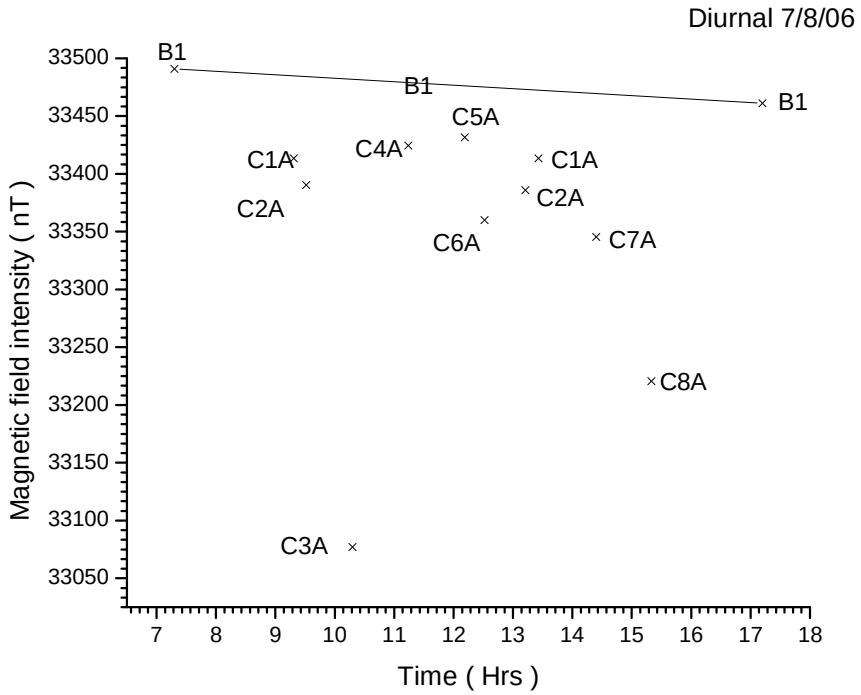
Diurnal 7/8/06
Magnetic field intensity (nT)
Time (Hrs)
33500
33450
33400
33350
33300
33250
33200
33150
33100
33050
7
8
9
10
11
12
13
14
15
16
17
18
B1
B1
B1
C5A
C4A
C1A
C1A
C2A
C2A
C6A
C7A
C8A
C3A

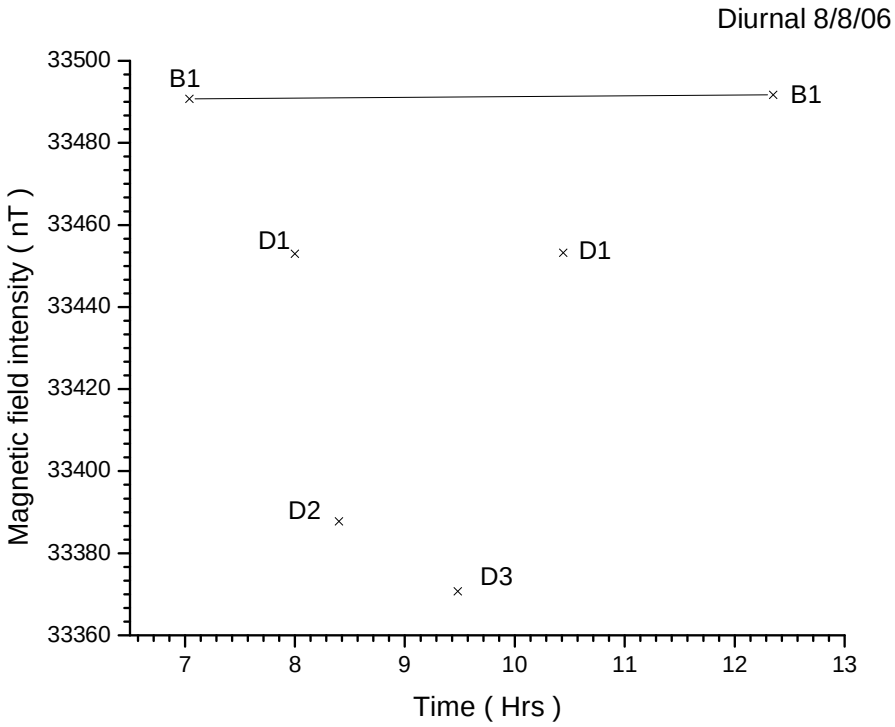
Diurnal 8/8/06
Magnetic field intensity (nT)
Time (Hrs)
33500
33480
33460
33440
33420
33400
33380
33360
7
8
9
10
11
12
13
B1
B1
D1
D1
D2
D3

Appendix D Terrain Corrections Listings

Station	Location	Height (m)	Average Elevation per compartment (metres)					
			e	f	g	h	i	J
			620	600	600	620	640	660
			620	600	600	620	680	670
			620	600	600	660	720	720
	197.8 E		600	620	600	660	710	730
		626	620	620	600	630	720	730
B1	9788.9 N		610	615	630	620	620	760
			600	630	610	620	620	710
			610	630	600	600	610	600
					600	600	620	600
					620	600	620	620
					620	600	600	620
					600	610	630	620
								620
								600
								600
								640
Terrain correction per zone (µgal)			39.8	19.6	10.7	5.9	18.4	13.6
Total terrain correction (Mgal)			0.108					

Station	Location	Height (m)	Average Elevation per compartment (metres)					
			e	f	g	h	i	j
			630	660	680	680	680	660
			620	660	700	730	740	720
			650	660	710	750	745	740
	199.96 E		620	630	720	730	720	800
		600.5	620	620	700	730	730	820
A21	9790.08 N		600	600	660	670	660	775
			620	600	620	620	600	775
			640	600	670	620	600	660
					620	620	600	600
					600	620	600	600
					600	620	620	630
					610	620	600	610
								615
								600
								625
								630
Terrain correction per zone (µgal)			125.3	102.6	105.3	93.6	52	42.5
Total terrain correction (Mgal)			0.521					

Station	Location	Height (m)	Average Elevation per compartment (metres)					
			E	f	g	h	i	j
			880	880	920	860	1020	880
			880	880	860	860	900	856
			880	880	860	880	1300	1200
	207.7 E		900	880	860	940	1200	1760
		878.5	910	930	860	940	1300	1300
A3	9813.4 N		940	930	860	860	900	1300
			920	950	860	960	1200	1200
			920	980	860	1000	1300	900
					860	1000	1000	1200
					860	1000	900	1060
					860	1050	900	820
					860	920	1000	840
								900
								916
								912
								960
Terrain correction per zone (µgal)			168	177.3	185.2	98.5	499.3	326
Total terrain correction (Mgal)			1.454					

Station	Location	Height (m)	Average Elevation per compartment (metres)					
			E	f	g	h	i	j
			880	860	856	900	900	980
			860	900	900	920	920	1100
			860	900	940	960	920	850
	205.3 E		880	880	960	960	920	855
		868	870	880	900	980	1020	856
A 7	9807 N		880	900	940	912	950	858
			870	900	900	910	910	860
			880	880	900	900	900	1020
					940	840	800	992
					900	850	760	800
					860	920	860	690
					860	860	900	700
								660
								700
								820
								813
Terrain correction per zone (µgal)			14.2	39.9	54.6	45.5	37.7	54.6
Total terrain correction (Mgal)			0.247					

Station	Location	Height (m)	Average Elevation per compartment (metres)					
			E	f	g	h	i	j
A8	204.1 E 9806.99 N	936.5	930	900	900	860	810	813
			920	900	850	855	900	1080
			920	900	850	840	940	960
			920	880	860	940	978	900
			920	860	900	910	932	856
			920	850	860	880	880	1081
			900	880	860	880	900	1060
			900	900	800	820	720	1000
					800	820	700	814
					800	820	640	700
					820	820	640	760
					920	920	820	640
								660
								640
								640
								820
Terrain correction per zone (µgal)			80.2	215.6	193.9	90.8	200.4	119.4
Total terrain correction (Mgal)			0.9					

Station	Location	Height (m)	Average Elevation per compartment (metres)					
			E	f	g	h	i	j
A9	203.17 E 9807.0 N	840.5	840	852	900	920	800	813
			840	880	920	860	860	840
			840	880	920	860	840	900
			840	860	920	880	960	940
			840	800	900	860	930	980
			850	800	900	860	916	1080
			840	800	800	880	720	1000
			840	820	700	760	690	910
					700	780	840	750
					760	660	660	740
					820	700	700	700
					820	820	800	615
								615
								615
								636
								760
Terrain correction per zone (µgal)			108	77.9	144.3	80.2	77.1	79.6
Total terrain correction (Mgal)			0.461					

Station	Location	Height (m)	Average Elevation per compartment (metres)					
			E	f	g	h	i	j
			840	800	813	800	800	834
			840	820	813	840	1100	940
			840	840	840	840	980	960
	204.31 E		840	840	860	900	920	840
		840.5	860	860	840	900	940	960
A 10	9803.469 N		860	900	840	860	880	960
			840	880	900	920	880	980
			840	820	900	820	700	900
					800	800	700	860
					800	800	640	780
					800	800	700	680
					800	800	760	630
								630
								635
								720
								750
Terrain correction per zone (µgal)			15.2	69	28.9	24.4	135.9	57.3
Total terrain correction (Mgal)			0.331					

Station	Location	Height (m)	Average Elevation per compartment (metres)					
			E	f	g	h	i	j
			840	840	840	850	900	900
			840	860	880	1169	960	833
			840	860	900	1100	840	832
	206.05 E		860	880	880	960	900	838
		845	860	860	890	920	940	850
A11	9802.67 N		840	840	900	920	950	855
			840	810	900	880	850	900
			840	810	840	840	920	990
					810	840	820	900
					810	813	800	852
					810	800	760	680
					810	800	820	680
								636
								700
								780
								800
Terrain correction per zone (µgal)			12	38.2	34.4	215.6	35.4	34.5
Total terrain correction (Mgal)			0.37					

Station	Location	Height (m)	Average Elevation per compartment (metres)					
			E	f	g	h	i	j
			820	820	820	820	850	890
			820	830	830	900	900	855
			820	840	860	980	920	860
	205.722 E		820	840	900	1170	880	830
		828	820	840	840	860	860	840
A12	9801.05 N		820	810	840	860	960	850
			820	810	810	840	900	900
			820	820	820	813	830	950
					800	780	800	860
					780	776	780	820
					800	780	756	700
					820	820	800	640
								620
								700
								770
								800
Terrain correction per zone (µgal)			10.2	8.1	20.2	166	31.6	31.6
Total terrain correction (Mgal)			0.268					

Station	Location	Height (m)	Average Elevation per compartment (metres)					
			E	f	g	h	i	j
			770	770	770	780	790	800
			770	760	770	800	820	830
			760	770	800	780	880	900
	203.349 E		770	760	800	820	1100	950
		787.5	760	780	800	813	860	930
A13	9800.90 N		800	770	790	830	840	940
			800	780	820	820	800	930
			780	770	780	820	660	880
					770	780	636	800
					770	800	630	700
					770	780	680	630
					770	760	780	600
								600
								610
								640
								760
Terrain correction per zone (µgal)			55.6	24.8	6.4	7.5	121.3	59.8
Total terrain correction (Mgal)			0.275					

Station	Location	Height (m)	Average Elevation per compartment (metres)					
			E	f	g	h	i	j
			780	780	760	756	760	800
			770	780	760	796	830	830
			780	775	760	800	820	900
	202.668 E		780	770	776	800	840	950
		778	780	780	780	800	840	1169
A14	9800.2 N		770	780	780	810	900	900
			780	780	780	800	750	850
			780	770	700	800	650	880
				770	700	620	650	700
					700	610	630	650
					760	700	620	610
					790	780	790	600
								600
								600
								600
								760
Terrain correction per zone (µgal)			3	1.4	36.6	68.9	68.7	90.3
Total terrain correction (Mgal)			0.269					

Station	Location	Height (m)	Average Elevation per compartment (metres)					
			E	f	g	h	i	j
			740	680	620	780	790	770
			725	760	740	750	795	818
			720	760	760	760	800	800
	201.673 E		740	760	780	770	800	940
		724	680	620	780	800	840	1170
A15	9800.239 N		620	610	700	800	820	845
			660	620	660	640	700	840
			700	680	600	620	630	880
					618	635	600	680
					618	630	600	620
					630	610	605	610
					680	700	660	625
								620
								600
								600
								650
Terrain correction per zone (µgal)			325.8	360.1	133.2	72.9	65	87.7
Total terrain correction (Mgal)			1.045					

Station	Location	Height (m)	Average Elevation per compartment (metres)					
			E	f	g	h	i	j
			610	610	720	720	760	760
			610	680	720	760	756	818
			610	660	740	780	776	834
	200.99 E		610	620	720	780	800	860
		599	610	615	700	800	830	1100
A16	9800.668 N		610	618	680	680	800	865
			618	618	620	630	700	920
			610	620	620	636	620	740
					630	620	615	640
					630	620	600	610
					620	630	600	650
					610	620	610	620
								625
								610
								600
								640
Terrain correction per zone (µgal)			24.1	105.5	155	170.8	144.4	143.2
Total terrain correction (Mgal)			0.743					

Station	Location	Height (m)	Average Elevation per compartment (metres)					
			E	f	g	h	i	j
			640	660	720	720	790	770
			660	700	740	780	760	790
			650	700	780	780	780	815
	201.317 E		625	680	800	840	813	1000
		625.5	630	620	800	810	900	980
A17	9801.601 N		630	620	660	680	780	900
			640	617	640	660	700	900
			640	618	630	645	610	820
					636	636	610	700
					617	660	600	640
					618	630	620	620
					618	610	610	650
								615
								615
								600
								640
Terrain correction per zone (µgal)			48.7	133	199.2	154.7	133.7	120.5
Total terrain correction (Mgal)			0.79					

Station	Location	Height (m)	Average Elevation per compartment (metres)					
			E	f	g	h	i	j
			640	636	630	700	700	780
			640	680	800	760	776	780
			640	660	810	820	810	830
	201.224 E		640	640	760	830	840	1100
		644	640	640	750	820	880	900
A18	9802.936 N		640	630	660	710	820	855
			636	636	640	700	630	880
			636	636	620	660	620	780
					620	620	620	680
					630	620	615	620
					630	640	620	605
					620	618	620	650
								643
								615
								600
								606
Terrain correction per zone (µgal)			3.5	17.1	145.7	133.1	112.3	104
Total terrain correction (Mgal)			0.516					

Station	Location	Height (m)	Average Elevation per compartment (metres)					
			E	f	g	h	i	j
			640	640	700	700	750	760
			640	700	800	820	760	800
			640	720	780	830	820	820
	201.43 E		650	700	820	900	840	1100
		650.5	645	660	780	820	880	920
A19	9803.747 N		650	640	700	760	780	860
			640	640	660	640	640	880
			640	645	700	630	660	860
					660	630	630	700
					620	630	630	615
					630	630	635	605
					640	620	620	700
								660
								620
								610
								630
Terrain correction per zone (µgal)			11.6	87.9	172.3	182.9	100.6	108
Total terrain correction (Mgal)			0.663					

Station	Location	Height (m)	Average Elevation per compartment (metres)					
			E	f	g	h	i	j
			680	660	640	640	700	720
			660	680	650	750	850	770
			660	680	700	850	900	820
	200.825 E		600	660	720	820	860	900
		661	660	640	700	750	900	880
A20	9805.273 N		640	640	660	640	750	900
			660	640	640	680	640	916
			680	700	620	660	615	720
					630	610	615	720
					610	610	610	660
					630	610	600	640
					700	640	630	780
								740
								670
								630
								620
Terrain correction per zone (µgal)			93.9	31	28.4	93.7	134.1	66
Total terrain correction (Mgal)			0.447					

Station	Location	Height (m)	Average Elevation per compartment (metres)					
			E	f	g	h	i	j
			680	660	670	640	700	720
			660	680	660	750	850	770
			660	680	700	850	900	800
	200.341 E		600	660	720	820	860	900
		614	660	640	700	750	900	880
A21A	9805.114 N		640	640	660	640	750	900
			660	640	640	680	640	916
			680	700	620	660	625	720
					630	610	615	720
					620	610	610	660
					630	640	600	640
					700		630	780
								740
								670
								630
								620
Terrain correction per zone (µgal)			345.9	192.6	78	150.2	194.8	106.3
Total terrain correction (Mgal)			1.068					

Station	Location	Height (m)	Average Elevation per compartment (metres)					
			E	f	g	h	i	j
			620	620	640	630	615	680
			620	700	640	640	800	780
			620	700	650	750	850	800
	199.87 E		640	640	650	710	900	860
		638	630	610	660	660	820	850
A22	9804.544 N		610	610	640	640	680	880
			610	610	620	660	700	900
			610	620	610	610	610	680
					610	610	600	680
					610	610	600	620
					610	615	605	700
					610	630	665	740
								700
								630
								615
								620
Terrain correction per zone (µgal)			67.2	92.4	9.4	23.6	117.3	64.7
Total terrain correction (Mgal)			0.375					

Station	Location	Height (m)	Average Elevation per compartment (metres)					
			E	f	g	h	i	j
			610	610	630	610	610	700
			635	620	635	680	780	750
			640	640	650	730	820	800
	200.025 E		620	620	650	750	900	840
		605.5	610	630	640	680	820	850
A23	9803.862		610	610	620	640	640	880
			610	610	630	660	650	820
			610	620	630	630	610	700
					630	630	600	700
					630	630	610	620
					630	630	600	780
					630	640	620	740
								673
								630
								600
								620
Terrain correction per zone (µgal)			46.8	21.6	19.4	60.1	135.1	83.1
Total terrain correction (Mgal)			0.366					

Station	Location	Height (m)	Average Elevation per compartment (metres)					
			E	f	g	h	i	j
A24	200.454 E 9802.559	620	625	630	620	620	700	700
			620	630	625	700	780	750
			620	640	680	810	810	800
			620	630	660	820	840	840
			625	630	650	760	900	880
			620	650	640	680	660	855
			620	635	650	640	660	850
			620	635	605	605	610	700
					605	605	610	630
					625	605	605	615
					636	635	600	720
					617	620	620	670
								620
								620
								600
								610
Terrain correction per zone (µgal)			1	18.7	15.2	115.9	128.9	66.2
Total terrain correction (Mgal)			0.346					

Station	Location	Height (m)	Average Elevation per compartment (metres)					
			E	f	g	h	i	j
AC1A	195.736 E 9792.199 N	601.5	600	600	600	600	600	600
			600	600	600	600	615	615
			600	600	600	600	605	670
			600	600	600	600	600	720
			600	620	600	600	600	700
			600	625	600	605	600	640
			600	625	640	640	615	620
			600	620	640	620	620	600
					620	620	605	615
					610	630	618	620
					620	620	600	720
					620	630	615	700
								736
								720
								640
								600
Terrain correction per zone (µgal)			0.4	15.6	7.6	4.5	0.8	19.5
Total terrain correction (Mgal)			0.048					

Station	Location	Height (m)	Average Elevation per compartment (metres)					
			E	f	g	h	i	j
AC2	194.196 E 9794.151 N	608	620	620	620	630	625	630
			615	630	640	600	600	600
			620	630	645	600	600	615
			625	620	640	600	600	620
			620	625	620	615	600	600
			625	630	625	620	615	600
			620	634	620	620	620	600
			615	625	628	620	615	620
					630	600	680	680
					605	600	720	680
					610	605	690	700
					620	600	600	700
								690
								700
								720
								605
Terrain correction per zone (µgal)			25	26.1	9.6	1.5	16.1	12.4
Total terrain correction (Mgal)			0.091					

Station	Location	Height (m)	Average Elevation per compartment (metres)					
			E	f	g	h	i	j
AC3	194.426 E 9797.065 N	618	620	620	620	640	635	615
			615	620	615	605	600	600
			620	620	615	600	600	600
			620	630	620	600	600	640
			620	620	615	615	600	605
			615	620	615	620	620	615
			620	620	620	620	680	600
			620	620	620	620	660	620
					620	620	680	714
					620	625	660	660
					625	625	610	660
					620	634	605	700
								705
								720
								665
								600
Terrain correction per zone (µgal)			0.8	1.5	0.2	1.8	8.3	9.2
Total terrain correction (Mgal)			0.022					

Station	Location	Height (m)	Average Elevation per compartment (metres)					
			E	f	g	h	i	j
AC4	194.487 E 9800.042 N	635	630	635	620	620	615	620
			630	620	631	615	600	600
			625	625	640	600	600	605
			625	630	640	615	600	630
			630	635	635	630	605	630
			635	650	640	635	670	610
			640	655	700	700	710	605
			640	660	700	714	700	670
					700	660	660	740
					680	640	660	700
					660	640	640	670
					660	650	640	650
								680
								680
								610
								620
Terrain correction per zone (µgal)			6.5	13.9	30.2	14.9	11.1	5.9
Total terrain correction (Mgal)			0.082					

Station	Location	Height (m)	Average Elevation per compartment (metres)					
			E	f	g	h	i	j
AC5	195.466 E 9803.115 N	670	640	640	640	620	615	605
			650	620	605	610	600	610
			660	620	600	600	615	620
			700	660	600	605	625	630
			700	670	600	600	610	700
			670	700	640	605	600	640
			670	660	660	720	750	615
			670	660	720	740	750	650
					700	750	710	816
					720	714	715	800
					690	700	714	690
					640	640	635	660
								670
								660
								670
								620
Terrain correction per zone (µgal)			63.2	61.5	52.1	45.6	26.2	12.9
Total terrain correction (Mgal)			0.262					

Station	Location	Height (m)	Average Elevation per compartment (metres)					
			E	f	g	h	i	j
AC6	195.759 E 9804.153 N	647	670	670	640	610	615	610
			665	620	600	620	600	610
			660	600	600	610	605	617
			640	640	600	605	650	650
			640	680	600	600	620	650
			670	700	650	650	600	650
			665	720	720	720	780	655
			670	680	740	740	750	670
					730	750	720	820
					730	715	715	800
					720	710	714	660
					673	640	640	665
								670
								660
								670
								630
Terrain correction per zone (µgal)			49.7	119.5	79.2	44.3	32.3	13.2
Total terrain correction (Mgal)			0.338					

Station	Location	Height (m)	Average Elevation per compartment (metres)					
			E	f	g	h	i	j
AC7	192.027 E 9797.165 N	618.5	615	615	625	615	630	618
			620	625	620	620	630	640
			625	630	620	620	615	615
			620	620	620	630	630	600
			615	620	630	660	640	600
			625	625	650	670	700	610
			620	625	650	660	660	660
			615	630	680	660	700	715
					660	720	700	680
					660	700	700	670
					680	690	730	776
					680	610	660	715
								715
								695
								693
								660
Terrain correction per zone (µgal)			2.6	3.6	31.5	28.8	27.6	16.7
Total terrain correction (Mgal)			0.111					

Station	Location	Height (m)	Average Elevation per compartment (metres)					
			E	f	g	h	i	j
AC8	190.73 E 9800.302 N	650	650	655	660	660	620	605
			660	665	665	655	640	620
			665	660	670	680	640	615
			650	650	700	690	650	620
			650	660	680	680	715	640
			660	660	680	690	700	680
			665	675	660	670	670	740
			660	660	670	670	680	700
					670	690	720	650
					670	700	750	654
					675	680	710	695
					660	660	680	720
								700
								700
								690
								730
Terrain correction per zone (µgal)			15	11.1	13.1	12	18.2	8.1
Total terrain correction (Mgal)			0.077					

Station	Location	Height (m)	Average Elevation per compartment (metres)					
			E	f	g	h	i	j
AC9	191.146 E 9803.04 N	666.5	690	690	670	680	670	620
			685	695	700	700	700	640
			690	700	700	710	700	625
			670	690	715	720	710	615
			690	670	710	720	740	605
			680	670	700	720	700	625
			675	675	670	680	680	780
			670	670	671	670	654	800
					670	670	620	660
					660	670	700	660
					660	670	700	680
					660	650	660	690
								720
								740
								700
								690
Terrain correction per zone (µgal)			45.2	27.4	14.5	13.4	9.9	12
Total terrain correction (Mgal)			0.122					

Station	Location	Height (m)	Average Elevation per compartment (metres)					
			E	f	g	h	i	j
B2	189.533 E 9798.978 N	663	680	680	670	680	700	720
			680	670	665	660	620	620
			680	675	660	655	640	620
			660	665	650	660	680	625
			670	660	650	650	680	620
			650	660	655	670	670	705
			670	660	660	700	670	715
			680	660	700	770	740	660
					680	750	720	650
					660	720	700	675
					700	740	710	750
					700	720	690	700
								670
								680
								700
								695
Terrain correction per zone (µgal)			28.5	4.5	9.1	36.4	11.4	5.9
Total terrain correction (Mgal)			0.096					

Station	Location	Height (m)	Average Elevation per compartment (metres)					
			E	f	g	h	i	j
B3	188.62 E 9796.354 N	697.5	680	680	710	710	700	730
			680	690	715	749	660	680
			680	690	710	650	610	630
			680	680	700	660	620	620
			710	720	700	690	630	630
			710	720	710	700	660	680
			680	715	720	720	750	660
			695	700	720	750	720	670
					720	720	680	700
					720	720	690	690
					700	720	700	680
					695	690	680	700
								680
								670
								660
								675
Terrain correction per zone (µgal)			36.8	17.8	5.3	12.4	15.9	5
Total terrain correction (Mgal)			0.093					

Station	Location	Height (m)	Average Elevation per compartment (metres)					
			E	f	g	h	i	j
B4	187.062 E 9794.121 N	706	700	680	680	680	680	670
			700	685	685	693	710	720
			700	690	690	700	680	670
			700	720	700	710	690	630
			705	715	695	700	690	610
			700	715	720	720	740	620
			700	700	715	715	720	670
			700	690	700	680	660	700
					700	660	660	700
					690	660	680	680
					690	680	650	670
					680	685	660	660
								650
								650
								635
								650
Terrain correction per zone (µgal)			5.1	17.6	5.7	7.9	8.5	10
Total terrain correction (Mgal)			0.055					

Station	Location	Height (m)	Average Elevation per compartment (metres)					
			E	f	g	h	i	j
B5	184.355 E 9794.431 N	646.5	650	650	650	655	660	645
			650	650	655	690	675	660
			655	660	660	700	685	700
			655	655	670	715	715	710
			650	655	670	700	730	730
			650	650	670	670	690	720
			650	650	655	655	680	760
			650	650	655	665	672	700
					655	660	660	720
					650	655	655	690
					650	650	650	675
					650	650	645	650
								655
								650
								650
								635
Terrain correction per zone (µgal)			4.4	3.4	4.1	14.8	11.5	9.6
Total terrain correction (Mgal)			0.048					

Station	Location	Height (m)	Average Elevation per compartment (metres)					
			E	f	g	h	i	j
B6	183.976 E 9791.038 N	635	635	640	635	635	640	635
			640	645	635	640	650	650
			640	645	640	645	660	690
			642	645	655	670	675	700
			640	640	650	660	690	710
			636	640	650	650	660	700
			640	645	650	650	655	720
			640	640	650	655	655	680
					645	645	655	660
					645	645	645	665
					640	640	640	655
					635	635	636	656
								650
								640
								640
								635
Terrain correction per zone (µgal)			3.5	4.4	2.9	3.3	4.8	6.5
Total terrain correction (Mgal)			0.025					

Station	Location	Height (m)	Average Elevation per compartment (metres)					
			E	f	g	h	i	j
B7	185.819 E 9787.871 N	647.5	645	645	635	650	650	650
			647	650	645	652	670	684
			645	647	645	660	685	695
			640	645	645	660	700	700
			640	640	650	660	670	710
			640	639	652	655	670	736
			645	635	640	660	650	693
			645	639	638	639	645	680
					636	636	640	650
					635	635	638	650
					638	635	634	650
					640	640	635	645
								639
								633
								632
								634
Terrain correction per zone (µgal)			4.1	3.4	1.5	1.4	3.9	4.8
Total terrain correction (Mgal)			0.019					

Station	Location	Height (m)	Average Elevation per compartment (metres)					
			E	f	g	h	i	j
			650	650	652	659	655	650
			650	652	660	670	665	655
			650	655	662	672	690	645
	186.413 E		650	650	660	672	700	650
		646	650	650	658	660	680	655
B8	9784.998 N		650	645	650	655	660	660
			650	642	650	650	645	720
			650	645	645	640	637	660
					640	635	635	655
					639	632	635	640
					640	635	634	640
					649	645	640	639
								635
								636
								635
								637
Terrain correction per zone (µgal)			2.6	1.6	1.8	3.1	4.6	1.5
Total terrain correction (Mgal)			0.015					

Station	Location	Height (m)	Average Elevation per compartment (metres)					
			E	f	g	h	i	j
			675	660	660	650	640	640
			670	670	660	640	640	640
			665	680	660	640	635	600
	188.751 E		670	670	680	645	620	600
		669	670	665	690	680	660	600
B9	9782.256 N		675	660	680	694	695	620
			680	662	675	674	672	680
			680	665	665	660	650	710
					660	650	640	660
					660	650	640	640
					660	660	640	632
					660	660	650	636
								640
								640
								650
								645
Terrain correction per zone (µgal)			6.6	3.2	2.4	4.7	5.9	5.8
Total terrain correction (Mgal)			0.029					

Station	Location	Height (m)	Average Elevation per compartment (metres)					
			E	f	g	h	i	j
B10	188.866 E 9779.21 N	640	660	640	660	660	640	660
			640	670	660	640	640	640
			660	680	660	640	640	600
			660	670	680	650	620	600
			670	660	700	680	660	600
			670	660	680	700	700	640
			680	670	680	680	670	700
			680	665	660	660	650	720
					660	660	640	660
					660	650	640	640
					660	660	640	640
					660	660	660	640
								640
								640
								650
								650
Terrain correction per zone (µgal)			7.7	3.7	2.9	4.5	6.4	6
Total terrain correction (Mgal)			0.031					

Station	Location	Height (m)	Average Elevation per compartment (metres)					
			E	f	g	h	i	j
B11	190.026 E 9776.383 N	645	650	660	660	660	640	660
			650	670	660	640	640	640
			665	680	660	640	635	600
			640	670	680	660	620	600
			650	665	700	680	660	600
			660	660	680	700	695	620
			660	662	680	680	672	680
			650	660	670	660	650	720
					660	660	640	660
					660	660	640	640
					660	660	640	632
					660	660	650	636
								640
								640
								650
								660
Terrain correction per zone (µgal)			6.6	4.6	5.4	6.7	6.9	7.8
Total terrain correction (Mgal)			0.038					

Station	Location	Height (m)	Average Elevation per compartment (metres)					
			E	f	g	h	i	j
B12	192.238 E 9776.77 N	606	600	640	660	660	660	680
			605	640	660	640	640	640
			620	620	660	640	640	620
			600	600	680	660	620	600
			600	620	690	680	660	600
			600	640	680	694	695	620
			620	662	680	680	680	680
			610	665	680	660	660	720
					660	650	640	660
					660	650	640	640
					660	660	640	640
					660	660	650	640
								640
								640
								680
								660
Terrain correction per zone (µgal)			11.6	8.6	7.4	9.7	10.9	10.8
Total terrain correction (Mgal)			0.059					

Station	Location	Height (m)	Average Elevation per compartment (metres)					
			E	f	g	h	i	j
B13	194.02 E 9778.976 N	599	675	660	660	650	640	640
			670	670	660	640	640	640
			665	680	660	640	635	600
			670	670	680	645	620	600
			670	665	690	680	660	600
			675	660	680	694	695	620
			680	662	675	674	672	680
			680	665	665	660	650	710
					660	650	640	660
					660	650	640	640
					660	660	640	632
					660	660	650	636
								640
								640
								650
								645
Terrain correction per zone (µgal)			17.3	14.5	8.3	9.8	6.2	6.9
Total terrain correction (Mgal)			0.063					

Station	Location	Height (m)	Average Elevation per compartment (metres)					
			E	f	g	h	i	j
			620	640	630	630	635	620
			625	630	635	700	680	680
			625	640	710	600	700	700
	196.338 E		620	640	710	605	660	710
		618.3	620	610	680	610	610	715
B14	9780.519 N		622	615	640	650	630	700
			610	600	635	630	600	610
			620	620	615	600	610	620
					610	600	610	600
					620	600	605	620
					620	615	615	660
					640	620	620	650
								640
								640
								630
								620
Terrain correction per zone (µgal)			3.7	17.1	41.5	10.4	8.5	8.7
Total terrain correction (Mgal)			0.09					

Station	Location	Height (m)	Average Elevation per compartment (metres)					
			E	f	g	h	i	j
			663	640	630	660	670	680
			660	620	620	620	680	680
			660	630	620	635	700	714
	197.563 E		662	630	620	620	700	720
		660	660	660	620	620	655	720
B15	9783.338 N		660	650	635	620	630	730
			660	660	655	620	615	730
			662	665	625	600	600	620
					620	600	600	600
					650	620	600	600
					640	640	615	625
					660	670	635	650
								620
								600
								620
								640
Terrain correction per zone (µgal)			0.3	34.1	21	19.5	12.8	8.4
Total terrain correction (Mgal)			0.096					

Station	Location	Height (m)	Average Elevation per compartment (metres)					
			E	f	g	h	i	j
B16	197.666 E 9786.628 N	642	630	610	610	615	620	660
			640	605	610	640	660	700
			630	605	610	650	700	714
			640	615	610	645	730	720
			642	640	610	625	670	740
			642	630	620	620	620	750
			640	630	630	605	600	740
			640	640	610	600	615	600
					610	600	600	600
					610	600	600	600
					620	600	600	600
					630	640	645	650
								640
								640
								600
								640
Terrain correction per zone (µgal)			6.1	41.6	17.6	10.9	13.4	12.1
Total terrain correction (Mgal)			0.102					

Station	Location	Height (m)	Average Elevation per compartment (metres)					
			E	f	g	h	i	j
C1A	201.727 E 9794.369 N	742.5	750	760	760	750	740	750
			760	755	780	760	750	740
			755	770	790	780	760	800
			760	760	770	760	810	840
			750	740	755	765	780	875
			740	720	760	775	770	850
			740	690	740	700	700	810
			750	720	690	620	605	770
					660	600	600	620
					660	605	600	615
					680	630	610	600
					730	700	720	607
								620
								600
								610
								680
Terrain correction per zone (µgal)			18.9	46	47	80.6	55.1	38.5
Total terrain correction (Mgal)			0.287					

Station	Location	Height (m)	Average Elevation per compartment (metres)					
			E	f	g	h	i	j
			700	705	715	730	754	722
			705	739	735	740	730	750
			710	735	740	739	740	760
	201.011 E		701	730	755	740	780	830
		705.5	700	700	740	770	775	810
C2A	9791.376 N		702	660	740	730	760	790
			705	660	680	650	670	795
			705	700	630	615	600	770
					625	610	600	645
					625	610	615	600
					620	610	615	605
					615	610	645	622
								615
								600
								620
								630
Terrain correction per zone (µgal)			2.3	58.9	77.6	61.6	38.9	25.5
Total terrain correction (Mgal)			0.265					

Station	Location	Height (m)	Average Elevation per compartment (metres)					
			E	f	g	h	i	j
			705	720	720	710	714	730
			720	720	720	715	720	770
			730	740	718	720	750	800
	201.085 E		700	720	718	735	750	820
		696	690	700	740	750	730	825
C3A	9786.815 N		690	680	720	740	740	810
			700	680	700	700	650	760
			700	680	680	620	620	750
					660	615	630	650
					660	610	620	615
					670	630	615	600
					690	670	655	605
								600
								625
								660
								670
Terrain correction per zone (µgal)			38.2	38.6	15.3	35.2	23	24.8
Total terrain correction (Mgal)			0.175					

Station	Location	Height (m)	Average Elevation per compartment (metres)					
			E	f	g	h	i	j
C4A	203.022 E 9786.545N	716.5	720	725	722	720	740	800
			720	720	720	730	780	820
			715	725	720	735	820	830
			720	730	730	730	820	835
			720	730	735	730	770	835
			720	730	735	740	755	855
			720	725	740	750	750	815
			720	720	738	740	700	750
					720	700	660	755
					720	700	630	650
					725	720	670	610
					720	715	714	615
								630
								630
								660
								720
Terrain correction per zone (µgal)			1.8	6.9	3.8	4	28.4	29.7
Total terrain correction (Mgal)			0.075					

Station	Location	Height (m)	Average Elevation per compartment (metres)					
			E	f	g	h	i	j
C5A	203.306 E 9788.854 N	733	740	740	750	730	730	740
			742	740	752	750	780	840
			740	742	750	780	835	860
			740	745	745	720	840	880
			740	740	740	740	800	900
			739	748	740	740	780	860
			739	744	739	739	740	870
			742	735	740	760	720	800
					767	754	680	770
					750	680	675	690
					749	754	680	640
					750	740	700	620
								630
								630
								655
								714
Terrain correction per zone (µgal)			8.6	6.3	6.1	7.9	26.2	37.3
Total terrain correction (Mgal)			0.092					

Station	Location	Height (m)	Average Elevation per compartment (metres)					
			E	f	g	h	i	j
C6A	203.348 E 9790.577 N	733	740	742	745	740	745	740
			750	760	740	745	800	830
			750	760	740	780	840	860
			740	740	740	750	825	855
			738	739	760	760	780	900
			739	739	745	755	797	880
			738	745	740	780	780	850
			740	739	760	740	700	818
					760	720	650	755
					762	730	660	640
					750	767	725	610
					750	744	750	610
								615
								610
								630
								720
Terrain correction per zone (µgal)			16.2	16	7.6	8.3	29.8	42.1
Total terrain correction (Mgal)			0.12					

Station	Location	Height (m)	Average Elevation per compartment (metres)					
			E	f	g	h	i	j
C7A	202.464 E 9797.027 N	767	770	785	780	780	795	760
			765	790	760	790	800	800
			765	760	755	800	810	870
			780	780	760	820	800	875
			782	790	760	790	820	910
			778	796	755	760	776	965
			780	790	770	780	740	840
			782	782	780	720	620	815
					720	700	615	740
					700	685	600	636
					760	720	640	610
					765	780	755	600
								600
								600
								630
								725
Terrain correction per zone (µgal)			18.5	27.8	14	23.4	62	52.5
Total terrain correction (Mgal)			0.198					

Station	Location	Height (m)	Average Elevation per compartment (metres)					
			E	f	g	h	i	j
C8A	204.091 E 9796.923 N	750	770	775	790	800	780	760
			780	810	810	800	830	860
			782	800	820	810	890	890
			770	790	830	810	900	870
			750	760	820	834	840	835
			750	755	795	796	810	870
			750	750	756	756	780	1169
			760	760	750	780	760	810
					780	796	670	810
					780	765	680	636
					780	780	760	625
					770	775	780	615
								600
								630
								700
								730
Terrain correction per zone (µgal)			55.8	74	49.7	28.5	47.4	74.4
Total terrain correction (Mgal)			0.33					

Station	Location	Height (m)	Average Elevation per compartment (metres)					
			E	f	g	h	i	j
D1	200.176 E 9792.43N	633	640	680	700	700	720	670
			660	700	760	760	780	740
			650	700	755	765	796	750
			660	675	760	780	760	800
			640	605	720	795	756	800
			645	600	690	700	720	830
			640	600	600	610	630	780
			620	625	600	600	600	720
					600	600	600	630
					600	600	600	600
					600	600	610	615
					640	605	610	610
								645
								610
								610
								620
Terrain correction per zone (µgal)			43.8	138	125.6	104	63	34
Total terrain correction (Mgal)			0.509					

Station	Location	Height (m)	Average Elevation per compartment (metres)					
			E	f	g	h	i	j
D2	200.589 E 9795.184 N	667.5	680	680	680	680	720	750
			690	700	720	760	796	740
			680	700	740	770	796	760
			660	670	745	755	800	800
			640	620	740	796	780	800
			620	610	680	720	720	830
			620	605	600	612	620	776
			660	670	600	600	600	700
					600	600	600	630
					600	600	600	600
					600	600	600	615
					660	605	600	615
								630
								605
								600
								650
Terrain correction per zone (µgal)			120.9	101.6	78.8	77.7	59.8	25.8
Total terrain correction (Mgal)			0.465					

Station	Location	Height (m)	Average Elevation per compartment (metres)					
			E	f	g	h	i	j
D3	200.805 E 9797.03 N	683	685	700	700	720	770	720
			700	720	740	760	796	780
			680	720	790	750	780	797
			640	700	795	770	796	820
			610	615	720	775	770	830
			620	615	700	700	720	810
			680	610	615	625	625	813
			660	640	605	630	600	750
					600	600	600	650
					600	600	600	636
					600	600	600	600
					640	620	620	630
								615
								625
								600
								620
Terrain correction per zone (µgal)			227.2	170.2	115.7	60	55	29.5
Total terrain correction (Mgal)			0.658					

Appendix E: Derivation of Structural Indices of Extended Bodies.

The structural indices may be derived by direct solution of Euler's equation E.1 shown below.

$$(X - X_0)\frac{\partial T}{\partial X} + (Y - Y_0)\frac{\partial T}{\partial Y} + (Z - Z_0)\frac{\partial T}{\partial Z} = -N(T - B) \quad \text{---------- (E.1)}$$

Magnetic Anomaly of Thin Dyke.

The vertical magnetic anomaly Z of an infinite thin dyke (Bosum, 1968) may be expressed as:

$$Z(x,z) = \frac{AS}{r^2} \quad \text{---------- (E.2)}$$

Where $A = 2Mt\cos\varphi$, t is the dyke thickness ($t<<z_o$), M is magnetisation intensity and (x_o, z_o) are the coordinates of the dyke top.

$Cos\varphi = \left[Cos^2\alpha Cos^2 I + Sin^2 I\right]^2$, Where α is the azimuth of profile with respect to magnetic north and I is the inclination of geomagnetic field.

$TanI' = \frac{TanI}{Cos\alpha}$, This is the reduced field inclination.

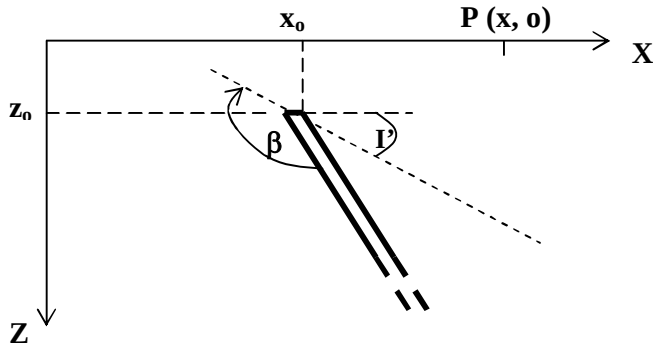

Figure A.1: Illustration of a dipping thin dyke.

$$S = \left[-(x - x_o)Sin\beta + (z - z_o)Cos\beta\right] \quad \text{---------- (E.3)}$$

Where β is the dip of the dyke with respect to the reduced inclination of field and

$r^2 = (x - x_o)^2 + (z - z_o)^2$

The partial derivatives of equation E.2 can be expressed as;

$\frac{\partial Z}{\partial x} = -A\frac{\left[r^2 Sin\beta + 2S(x - x_o)\right]}{r^4}$ And $\frac{\partial Z}{\partial z} = A\frac{\left[r^2 Cos\beta - 2S(z - z_o)\right]}{r^4}$ substituting

these derivatives to Euler's equation E.1 yields,

$$= A\left\{-(x - x_o)Sin\beta r^2 + (z - z_o)Cos\beta r^2 - 2S\left[(z - z_o)^2 + (x - x_o)^2\right]\right\}\frac{1}{r^4}$$

$$= A\frac{\left[Sr^2 - 2Sr^2\right]}{r^4} \quad \text{---------- (E.4)}$$

$$= -\frac{AS}{r^2} = -Z(x, z) \quad \text{---------- (E.5)}$$

If this result is compared to the right hand side of equation E.1, then N has to be equal to 1.0. Therefore the structural index of a dipping thin dyke is 1.0. Since the result is independent of dip of the dike or the earth's field, it is valid for total field anomalies and includes sill edges. Sills can be considered to be dikes with zero dip.

Gravity Anomaly of a Finite Step

The gravity anomaly of a finite step or fault may be expressed (Jung, 1961) as;

$$g(x, z) = 2G\rho\left[\phi_o(z - t) - \phi_u(z - T) + (x - x_o)\ln\left(\frac{R_U}{R_o}\right)\right] \quad \text{---------- (E.6)}$$

Where G is the gravitational constant, ρ is the density contrast, x_o is the x coordinates of the step midpoint and T (t) is the depth to the top of the step.

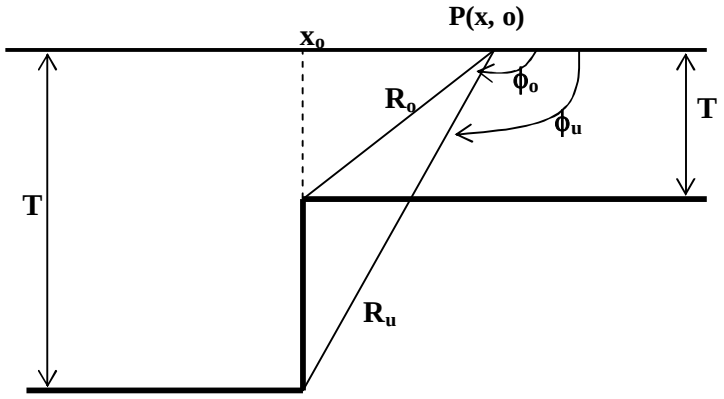

Figure A.2: Illustration of a finite step.

ϕ_o Or $\phi_u = \frac{\pi}{2} + \arctan\frac{(x - x_o)}{(t(orT) - z)}$ and $R_o(orR_U) = \{(x - x_o)^2 + [z - t(orT)]^2\}^{\frac{1}{2}}$ --- (E.7)

Substituting this into Euler's equation E.1 yields;

$$(x - x_o)\frac{\partial g}{\partial x} + (z - z_o)\frac{\partial g}{\partial z} = 2G\rho\left[(z - z_o)(\phi - \phi_u) + (x - x_o)\ln\left(\frac{R_u}{R_o}\right)\right] \text{ ---------- (E.8)}$$

This approximates the expression for g(x, z) as long as t ≅ T that is depth to the step is considerably greater than step thickness. Therefore the structural index is 1.0.

Magnetic Anomaly of a Sloping Contact

The magnetic anomaly of a magnetic contact often a fault is given by Am (1972) as;

$$F(x, z) = C(\Phi Sin\Theta - Cos\Theta \ln R) + K \quad \text{---------- (E.9)}$$

Where $C = 2P\frac{F'}{F}Sin\delta$ and $\phi = \frac{\pi}{2} + \arctan\left[\frac{(x - x_o)}{(z - z_o)}\right]$

$\Theta = I'(P) + I'(F) - \partial$, Where P is the polarisation vector and F the measurement vector.

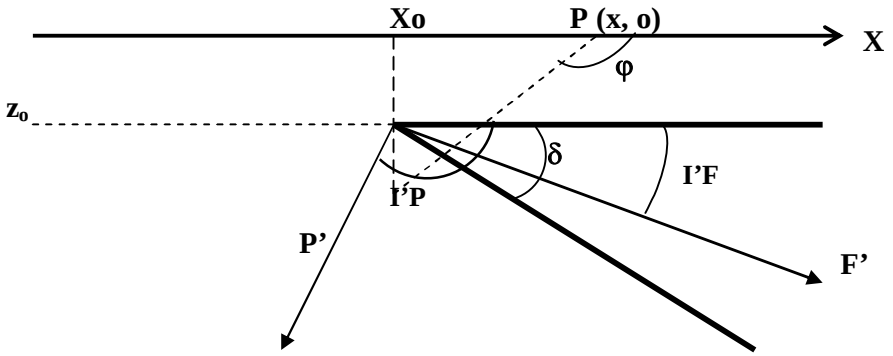

Figure A.3: Illustration of a slopping contact.

P', F' are projections of P, F in the x-z plane while I' (P) and I' (F) are inclinations of the projected vectors P' and F'.

$R = \left[(x - x_o)^2 - (z - z_o)^2\right]^{\frac{1}{2}}$, K is offset while δ is the dip of the contact.

The $\frac{\partial F}{\partial x} = C Cos\Theta \frac{(x - x_o)}{R^2} - C Sin\Theta \frac{(z - z_o)}{R^2}$ and $\frac{\partial F}{\partial z} = C Sin\Theta \frac{(x - x_o)}{R^2} + C Cos\Theta \frac{(z - z_o)}{R^2}$

Substituting this in Euler's equation E.1 yields,

$(x - x_o)\frac{\partial F}{\partial x} + (z - z_o)\frac{\partial F}{\partial z} = C Cos\Theta$ ---------- (E.10)

This implies that the structural index is zero.

Appendix F: Estimating depth to magnetic sources by spectral analysis (Blakely, R.J., 1995)

The magnetic potential of a dipole of dipole moment m give by equation F.1,

$$V = -C_m m \nabla_p \frac{1}{r} \qquad \text{---------- (F.1)}$$

Where C_m is a constant. The Fourier transform of this potential is given in equation F.2.

$$F[V] = -2\pi C_m m \Theta_m e^{|k|(z_0 - z')} \quad Z' > z_0 \qquad \text{---------- (F.2)}$$

Where $\Theta_m = \hat{m}_z + i\frac{(\hat{m}_x k_x + \hat{m}_y k_y)}{|k|}$ and Θ_m is a complex function of k_x and k_y that depends on the orientation of the dipole.

The magnetic field is related to the potential by the equation $B = -\Delta_p V$, and so any component of B is found from the directional component of B. The total field anomaly is hence given as in equation F.3.

$$\Delta T = -\hat{f}.\nabla_p V = -\hat{f}_x \frac{\partial}{\partial x} V - \hat{f}_y \frac{\partial}{\partial y} V - \hat{f}_z \frac{\partial}{\partial z} V \qquad \text{---------- (F.3)}$$

Where f is a unit vector parallel to the ambient field. Therefore observed from a horizontal plane, the Fourier transform of the total field anomaly is as in equation F.4.

$$F[\nabla T] = -\hat{f}_x F\left[\frac{\partial}{\partial x} V\right] - \hat{f}_y F\left[\frac{\partial}{\partial y} V\right] - \hat{f}_z F\left[\frac{\partial}{\partial z} V\right]$$

$$= -if_x k_x F[V] - if_y k_y F[V] - f_z \frac{\partial}{\partial z} F[V] \qquad \text{---------- (F.4)}$$

Equation F.2 and F.4 can be combined to yield equation F.5 as below.

$$F\left[\nabla T = 2\pi C_m m \Theta_m \Theta_f |k| e^{|k|(z_o - z')}\right], \; z' > z_o \qquad \text{---------- (F.5)}$$

Where $\Theta_f = \hat{f}_z + i\frac{(\hat{f}_x k_x + \hat{f}_y k_y)}{|k|}$

From equation F.5, orientations of vectors m and f are contained in Θ_m and Θ_f while depth of the dipole is within the exponential term. To find the Fourier transform of the anomaly over a vertical line of dipoles, equation F.6 is integrated along the z-axis.

Considering the top of the magnetic source to be at coordinate (0,0, z_1) and the bottom at (0,0, z_2) as illustrated in figure A.4.

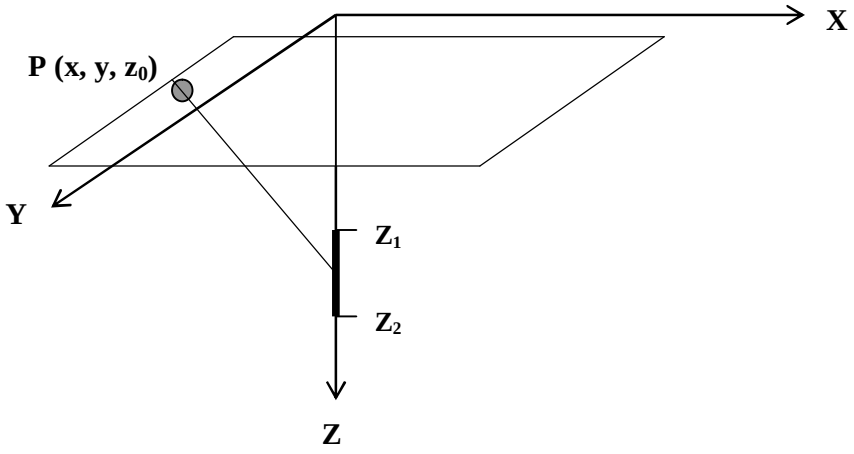

Figure A.4. A line source observed on horizontal surface.

Let each element of the vertical line has a dipole moment m equal to m'dz, where m' is moment per unit length. The Fourier transform of the anomaly can be expressed as in equation F.6.

$$F[\Delta T] = 2\pi C_m m' \Theta_m \Theta_f |k| \int_{z_1}^{z_2} e^{|k|(z_0 - z')} dz'$$

$$= 2\pi C_m m' \Theta_m \Theta_f e^{|k| z_0} (e^{-|k| z_1} - e^{-|k| z_2}),\ z_2 > z_1,\ z_1 > z_0 \quad \text{---------- (F.6)}$$

Mathematical statement of Fourier –convolution theorem can be expressed as equation F.7.

$$F[f] = F|s|.F|\varepsilon| \quad \text{---------- (F.7)}$$

That is the Fourier transform of the potential field is equal to the Fourier transform of the source distribution multiplied by the Fourier transform of Green's function. For the total field anomaly, Fourier transform of Green's function is obtained from equation 6 and when applied to equation F.7, yields equation F.8.

$$F[\Delta T] = F[M]\left\{2\pi C_m \Theta_m \Theta_f e^{|k| z_0} (e^{-|k| z_1} - e^{-|k| z_2})\right\},\ z_0 < z_1,\ z_1 < z_2 \quad \text{---------- (F.8)}$$

Where magnetization M is a function of x and y. The Fourier transform in equation F.8 has separated the total field anomaly into the magnetization and a function that depends on other attributes such as depth, thickness and direction of magnetization.

A statistical approach can be applied in estimating the average depth of a large collection of magnetic sources. Consider the total field anomaly measured on a horizontal surface and caused by a horizontal layer with top at a depth d and thickness t. This substituted in equation F.8 can be expressed as equation F.9.

$$F[\Delta T] = F[M]\left\{2\pi C_m \Theta_m \Theta_f e^{-|k|^d}(1-e^{-|k|^t})\right\} \quad \text{---------- (F.9)}$$

The total field anomaly is measured in discrete locations and hence $F[\Delta T]$ and Θ_f are easily determined. Assuming layer extends infinitely far in horizontal directions, and that M (x,y) is a random function of x and y, then $F|M|$ and $F[\Delta T]$ do not exist as the inequality in equation F.10 is not satisfied.

$$\int_{-\infty}^{\infty} |f(x)| dx < \infty \quad \text{---------- (F.10)}$$

Equation F.9 can hence be simplified to equation F.11.

$$\Theta_{\Delta T}(k_x, k_y) = \Theta_M(k_x, k_y).F(k_x, k_y) \quad \text{---------- (F.11)}$$

Where $\Theta_{\Delta T}$ and Θ_M are power density spectra of the total field anomaly and magnetization respectively. The Fourier transform in wave number domain can be expressed as in equation F.12.

$$F(k_x, k_y) = 4\pi^2 C_m{}^2 |\Theta_m|^2 |\Theta_f|^2 e^{-2|k|^d}(1-e^{-|k|^t})^2 \quad \text{---------- (F.12)}$$

The radial average of equation F.11 can hence be written as equation F.13.

$$\Theta_{\Delta T}(|k|) = A\Theta_M(|K|)e^{-2|k|^d}(1-e^{-|k|^t}) \quad \text{---------- (F.13)}$$

Where A is a constant that depends on the orientation of magnetization and the regional field. If M (x, y) is completely random and uncorrelated, $\Theta_m(k_x, k_y)$ is a constant and equation F.13 is expressed as equation F.14.

$$\Theta_{\Delta T}(|K|) = Be^{-2|k|^d}(1-e^{-|k|^t})^2 \quad \text{---------- (F.14)}$$

Where B is a constant. Taking logarithm of both sides of equation F.14, yield equation F.15.

$$Ln\Theta_{\Delta T}(|K|) = LnB - 2|k|d + 2Ln(1 - e^{-|k|t}) \quad \text{---------- (F.15)}$$

From equation F.15, the depth d can be estimated by calculating power density spectrum of ΔT and fitting a straight line through high wave number part of the spectrum. Half of the slope of the line is an estimate of depth d.